UCLouvain

epl

École polytechnique de Louvain

# Characterization of the behavior of advanced surface treatments to rain erosion: towards a material performance index

Author: **Matthieu Van de Wyngaert**
Supervisors: **Thomas Pardoen, Pierre Bollen**
Readers: **Evelyne Van Ruymbeke, Laurent Delannay**
Academic year 2020–2021
Master [120] in Chemical and Materials Engineering

# Abstract

Water droplet erosion (WDE), or the form of material wear caused by high speed impact of water droplets, is a serious damage mechanism affecting the lifetime of leading edges of airplanes and wind turbines. This erosion can be simulated in testing machines in two main ways, either by accelerating the sample as in whirling arm rain erosion rigs (WARER) or by projecting the water droplets as in pulsating jet erosion tests (PJET).

In the present work, a study of the erosion damage mechanisms using both techniques is performed on three different metallic materials: Al7075, Ti6Al4V and Ni bulk of commercial purity. Two main damage mechanisms are observed in the early stages of erosion, namely peening at the macro-scale and pitting at the micro-scale. Notable results include the influence of the initial roughness of the sample down to the sub-micron scale grooves created by polishing, since they appear to be pitting initiation zones.

Using laser interferometry, it is shown that the arithmetic mean roughness $R_a$ increases in the early stages of erosion as a linear function of the total received energy, defined as the cumulative kinetic energy of the droplets, for the PJET technique. The skewness parameter $R_{sk}$, which represents the asymmetry of the profile with respect to the mean surface elevation, seems to be the most representative parameter in the present work. It shows a decreasing trend, explained by the increasing number of pits and their deepening as erosion progresses. Finally, the evolution of the sharpness of the damaged zones, represented by the kurtosis $R_{ku}$, depends on the droplet speeds but quickly stabilizes. Despite the difference in erosion rate, a correlation can be established between 18 hours of exposure in the WARER at 120 m/s and either 9 000 impacts at 225 m/s or 15 000 impacts at 180 m/s in the PJET under reference conditions.

Based on roughness measurements, the performance of several metallic samples is compared and a material selection approach towards a performance index is taken. Most interestingly, the analysis of Al7075 alloys highlights the influence of increased hardness and ductility by age-hardening and friction stir processing on the resistance to water droplet erosion. While increased hardness leads to better performance, the ductility does not seem to influence the resistance to water droplet erosion in the early stages of damage. The two main macroscopic material properties studied in the present work are the yield strength $\sigma_y$ and Young's modulus $E$. Most existing material performance indices assessing the resistance to water droplet erosion correctly identify the superiority of Ti6Al4V but fail to predict the behavior of Ni bulk which has experimentally slightly better performance than Al7075. Therefore, a new performance index adding the influence of density, namely $I_4 = \rho\sigma_y^2 E$, is analyzed and seems to correspond to the experimentally observed ranking for the materials tested in the present work. Still, other properties such as toughness, ductility or strain-hardening are likely to have an influence on the resistance to WDE in more advanced erosion stages, which are not studied here. The response under high strain rate should also be further studied to identify a potentially universal performance index.

## Acknowledgements

I would like to express special thanks to Pierre Bollen for his kind support in the daily supervision of my work, bringing insightful reflections on the experiments, results and discussions. His interest, commitment and availability were of great value for all of my questions and reflections.

Thank you to my promoter Pr. Thomas Pardoen for his supervision and enthusiasm in this project. I am also grateful to Pr. Evelyne Van Ruymbeke and Pr. Laurent Delannay for accepting to be members of the jury.

I am deeply thankful to Yves Marchal for allowing me into the facilities of *Sonaca*, which greatly contributed to the results of the present work. Special thanks to Fabrice Simoes and Michel Culot who kindly supported my experiments at *Sonaca* with their experience and know-how.

I would also like to thank all of the researchers and staff members of the *UCLouvain* who helped me in my experiments. Many thanks to Laurence Ryelandt, Olivier Poncelet, Matthieu Lezaack, Sophie Ryelandt, Mark Sinaeve, Alban Matton and Jonathan Lorfevre to name but a few.

Finally, huge thank you to my family for the proof-reading. Always present to cheer, they are my best supporters.

## List of abbreviations used

| Abbreviation | Meaning |
|---|---|
| CLSM | Confocal laser scanning microscopy |
| EDX | Energy-dispersive X-ray spectroscopy |
| LIE | Liquid impingement erosion |
| PJET | Pulsating jet erosion test |
| SEM | Scanning electron microscopy |
| WARER | Whirling arm rain erosion rig |
| WDE | Water droplet erosion |

Table 1: List of abbreviations used.

## List of symbols used

| Symbol | Meaning | Units |
|---|---|---|
| $\rho_0$ | Mass density of the liquid | $kg/m^3$ |
| $c_0$ | Speed of sound in the liquid | $m/s$ |
| $v_0$ | Impact velocity | $m/s$ |
| $M_0$ | Impact Mach number | - |
| $\rho_s$ | Mass density of the impinged material | $kg/m^3$ |
| $c_s$ | Speed of sound in the impinged material | $m/s$ |
| $v_j$ | Lateral jetting velocity | $m/s$ |
| $r_0$ | Radius of the droplet | $m$ |
| $n$ | Number of impacts | - |
| $\varepsilon_{tot}$ | Total energy received | J |
| $HV$ | Vickers Hardness | - |
| $\sigma_u$ | Ultimate tensile strength | $MPa$ |
| $\sigma_y$ | Yield strength | $MPa$ |
| $E$ | Young's modulus | $GPa$ |
| $R_a$ | Arithmetic mean roughness parameter | nm |
| $R_{ku}$ | Kurtosis roughness parameter | - |
| $R_{sk}$ | Skewness roughness parameter | - |

Table 2: List of symbols used.

# Contents

# Introduction

What do aeronautic transportation and wind power have in common ? Both domains are under strong demand and increasingly elaborate performances are sought. Another similarity is the fact that both are exposed to severe erosive conditions due to the high speed impact with water droplets, called water droplet erosion (WDE) or liquid impingement erosion (LIE).

If the example of commercial flights is taken, fees associated to runway occupation and passengers patience keep adding pressure to reduce delays on the schedule. This leads to aircraft taking-off and landing almost regardless of the weather conditions. As a result, airplanes, and especially their leading edges, are exposed to potential damage due to rainfall erosion. Heavy rain during take-off or landing as well as storms encounters during flights can cause droplets to impact the leading edges at speeds which can be well above 100 m/s. Erosion is less present at cruising altitude despite the higher speed of the plane because of the absence of macro-sized droplets above the clouds. From an aerodynamic point of view, the wings of airplanes need to keep a low surface roughness to delay the laminar to turbulent flow transition on the wing profile, crucial for the lift. The evolution towards carbon fiber reinforced polymers in airplanes wings for their high strength to weight ratio brought back erosion in the spotlight since they have a poor resistance to water droplet erosion, as opposed to their aluminum predecessor. In the context of aviation, light weight material solutions with high resistance to water droplet erosion and extended lifetime are long awaited.

Wind turbines are also exposed to severe erosion. In order to reach higher power, the trend is to develop larger wind turbines, with increasingly long blades. Due to this design, the tip reaches speeds at which impacts with rain droplets can cause severe erosion, similarly as for airplanes leading edges. In addition, wind turbines are increasingly located in off-shore farms, where the weather conditions are oftentimes harsher than inland. This erosion increases the drag significantly and decreases the lift of the blades, which can cause an annual loss of energy production up to 25%.

As opposed to airplanes, wind turbines can be slowed down in heavy rain conditions in order to protect them but are then not used to their full power. Maintenance and repair of damaged blades can be extremely costly and time-consuming, especially for off-shore wind turbines. Besides being more difficult to reach for maintenance, off-shore wind turbines are faced with a more humid and corrosive environment. The objective is therefore to develop materials with higher erosion resistance while maintaining the aerodynamic properties of the blades as well as a good balance between structural integrity and weight.

In order to protect blades and leading edges from water droplet erosion, coatings can be placed on the structural support. These protective solutions can be electroplated nickel, cladded aluminum plates or polymeric surface layers such as gelcoats or tapes. Depending on the material properties of the protection layer, different erosion mechanisms happen ranging from surface roughening to complete layer decohesion.

The present thesis focuses on the erosion caused by water droplets impacting effective areas. This work aims at defining a general performance index based on macroscopic material properties which would allow to rank the ability of materials to resist rain erosion by identifying the relevant parameters. Indeed, up to now, very few standards exist when it comes to characterizing erosion, mainly due to the high dependence on the operating conditions.

The first section is a review of the current state of literature on water droplet erosion and the mechanisms responsible for leading edge erosion. In this section, three aspects linked to the impingement, namely the impact loading, the material response and the damage mechanisms, are developed and the existing models are reviewed. Then, the parameters influencing erosion both from the operating conditions and the material point of view are analyzed, as well as the material performance indices which have been developed so far. Finally, the solutions currently used to protect leading edges of airplanes and wind turbines are presented.

The second section consists in a comparison of both water droplet erosion test facilities used in the present work, namely the pulsating jet erosion test (PJET) and the whirling arm rain erosion rig (WARER). While the PJET approach is to accelerate the droplets and project them against the sample, the WARER accelerates the samples and smashes them with vertically falling droplets. This section will show that both techniques are used in research and give similar erosion behavior provided that the material has a sufficiently fast dynamic response and is not influenced by the local heating triggered by the repetitive impingement. Indeed, both techniques differ in terms of impact rate due to the difference in size of the impinged zone.

Then, in the third section, the methodology followed in the experiments is described. The choice of parameters in both erosion techniques, as close as possible to real-life conditions, is motivated. This section also presents three categories of materials tested, namely aluminum, titanium and nickel. Although other samples of these categories are also tested, the present work focuses on five materials: Al7075 T4, Al7075 T6, Al7075 FSP T6, Ti6Al4V and Ni bulk. The aluminum samples were chosen to have three similar samples which only differ in hardness and ductility, via heat treatment and friction stir processing. Indeed, the friction stir processing, which consists in locally modifying the microstructure via solid state mixing, allows to break and spread the inclusions, leaving a material with improved ductility. Ti6Al4V and Ni bulk were chosen for their high strength to weight ratio, as well as for their corrosion resistance, interesting features for aerospace applications for instance. The third section ends with a presentation of the techniques used to assess erosion and analyze the samples. The samples were mechanically tested, as well as observed with different microscopy techniques. The roughness parameters obtained with laser interferometry, which are of great use for the assessment of erosion in the early stages of damage, are also presented.

The results and their analysis come in the fourth section. The mechanical properties are compared with the literature and the erosion mechanisms at different scales are illustrated with scanning electron microscopy. The evolution of the most relevant roughness parameters with respect to the number of impacts is also analyzed. In addition, a correlation between both PJET and WARER erosion techniques is presented. Finally, a case of coating decohesion is illustrated, as opposed to bulk material damage for the aforementioned samples.

The fifth and last section of the present work is a discussion on the erosion test results, crossed with the state of the art to work towards a material performance index. Based on material properties charts, as done by M. Ashby [1], a material selection approach is taken to highlight an objective, namely to minimize erosion damage, from which a material performance index should be deduced. This section highlights the importance of many constraints such as the toughness, thermal expansion, ductility or dynamic response of the material and aims at opening the discussion for future research.

# 1 State of the art

## 1.1 Context

Water droplet erosion (WDE) is a form of material wear caused by the impact of high speed liquid particles. The substrate undergoes progressive material loss, usually in the form of small particles or fragments, due to the repeated dynamic forces on the surface. This phenomenon is also called liquid impingement erosion (LIE). [2]

This phenomenon is observed in airplanes radomes or wings leading edges as well as on blades of wind turbines or power generation steam turbines for example. WDE is in fact encountered in every high speed application operating in a gaseous phase carrying discrete water droplets.

WDE is a damage mechanism which has important negative implications on performance. For example, in the case of steam turbine blades, erosion causes over time a mass imbalance which triggers vibrations. This limits the lifetime of the turbine and decreases the energy production. In the aerospace industry, WDE causes pitting of the airfoils or paint stripping which is detrimental from an aerodynamic point of view. In wind turbines, WDE decreases significantly the lift and increases the drag of the blades, hence decreasing their energy production over time.

In the field of wind energy, the size of the turbine blades constantly increases to reach higher power and the number of off-shore applications rises. Off-shore wind turbines have more freedom in terms of height, blade length or noise emission as they are generally not visible from the shore and are situated far from residential areas. As opposed to airplanes which can be regularly and rather easily inspected on the ground, maintenance of off-shore wind turbines is a complex process which requires heavy equipment. The combination of large blades, harsh weather conditions ashore and difficult access for maintenance leads to high repair costs for the off-shore wind turbines. This puts a lot of pressure on finding durable solutions to limit WDE. Indeed, as mentioned by Castorrini et al. [3], serious erosion damage can be observed on wind turbine blades as soon as after two years of operation in severe climate conditions. The maximum power delivered by eroded turbine blades is therefore reduced by up to 25% of the rated nominal power. This is explained by an increase of the drag and a decrease of the lift by up to 314% and 53 % respectively, according to Ibrahim et al. [4]

This decrease in power efficiency due to eroded blades can jeopardize the return on carbon used to manufacture and assemble the turbines. Reducing erosion damage, or at least postponing the early effects on the power efficiency, is critical to ensure a quick return on carbon invested. In addition, blades which undergo fast erosion damage need more frequent maintenance and repair, which increases the downtime of the wind turbines and their operating costs. These problems motivate the quest for erosion resistant materials, to limit as much as possible the shortfall in energy and the need for frequent maintenance.

In the aerospace industry, leading edges of airplane wings are the most heavily exposed parts to WDE, due to the normal angle of the impacts. Historically, airplanes were mostly manufactured with aluminum, for its high strength to weight ratio. That was until the development of polymer-based composites, especially carbon fiber reinforced polymers, which outperformed the aluminum alloys previously used, due to their very low weight. However, as opposed to aluminum alloys, composites exhibit poor impact and erosion resistance. Therefore, decreasing the weight of the airplanes by using composites brought the problem of WDE on the leading edges, which required the development of erosion resistant protections. Leading edge protection solutions include pure aluminum cladding on anodized aluminum 2024 alloy. This allows a life time of over 25-30 years, which corresponds to the operation lifespan of most airplanes. Leading edges have a shorter lifetime in airplanes flying regularly through tropical rainfalls, where larger and heavier droplets cause much more severe erosion damage.

One should mention that research is made in sandwich hybrid structures combining the high strength to weight ratio of the inner structure with the improved erosion and impact resistance of the sheet faces. As mentioned by Castanie et al. [5], sandwich structures are usually made of a polymeric honeycomb structure sandwiched with sheets of carbon fiber reinforced composites or aluminum alloys. This is however not yet frequently used for leading edges but rather for non-structural parts or for pressurized fuselage. Despite their improved performances, hybrid sandwich structures are difficult to manufacture and defects can have very serious structural implications. As a result, although most of the fuselage and wings of flagship commercial planes *Airbus A350* and *Boeing 787* are made of carbon fiber reinforced composite, their leading edges are still made of aluminum alloys.

To develop an erosion model, three points need to be considered: the impact loading, the material response and the damage mechanisms.

## 1.2 Impact loading - Pressure increase

Upon impact with the material, the liquid droplet causes an increase of pressure inside the substrate. Several theories modeled this impact pressure, of which the simplest is the water-hammer pressure. The pressure rise due to the impact can be simply approximated as in equation (1).

$$\mathit{\Delta} P_{w-h} = \rho_0 c_0 v_0 \tag{1}$$

In equation (1), the parameters are the density of the liquid $\rho_0$, the speed of sound waves in the liquid $c_0$ and the impact velocity $v_0$. The water-hammer pressure model follows Engel's earlier model which included an additional parameter to consider the shape of the droplet. The water-hammer equation gives a good approximation of the pressure rise within the material, especially for low impact speed. Besides constant speed of sound and liquid density, this model assumes that the substrate material is perfectly rigid, as highlighted by Bartolomé et al. [6] Another limitation of this model is that it is a one dimension equation. To include the effect of the shock waves generated which propagate in the material, Heymann came with a two dimensional, corrected water-hammer equation (2), reported by Li et al. [7]

$$\mathit{\Delta} P_{Heymann} = \rho_0 c_0 v_0 \left[1 + k M_0\right] \tag{2}$$

In equation (2), $k$ is a dimensionless constant and the ratio $M_0 = \frac{v_0}{c_0}$ is called the impact Mach number. Heymann showed that a constant equal to $k = 2$ fits the reality for an impact Mach number up to $M_0 = 1.2$, as reported by Tatekura et al. [8] This greatly broadens the range of impact speeds at which the model is valid compared to the water-hammer pressure.

Keegan et al. [9] showed a good correlation between the modified water-hammer pressure and the maximum Von Mises stress computed based on the *ANSYS Design Modeler* tool. The modified water-hammer pressure is based on the water-hammer pressure equation but also considers the impinged material properties, as illustrated in equation (3).

$$\mathit{\Delta} P_{mw-h} = \frac{\rho_0 c_0 \rho_s c_s v_0}{\rho_0 c_0 + \rho_s c_s} \tag{3}$$

In equation (3), $\rho_s$ and $c_s$ are the target material density and the speed of sound through this material, respectively.

Another approach to model the pressure rise due to the interaction between the shock wave and the liquid impact is the stiffened-gas equation, as described by Tatekura et al. [8] Using the stiffened-gas model, the pressure rise due to the liquid-solid impact is given in equation (4), where another constant is introduced $\gamma$, which is about $\gamma = 4.4$ for water.

$$\varDelta P_{sg} = \rho_0 c_0 v_0 \left[ \frac{(\gamma+1)M_0}{4} + \sqrt{1 + \frac{(\gamma+1)^2 M_0^2}{16}} \right] \tag{4}$$

It is interesting to note that all four models are developed based on the same conservation equations, namely the conservation of mass, momentum and energy. However, different models were used for the speed of the waves propagation within the material. Therefore, the predicted pressure rise upon impact differs between the models.

Tatekura et al. [8] showed that when the size of the mesh in finite elements computation is decreased, the maximum central pressure converges towards the stiffened gas model prediction. This requires extremely high resolution both in temporal and spatial domains to obtain the numerical results confirming the stiffened-gas pressure rise given by the expression (4). Note that in WDE, due to the short duration of the impact, the models consider that the deformation of the substrate is mainly elastic.

## 1.3 Material response - Waves creation and propagation

At the instant of the impact between the water droplet and the substrate surface, two main mechanisms happen. On one hand, the impact causes a pressure rise right below the surface of the material, which induces the propagation of stress waves in the substrate. On the other hand, a lateral outflow of water, called lateral jetting, creates shearing effect and can rip out surface irregularities.

As a consequence of the water droplet impacting the substrate, stress waves are created inside the material and propagate in various directions. This causes a surface hardening and residual compressive stresses within the material. Three main types of waves can be identified: compression, shear and Rayleigh. Due to the compressibility of the liquid, a shock wave is also created in the droplet in the form of higher density region. These phenomena are illustrated in Figure 1.

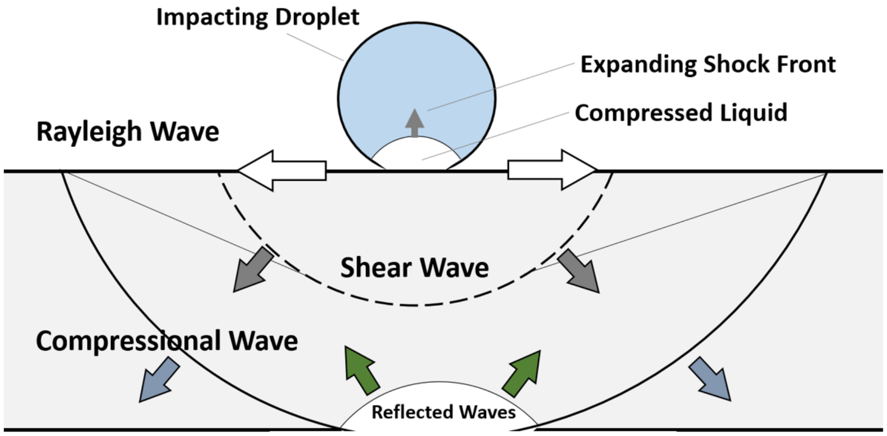

Figure 1: Schematic representation of the waves developed in the substrate and the droplet due to the liquid-solid impact. Three main types of waves can be seen in the substrate: compression, shear and Rayleigh. Image from [2]

The compression and shear waves travel respectively in a longitudinal and transverse direction in the substrate while the Rayleigh waves move along the surface. According to Slot et al. [10], the Rayleigh waves decay along the radial direction as $\frac{1}{\sqrt{r}}$ on the surface while the bulk waves decay as $\frac{1}{r}$. Therefore, the stress-strain state is dominated by the Rayleigh waves in the substrate.

The key to understand and model WDE, as stated by Na Li et al. [11], is to obtain the transient stress field inside the solid upon impact and locate the most critical, peak stresses as a function of the impact speed and the droplet diameter.

The most critical phenomenon in WDE due to these waves is the presence of a high tensile stress right behind the propagating Rayleigh wave, which can cause crack initiation on the substrate surface. The speed of the wave propagation depends on the material and it was shown by Slot et al. [10] that softer materials take longer to reach the maximum tensile strength. As a result, the stress from consecutive liquid droplets impact can build up more significantly in soft polymers than in hard metals for example due to the slower Rayleigh waves propagation in the former.

As mentioned by Adler [12], the droplet impact creates zones of significant tensile stresses within the substrate, which can initiate fracture in brittle materials. The impact between the water droplet and the substrate can be divided in three stages: center stamping zone, annular digging zone and free jetting zone. Indeed, the circular intersection between the liquid front and the substrate expands as the droplet deforms. This circular intersection expands at speeds much higher than the impact speed and the compression wavefront propagation, as shown by Tatekura et al. [8] Note that the curvature of the wavefront continuously varies as the droplet deforms on the substrate upon impact. As reported by Slot et al. [13], the radius within which the water-hammer pressure model can be used is defined when the velocity of the expanding circular contact boundary decreases below the speed of sound in water, therefore the speed of the wavefront.

In addition, the pressure distribution in the water droplet is not uniform and varies with time. The highest pressure is observed at the contact edge point between the expanding droplet and the substrate. Once this wave breaks away from the liquid droplet, it releases its impact pressure into kinetic energy in the form of a fast outflow of water, called lateral jetting. The speed of this lateral jet can be several times higher than the impact speed. As reported by H.S. Kirols [14], the lateral jetting speed $v_j$ can be obtained with equation (5), where $c_s$ is the speed of sound in the substrate and $v_0$ is the impact velocity.

$$v_j = \sqrt{2c_s v_0} \tag{5}$$

This lateral jet of water can reach extremely high velocities. For example, based on equation (5), a droplet impacting at $v_0 = 180$ m/s an aluminum sample - with speed of sound around $c_s = 6000$ m/s - creates a lateral jet with a velocity up to 1 500 m/s. This high speed lateral jetting rips out surface irregularities and is responsible for the material loss observed in erosion. The initial impacts trigger topological changes of the surface, then hydraulic penetration occurs and finally the lateral jetting causes the main part of the damage by expelling matter out.

Once a critical maximum pressure is reached within the substrate, the shock front detaches from the droplet and the lateral outflow begins. Rui Li et al. [7] showed that the maximum pressure in the substrate is undergone right before the jetting occurs, not at the first contact point. As suggested by Na Li et al. [11], a wave model can be used to describe the liquid-solid impact until the shock wave exits the liquid droplet. It is also interesting to note that the maximum stress in the substrate is reached significantly later than the maximum pressure in the droplet.

Slot et al. [10] showed that in the tomography of ZnSe exposed to a droplet of 2 mm diameter at 222 m/s, no cracks can be observed below 140 µm depth. This exemplifies that for substrates with a sufficient thickness the influence of the reflective waves is negligible.

## 1.4 Damage mechanisms - Erosion stages

In general, conventions represent erosion as cumulative volume or mass loss as a function of cumulative exposure duration. This cumulative exposure duration can be replaced by the kinetic energy of the droplets normalized to the impacted area, as done by Bartolomé et al. [6]

The evolution of erosion through time can be decomposed into five stages: incubation, acceleration, maximum erosion rate, deceleration and terminal steady erosion rate. These stages are illustrated in a typical S-shaped graph as in Figure 2.

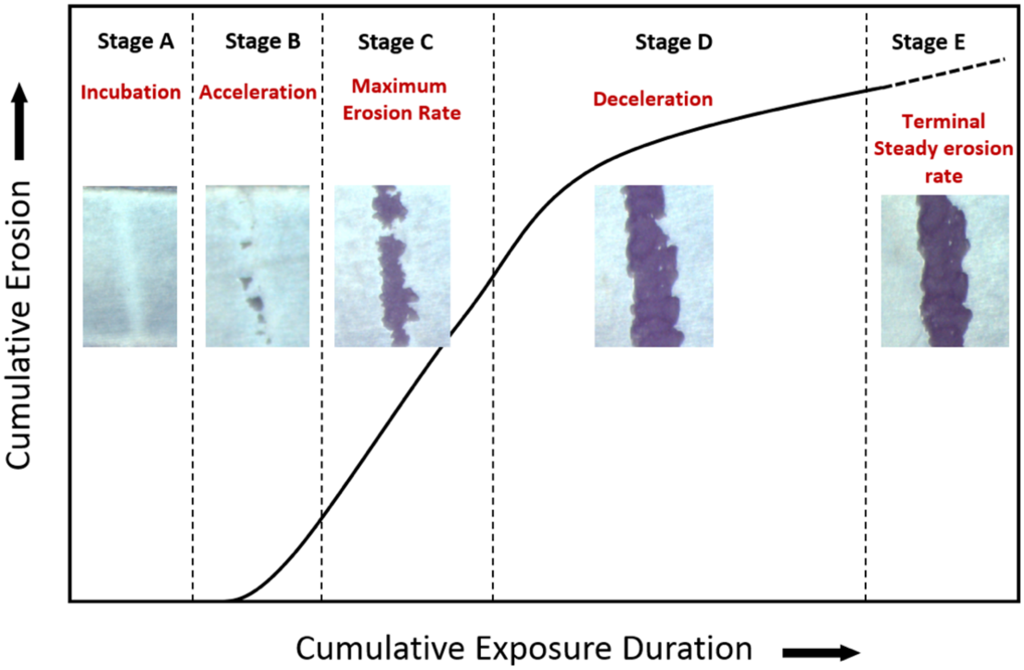

Figure 2: Typical evolution of the cumulative erosion as a function of the cumulative exposure duration. Image from [2]

The most important part of the erosion mechanism is the incubation period. During this stage, the water droplets alter the surface topography without causing any material loss. The roughness of the material increases but no major failure mechanism occurs. In fact, this stage illustrates the distinction between water droplet impingement and erosion. The impingement results in an alteration of the surface roughness without causing any erosion during the incubation period, as mentioned by Gohardani. [15] The increase of roughness can be detrimental from a fluid mechanics or aerodynamic point of view, such as a laminar-turbulent transition happening too early on a wing profile. Still, the integrity of the material is preserved. Increasing the incubation period of materials is probably the most challenging part to increase the erosion performance. Indeed, the end of life of a coating can be defined as the end of the incubation period, when the substrate starts loosing matter. For example, extending the incubation time of wind turbine blades enables longer period of use at full power capacity.

The second stage is the acceleration stage in which pits are created and grow due to coalescence, leading to some matter being lost. Then, the maximum erosion phase is observed during which the erosion rate remains constant. The fourth stage is a deceleration of the erosion rate, usually at around 50% of the maximum erosion rate because of the significant irregularities in the surface, which distribute stress differently over the substrate. Finally, the terminal stage can be either a constant erosion region or even a decline in erosion rate. In the case of brittle materials, this terminal stage can be a rapid increase of erosion rate called catastrophic failure.

As reported by Madhipoor [16], several features can be observed in the early stages of erosion. For example, circumferential surface fracture is due to the tensile stress generated around the impact point. Upon collision with the liquid droplet, the surface also starts roughening generally as small extrusions at the grain boundaries. Indeed, the damage initiation can be a slip band at the grain boundaries, leading to small features pointing out of the surface. Because of this protrusion, fractures can start propagating due to the lateral jetting of water, creating a shear on the asperity. This is illustrated schematically in Figure 3.

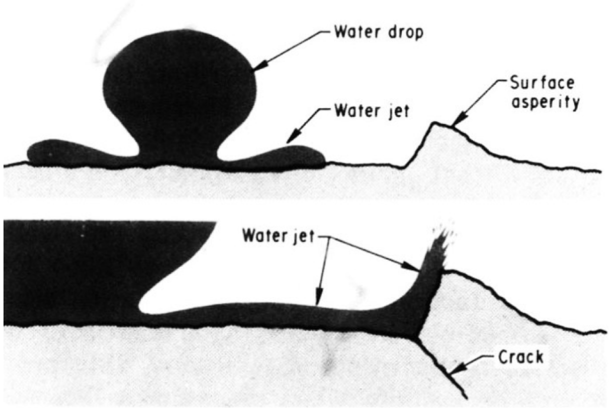

Figure 3: Due to the lateral jetting happening after the impact, the surface irregularities or asperities can be sheared out or cracks can initiate and propagate at their base. Image from Heymann et al. [17]

In ductile substrates, the material locally flows causing a localized depression. Micro- and sub-surface cracking appears due to the localized plastic deformation or due to the traveling stress waves. In the early stages, failure is often initiated at the grain boundaries.

Kirols et al. [18] showed that the initial surface roughness influences the length of the incubation stage. Indeed, on a polished surface, the water droplets will need more time to roughen the surface and thereby initiate erosion pits. Periodically polishing the surface can keep the erosion in the incubation stage indefinitely. Of course, this can only be applied to thick materials and not to surface coatings but the importance of the initial surface roughness is clearly emphasized. Polished samples also show a reduced maximum erosion rate. Limiting defects and impurities is fundamental to decrease the erosion rate. It is interesting to note that the higher the impact speed, the lower the influence of the initial surface roughness on erosion. In other words, the effect of initial roughness is more significant at low impact speed.

Among other solutions to limit damage caused by liquid impingement, surface modification can be considered. This is still a field of research but promising results can already be seen in methods such as relief structuring, ion-plasma coating or ion-plasma surface nitriding. Indeed, as illustrated by Mednikov et al. [19], combining structured surface topography with surface hardening via nitriding or ion-plasma coating allows improved erosion resistance on certain steel substrates.

To account for the accumulation of damage, the easiest method is the linear Palmgren-Miner damage accumulation model which can be written as in equation (6).

$$M = \sum_{i=1}^{j} \frac{n_i}{N_i} \tag{6}$$

In equation (6), the accumulation of $j$ different load levels is considered. $n_i$ is the number of impact cycles for the load level $i$ and $N_i$ is the number of cycles to failure at a level $i$. When $M \geq 1$, this model predicts failure. Note that this model is fatigue-based and requires prior knowledge of the cycles to failure for damage prediction, which is a strong limitation. In addition, the Palmgren-Miner model considers that the impacts are independent of each other. Despite this strong hypothesis, it can be used to predict the incubation time.

Based on the Palmgren-Miner damage accumulation model, Springer modeled the cumulative erosion curve as a function of the cumulative exposure time as two straight lines: one for the incubation period and one for the steady erosion rate. However, this model makes strong assumptions as it neglects the influence of three fundamental parameters: the material hardness, its surface roughness and the lateral jetting. Still, Ibrahim et al [4] showed that it predicts a relevant approximation of the incubation time.

Navier-Stokes equations for continuity and momentum can be used to model the impact and reaction stresses in what can be called fluid model of liquid-solid. Na Li et al. [11] showed that the displacement of the droplet can be neglected until the lateral jetting phenomenon happens. At this point, the full Navier-Stokes equations must be used. Solving simultaneously the Navier-Stokes equations for the waves in the solid substrate and the liquid droplet requires iterations until the velocity and pressure values converge for each time step, which is demanding in terms of calculating power. Na Li et al. also showed that the water-hammer pressure is an accurate and simple approximation, mostly valid for low impact speeds. At higher impact speeds, the compressibility of the liquid and the elastic deformation of the solid must be considered simultaneously.

The elasticity of the solid leads to lower stresses in the substrate while the compressibility of the liquid increases the impact pressure. Na Li et al. [11] showed that the impact speed and load duration time are the most important factors influencing the maximum stress developed in the substrate. Indeed, steady state models significantly underestimate the transient peak pressures and stresses. For that purpose, Zhou et al. [20] defined four dimensionless parameters which characterize the impact:

1. The maximum dimensionless stress in the substrate, defined as $\mathit{\Sigma} = \frac{\sigma_{e,max}}{\rho_0 c_0 v_0}$. In this expression, $\sigma_{e,max}$ is the maximum equivalent stress reached in the substrate.
2. The dimensionless influence duration time, defined as $T = \frac{t_{SB} c_0}{r_0}$ where $t_{SB}$ is the time between the first contact and the break of the shock wave off the droplet. In this expression, $r_0$ is the radius of the impacting droplet.
3. The dimensionless influence radius $R = \frac{r_{max}}{r_0}$ where $r_{max}$ is the maximum radius achieved before the shock wave breaks off.
4. The dimensionless influence depth defined as $L = \frac{l_{max}}{r_0}$ with $l_{max}$ the depth at which the maximum equivalent stress is reached.

They showed that, as long as the impact Mach number $M_0 = \frac{v_0}{c_0}$ remains constant, these four dimensionless parameters remain unchanged in the impinged material.

## 1.5 Towards an erosion performance index

Before analyzing the existing performance indices assessing the erosion resistance, let's look at the main parameters influencing WDE. As a first disclaimer, one should note that the damage caused by WDE will vary both with the erosion conditions and the intrinsic properties of the substrate exposed. Indeed, the resistance to WDE depends on a mix of parameters, such as hardness, toughness, ductility or

Young's modulus, whose relative weight in the relation depends on the impacting conditions.

Because liquids cannot sustain shear stress, only normal impacts are studied. As a matter of fact, it is the reason why mostly the leading edges of wings and blades are subject to WDE as they are faced with normal impacts, which cause the most erosion damage. This was shown by Ahmad et al. [21] in Figure 4, where the highest material loss due to WDE on a turbine blade is observed at a normal impact angle.

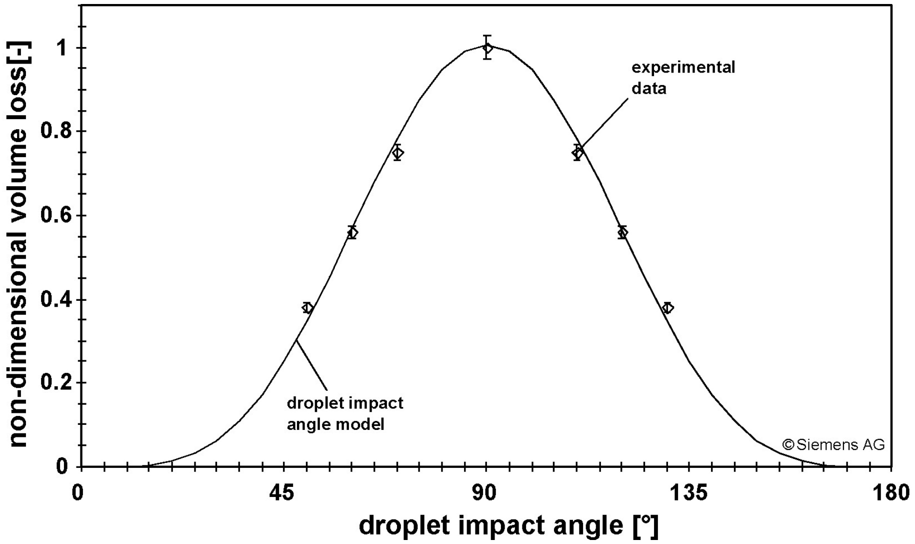

Figure 4: Normalized volume loss as a function of droplet impact angle. Image from Ahmad et al. [21]

As highlighted by Zhang et al. [22], the erosion rate increases when the temperature of the water droplet increases, due to the reduction of the viscosity of the liquid. This could be explained by the fact that the velocity of the lateral jetting increases when the viscosity of the water decreases, leading to more shear damage. On the other hand, the presence of residual water film on the substrate can act as a protecting shield, which decreases significantly the erosion rate.

From the point of view of the water droplet, the parameters influencing erosion are the impact speed, the impact angle relative to the normal of the impinged surface and the droplet diameter. The properties of falling droplets are dictated by the climatic conditions. It is interesting to note that the climatic conditions result in a non-homogeneous raindrop size distribution. Still, most conventions use spherical droplets of 2 mm diameter and a flow between 20 and 25 mm/h, which corresponds to heavy rainfall. As can be seen in Figure 5, droplets larger than 5 mm tend to take parachute-like shapes and break apart during their fall. Smaller droplets on the other hand, tend to agglomerate. From an erosion point of view, the diameter of 2 mm is, according to Ibrahim et al. [4], a compromise between the great individual effect of the large drops and the great number of impacts of smaller drops. As shown by Dina Ma [23], larger droplets cause more severe erosion because of the higher kinetic energy associated to their mass compared to smaller droplets for the same amount of water.

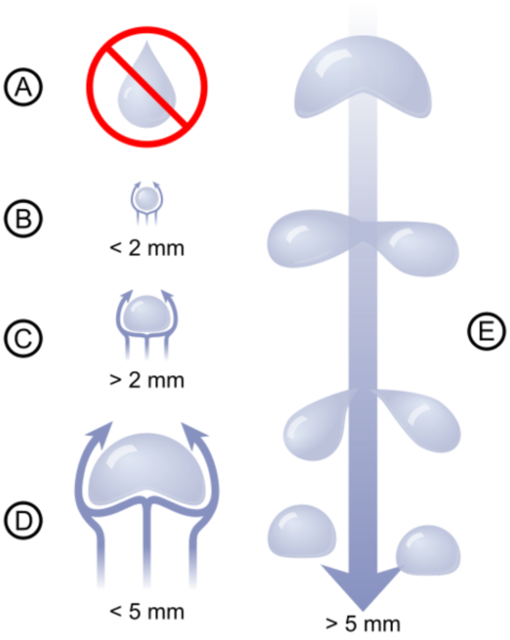

Figure 5: Evolution of the shape of falling water droplets depending on their diameter. Droplets with a diameter below 2 mm are quasi-spherical while droplets above 5 mm diameter tend to divide due to drag force exerted by air. Image from [24]

The impact speed changes the erosion mechanism from chemical to mechanical. Indeed, at speeds higher than the critical impact speed, the chemical corrosion mechanism is negligible compared to the mechanical erosion caused by the impact. Erosion rate seems to be exponentially proportional to impact speed according to the experimental data collected by Mahdipoor et al [25]. The erosion rate $ER$, defined as the rate of material loss as a function of time, can therefore be modeled as in equations (7) or (8) by Heymann:

$$ER = aV^n \tag{7}$$

$$ER = a\left(V - V_c\right)^n \tag{8}$$

Note that in equations (7) and (8), the power law parameter $n$ is fitted to the experimental data and depends intrinsically on the substrate properties. In equation (8), the parameter $V_c$ is the threshold impact velocity. As illustrated by Bech et al. [26], it corresponds to the impact velocity below which erosion due to fatigue never occurs.

Although the hardness is a measure of the ability to resist plastic penetration, the direct correlation between the hardness and the resistance to erosion only exists for materials with similar metallurgical structures, as stated by Ahmad et al. [21] Therefore, hardness alone does not give a relevant comparison basis when it comes to the resistance to water droplet erosion.

In addition, fatigue only plays a secondary role in WDE. Indeed, as shown by Ibrahim et al. [4], surface treatments which remarkably increase the fatigue resistance, such as deep rolling or laser shock peening, do not significantly increase the erosion resistance.

Heymann [17] defined the normalized erosion resistance as the rate of volume loss of a reference material divided by the rate of volume loss of the sample for the same test parameters. Based on mechanical properties, this is a first approach to a performance index. Ahmad et al. [27] formulated this material indicator equivalently but in other words as the reciprocal of the normalized volume loss of the test sample for a fixed testing duration.

A reference parameter, as suggested by Heymann [17], is the ultimate resilience $U_{r,H}$, defined as in equation (9) based on the ultimate tensile strength $\sigma_u$.

$$U_{r,H} = \frac{\sigma_u^2}{2E} \tag{9}$$

The ultimate resilience for non brittle material is better defined using the yield strength $\sigma_y$ instead of the ultimate tensile strength, as mentioned by Ahmad et al. [27] This hardness induced elastic resilience $U_r$ is defined in equation (10). It represents the ability of the material to absorb energy by elastic deformation, then to release this energy back upon unloading. It corresponds to the area under a stress-strain curve until the yield point, therefore it is the elastic deformation energy.

$$U_r = \frac{1}{2}\sigma_y \varepsilon_y = \frac{\sigma_y^2}{2E} = \frac{HV^2}{18E} \tag{10}$$

In this index, the Vickers hardness $HV$ - here the approximation $\sigma_y = \frac{HV}{3}$ is made - and Young's Modulus $E$ are the parameters influencing the erosion resistance of the impinged material.

Note that the elastic resilience is not sufficient to describe and compare the resistance to WDE as it also depends on the metallurgic structure and toughness. Indeed, once the droplet impact pressure exceeds the elastic resilience value, the material enters the plastic deformation regime. The damage undergone is linked to the toughness, defined as the amount of energy the material can absorb before failing.

Heymann [17] showed that the normalized erosion resistance increases with the hardness following a power law with an exponent close to $n = \frac{5}{2}$. He also suggested that materials containing finely dispersed small and hard particles embedded in a more ductile matrix globally show better resistance to erosion. For example, finely dispersed inclusions or intermetallic particles help increase the erosion resistance by blocking the motion of dislocations, thereby allowing an increased uniform elongation, hence a tougher behavior. As reported by H.S. Kirols [14], Heymann also defined a material index to study erosion performance as follows: $I_H = \left(\sigma_y^2 E\right)^{\frac{2}{3}}$. This correlation was experimentally determined based on the evolution of the erosion rate of steel samples. Therefore, it should be understood as a primary indication of the resistance to WDE, but the best option to evaluate the behavior of a material remains today to test the material with a WARER or a PJET.

Resistance to WDE increases with surface hardness but decreases with impact pressure. Ahmad et al. [27] showed that the erosion resistance, measured as the reciprocal of erosion rate, increases exponentially with the elastic resilience to impact pressure ratio, $\frac{U_r}{P_{imp}}$ with the impact pressure $P_{imp}$ defined as the Heymann modified water-hammer pressure. The resilience and the relaxation time between the impacts are fundamental parameters influencing the impact absorption capability of a material, as it needs to sustain repeated high strain rate deformations.

Finally, as highlighted by Mahdipoor et al. [25], the toughness, which is total energy that can be absorbed by the substrate before fracture, is an important property which affects the WDE resistance. However, due to the high strain rate undergone, the dynamic mechanical properties of the substrate should be considered, including the evolution of the toughness.

Madhipoor et al. [16] also showed that in ductile materials, the dominant mechanism in material loss initiation is the generation of crack networks and their coalescence. This can be improved by preventing the propagation of cracks through small, well spread inclusions blocking the motion of the dislocations. They also showed that inter-granular cracking is the dominating process in the early stages, during damage initiation while trans-granular cracking is more important in the advanced stages of erosion.

## 1.6 Current protection solutions

Fiber reinforced polymers, greatly used in aircraft and wind turbine manufacture for their high strength, high stiffness and low weight, have low intrinsic rain erosion resistance. They usually show low ductility and impact resistance making them poor candidates for protection against WDE. In airplanes radomes for example, the material used must be transparent to radio waves. Therefore, most metallic alloys are not suited for this application but the polymeric alternatives show a lower erosion performance, as illustrated by Tobin et al. [28] Different approaches have been tested to provide protection against WDE.

Due to their high impedance compared to polymers, metallic erosion shields only show erosion at the surface, which does not affect the adhesion with the substrate, structural material as demonstrated by Herring et al. [29]. Thanks to their higher rigidity, metallic shields limit the risk of wrinkling. However, as mentioned by Tobin et al. [30], the influence of the structural substrate should not be overlooked. Indeed, highly erosion resistant coatings can fail more rapidly if they are too thin and coated on a softer substrate. This was shown by Tobin et al. [30] where a thin laminate of TiN demonstrated rather low erosion resistance when coated on 2024 series aluminum due to the more compliant nature of the substrate. On the other hand, Lammel et al. [31] showed that depositing a thick layer of nickel on copper, itself on the composite substrate leads to little deformation, slower roughening and therefore slower WDE. It is interesting to note that Lammel et al. [31] also demonstrated that ceramics fail by fragment dislocation or delamination in erosion tests.

Polymeric materials globally display lower resistance to rain erosion than metals. Thermoplastics provide better impact and erosion resistance than thermosets in general. While thermosets usually show brittle failure, thermoplastics fail by ductile deformation, like metals. Elastomers have a good erosion resistance because of their low modulus which dissipates shock waves and impact energy while lowering the impact pressure. Thanks to this quick elastic recovery upon impact, highlighted by Ibrahim et al. [4], the stress build-up within the laminate is limited. However, if the time between successive droplet impacts is shorter than the relaxation rate of the polymer, cumulative strain will build up in the coating and lead to failure, as shown by Zhang et al. [22]

Two main approaches exist in polymer coatings, either in-mold or post-mold application.

In-mold gelcoats use similar polymers as the composite substrate matrix, often epoxy. The advantage of in-mold gel coatings is the ease of integration and a longer erosion protection due to the close affinity between the coating and the composite substrate during curing.These should have high substrate adhesion, higher mechanical strain limits than the substrate and a good resistance to UV radiations.

Post-mold applications, which can consist of paint, spray or tapes, allow a more flexible choice of materials. However, in this case, decohesion and delamination are the main failure processes due to the low dynamic impedance of the coating compared to the laminate. The most common example is polyurethane flexible coating, which is frequently used as leading edge protection. For this reason, primers need to be applied under the coating layer as shown by Verma et al. [32] As illustrated by Cortes et al. [33], adding a primer and a putty filler between the substrate and the laminate drastically improves the adhesion. These fillers, which can be clay or carbon fibers among others, can create compressive stresses or increase the hardness, as reported by Slot et al. [10]

The acoustic properties of all the layers need to be optimized and matched to prevent premature failure by delamination. The thickness of the laminate, as well as the nature of the filler, the primer and the substrate, affect the damage mechanism. Failure can appear either in the form of pits caused by direct impact and surface stresses or in the form of delamination indirectly caused by the stress at the interfaces.

Characterizing the failure resistance of the interfaces, via the adhesive strength, is of prime importance in polymer-based protection against WDE. Indeed, gelcoats and flexible polymer coatings are highly vulnerable to defects and adhesion. The presence of wrinkles, air bubbles or other defects can trigger debonding with the substrate. The low impedance of such protective solutions cause a good energy absorption of the impacting rain droplets but accelerates debonding in areas of poor adhesion. Because of this behavior, the experimental sol-gel based on polyurethane silane coating tested by Tobin et al. [30] showed a poor resistance to WDE.

Metal-matrix composite layers have been tested, such as electrodeposited Ni-SiC by Whitehead et al. [34] In this material, the hard SiC particles increased the hardness of the metallic matrix through dispersion hardening but did not improve rain erosion resistance because of various erosion mechanisms happening. In that experimental trials, the SiC particles were selectively removed by the water droplets from the Ni matrix. This change in elemental composition is not due to the chemical nature of droplets but to their speed and impact, causing hard particles erosion.

A promising category of materials is nanocrystalline metal-polymer hybrids due to their ductility, high strength and low weight. Metals layers can be deposited on polymers by physical vapor deposition, sputtering, adhesive bonding or electroplating. Due to the small grains, the metallic layer reaches high strength and high hardness while still maintaining high toughness and ductility. Three main processes can be performed to metallize polymers: wet chemical process, physical vapor deposition or adhesive cladding. As mentioned by Tomantschger et al. [35], metal coated samples absorb better energy because of the increased stiffness, which increases the peak load at failure.

## 1.7 Key elements of the state of the art

Let's summarize the key points of the current state of the art, which will be used further in this work.

The damage generated by water droplet erosion can be divided in three phenomena:

1. The **impact loading** is the pressure rise within the material due to the impingement of the liquid droplet. Several models allow to compute the highest pressure point within the material, including the water-hammer, the modified water-hammer and the stiffened-gas models. However, to identify the location where these highest stress points are generated, finite element simulation is required.
2. The second phenomenon is the **material response**, which creates different types of waves - compression, shear and Rayleigh - propagating in the material. These waves are responsible for the appearance of stresses within the material, not only right under the impinged droplet. Indeed, due to the reflection of these stress waves and their interaction, stresses build up in the impinged material.
3. The **damage mechanisms**, which will be the most used in this work, are the visible consequences of the impingement, in the form of failure. Several stages of the erosion can be observed, of which the incubation is the most important. During this stage, the topography of the material is altered without significant material loss. In addition, lateral jetting occurs, projecting liquid outwards at velocities even higher than the impacting speed. The damage mechanisms include cracks and pits

initiation, followed by their growth and coalescence. These phenomena define different erosion stages, with various erosion rates, until catastrophic failure.

The parameters influencing the water droplet erosion can be divided in conditions-related and materials-related.

- From the **erosion conditions** point of view, the main parameters are the droplet diameter, its speed and the impact angle. This is dictated in practical applications by the climatic conditions in which the application takes place. Since these conditions affect significantly the erosion behavior, standards should be established to compare quantitatively the performance of materials.
- The **materials properties** influencing the resistance to WDE include the hardness and Young's modulus, often reported as the main parameters. However, properties such as the density, ultimate tensile strength and toughness should also be considered, as well as the dynamic response under high strain rate. A material performance index ranking materials solely on their macroscopic mechanical properties is still under research and is one of the aims of the present work.

Finally, current protecting solutions for leading edges of airplanes wings or wind turbines blades include metallic erosion shield, in-mold polymeric gelcoats, tapes or paints of thermosets or elastomers. The main failure mechanisms in such coatings is the delamination from the substrate due to the stress build-up at the interface.

# 2 Comparison of WDE test facilities

When it comes to designing an experimental machine to create rain erosion conditions, two main approaches can be taken. Either accelerate the sample up to the testing speed and make it smash quasi-stationary controlled droplets, as an airplane would fly through a rainfall. This is the technique used in the materials and process engineering (IMAP) department at *UCLouvain* and is called whirling arm rain erosion rig (WARER). The other approach, used at *Sonaca*, is to accelerate the water droplets and project them at high speed on the fixed sample. This technique is called pulsating jet erosion test (PJET). This section compares both experimental machines and the range of parameters achievable in both cases.

## 2.1 Whirling Arm Rain Erosion Rig (WARER)

In the case of the whirling arm rain erosion rig (WARER), the setup consists of an arm on both extremities of which samples are attached, rotating in a controlled rainfall environment. The free falling water droplets are therefore hit by the samples at impact speeds which can be fine-tuned.

The experimental setup available at *UCLouvain*, developed by P. Bollen, is based on this technique. The rainfall is simulated through 32 needles, fed by a continuous and controllable water distribution system. The water dispensing system uses filtered tap water, dispatched uniformly into the needles, each producing droplets of around 2 mm diameter. The droplets fall towards the region of impact through tubes to protect them from the airflow which would highly influence the droplet fall path. The whirling arm set-up is illustrated in Figure 6.

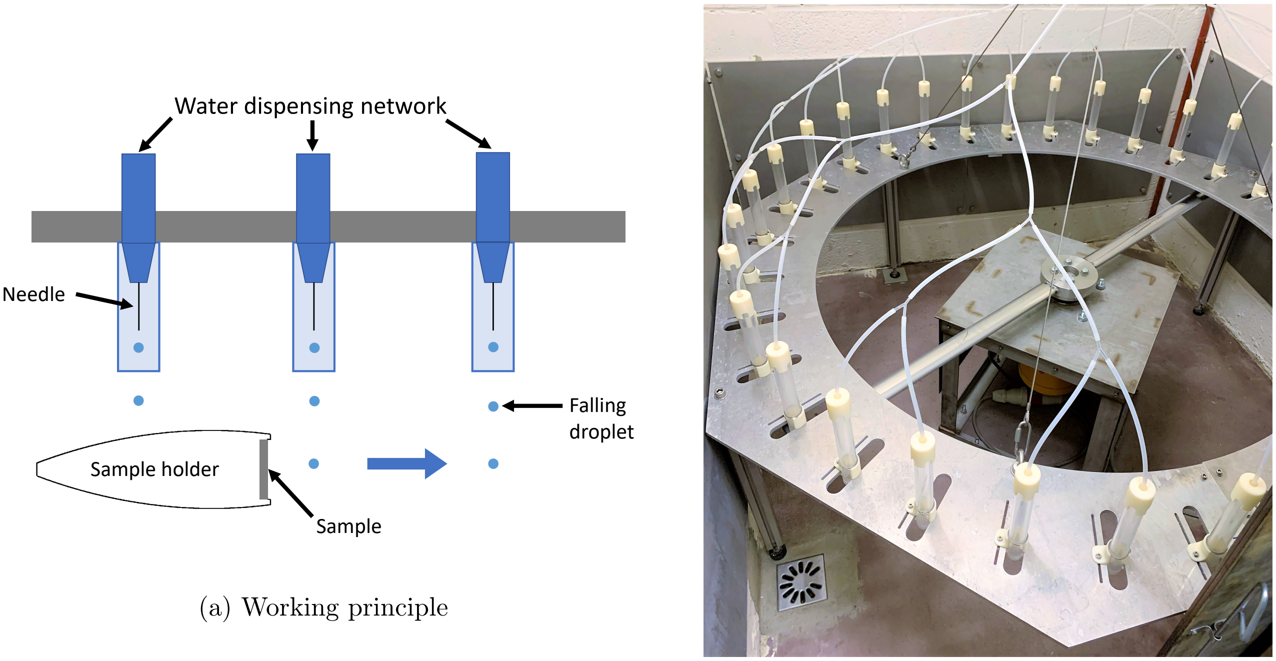

(a) Working principle

(b) WARER used at *UCLouvain*

Figure 6: Whirling arm rain erosion rig (WARER) used at *UCLouvain* for water droplet erosion tests. Figure (a) shows a schematic representation of the working principle while Figure (b) is a picture of the actual machine.

The droplets fall at a frequency such that the equivalent rain intensity is 20 mm/h, a standard heavy rain value. The water is not reused and its temperature is not controlled. Because of the 7 kW motor and the prolonged testing duration, the temperature of the experimental set-up rises. This could jeopardize the droplet formation as the viscosity of water is influenced by the temperature. As a result, the procedure used is to stop the machine after 3 hours of use, to let it cool down before starting it again. The needles were checked after each period to ensure the proper formation of droplets. Droplets of the relevant size and correct frequency were systematically observed despite the rise in temperature in the room.

These controlled droplets are hit by the samples placed on the extremities of the whirling arm. The samples consist in disks of 30 mm diameter with a maximum thickness of 2 mm, held by a 1 mm circular lip. As a result, the exposed area is a disk of 28 mm diameter. The whirling arm can rotate at speeds corresponding to up to 140 m/s at the sample location.

However, to prevent the overheating of the motor, all the tests were performed at a rotating speed of 1500 rpm, which corresponds to around 120 m/s at the radius where the samples are placed. At 20 mm/h equivalent rainfall, each of the 32 needles let a droplet fall at a rate of 2.51 droplets/s. Since the arm is rotating at 1500 rpm, the head takes 0.04 s to do a complete rotation, which means one can assume that every droplet is impacted by the rotating sample. As a result, 80.21 droplets/s dispensed on average by the 32 needles determine the impact frequency of 40 impacts/s, or 40 Hz, per sample.

In the present thesis, the standard conditions used are an impact speed of 120 m/s, with a rainfall equivalent of 20 mm/h by batches of 3 hours.

Note that standard test methods have been developed by the American Society for Testing and Materials: *ASTM G73-10 - Standard Test Method for Liquid Impingement Erosion Using Rotating Apparatus.* [36]

## 2.2 Pulsating Jet Erosion Test (PJET)

The other method consists in accelerating water droplets with compressed air and projecting them onto the surface of the sample surface in the form of a pulsated water jet. This technique is called pulsating jet erosion test (PJET) and is used at *Sonaca* to assess the erosion resistance of their leading edge protecting materials.

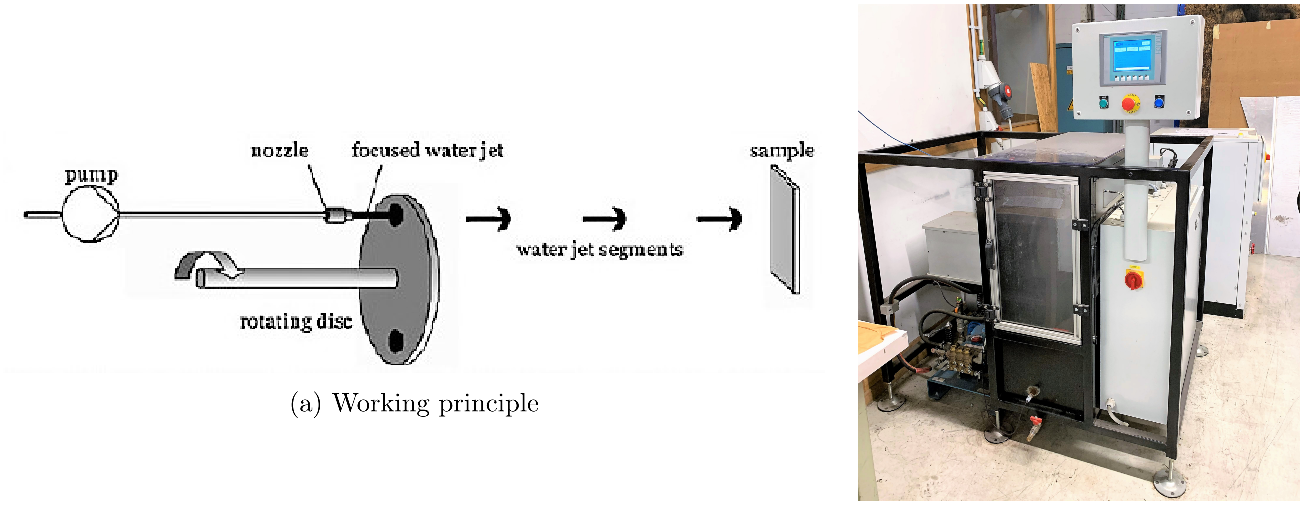

(a) Working principle

(b) PJET used at *Sonaca*

Figure 7: Pulsating jet erosion test (PJET) used at *Sonaca* for water droplet erosion tests. Figure (a) shows a schematic representation of the working principle from Keegan et al. [9] while Figure (b) is a picture of the actual machine.

As illustrated in Figure 7, a nozzle creates a continuous high speed water jet which is chopped into pulsating jet of 2 mm diameter droplets projected to the sample. The PJET available at *Sonaca* reaches an impact frequency of 40 Hz, which is equivalent to a rainfall rate of 25 mm/h. The machine is calibrated in terms of pressure to have impact speeds ranging from 180 m/s to 225 m/s. The erosion zone created by the PJET technique is concentrated on a circular region with a diameter around 1.5 mm. Therefore, the erosion zone is limited to about the size of the impacting droplets, as opposed to the WARER. Note that the water used in the PJET is collected, filtered and then recycled in the circuit. Therefore, its temperature is controlled and maintained at 10°C thanks to an external cooler.

According to Zhang et al. [37], the substrate curvature and the water-nozzle distance do not influence the erosion conditions. On the other hand, the accumulation of a water layer on the surface of the substrate can increase the erosion resistance due to the cushioning effect. Therefore, in certain PJET set-ups, compressed air is blown on the surface of the sample to remove this water film during the experimental tests. Indeed, it was shown by Brunton [38] and Rochester [39] that when the water droplets hit the liquid film, the latter deforms while absorbing some of the kinetic energy of the droplet and the pressure waves diverge through the film thickness. Both phenomena reduce the pressure on the substrate.

## 2.3 Comparison

Both methods have their limitations. In the case of the PJET, the erosion only takes place on a restricted area of the sample, with a high impact rate, leaving little time for the material to recover from the previous impacts. In the case of the whirling arm (WARER), unless working under extremely clean conditions, impacts with solid particles in suspension in the air are inevitable. In addition, as shown by Bech et al. [26], both techniques lead to idealized droplet conditions compared to natural rain, where the rainfall intensity and droplet size distribution are highly variable, depending on the meteorologic conditions.

Direct correlation between PJET and whirling arm test results cannot be made because of the significantly different impact mechanisms and associated energy absorption. Indeed, although both techniques have the same absolute frequency of impact (40 Hz), the PJET technology concentrates these impacts on a 1.5 mm diameter zone while the whirling arm distributes the droplets in a more random way over the 28 mm diameter disk sample. According to Zhang et al. [37], the PJET gives a quick first insight of the erosion mechanisms while the whirling arm test gives results closer to real conditions.

Still, as shown by Tobin et al. [28], despite the difference in frequency of impacts per surface area between the PJET and whirling arm tested samples, a correlation can be found in the results. For the aircraft aluminum Al2024 material tested in their article, they could establish a correlation between 1000 impacts using the PJET and 15 minutes exposure using the WARER, both for impact velocity of 180 m/s. This only holds true for materials like metals with a fast spring back which have time to relax between two impacts, as opposed to polymer coatings. In addition, due to the higher frequency of impacts per unit area in the PJET, the material locally heats up. While this phenomenon is mostly negligible for metals, it can significantly influence the material response in the case of polymers. Again, it shows that a general correlation cannot be established between both techniques due to the difference in erosion conditions.

Thanks to confocal laser scanning microscopy (CLSM), laser interferometry or 3D digital microscopy, the primary profiles topography - including roughness parameters such as $R_a$ or $R_z$ - can be used to correlate the results from WARER and PJET at different test speeds. Then the materials can be ranked based on the incubation time and based on the lowest primary profile. Indeed, from an aerodynamic point of view, the ideal situation is for the wing surface to remain as smooth as possible, for as long as possible.

However, one should be careful when comparing surface roughness $R_a$ values as this corresponds to an average of the profile. Very different profile topographies can lead to a similar $R_a$ value. In addition, past the incubation period, the surface topography starts to vary considerably, making the comparison more difficult. For example, when a coating is eroded and starts delaminating, the $R_a$ value measured may suddenly decrease as it does not consider the coating anymore but the freshly exposed substrate material instead, as mentioned by Tobin et al. [40] A more thorough discussion on the relevant roughness parameters is made in a subsequent section.

# 3 Methodology and experiments

## 3.1 Erosion techniques

### 3.1.1 WARER calibration and parameters

The first step of the experimental part of the thesis was to ensure the proper functioning of the WARER developed at *UCLouvain*. Based on previous numerical simulation, the droplet dispensers were aligned 10 mm closer to the center compared to the center of the rotating samples. This horizontal deviation is meant to counteract the centrifugal effect the droplets undergo in a system rotating at such high speed. To check whether this alignment indeed leads to most impacts on the center of the samples, disks of unidirectional carbon fiber reinforced composite polymers have been submitted to the machine. The epoxy resin matrix of the composites used is an aerospace grade, similar to *Hexcel HexFlow RTM 6* [41] or to *Solvay Cycom 977-2*. [42] [43] Although toughened and widely used for resin transfer molding, these composites are known to have a poor resistance to erosion, due to the low tensile modulus ($E \approx 3$ GPa) and low tensile strength ($\sigma_u \approx 80$ MPa) of the epoxy resin compared to metallic protection solutions. It was therefore chosen to quickly assess which zones are exposed to erosion.

A first disk of this type of composite was submitted, for a total duration of 3h to the whirling arm at standard conditions, that is at 120 m/s impact speed with an equivalent rainfall of 20 mm/h. After this exposure to erosion, the sample - named Initialization 1 - had an observable change of roughness on the inner side, which is in the case of the present whirling arm the left side of the sample. This can be observed in Figure 8, a macro of the eroded sample, as a less shiny crescent covering about a third of the sample, starting from the inner side. As a reminder, the samples eroded using the WARER are disks of 30 mm diameter, held in the sample holder by a 1 mm circular lip, such that the exposed surface is a disk of 28 mm diameter.

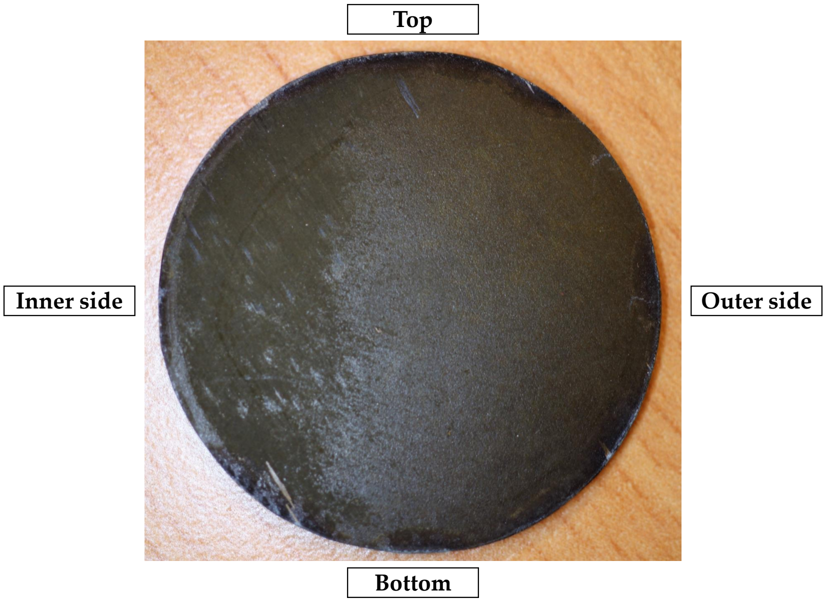

Figure 8: Visible erosion of the first reinforced epoxy composite sample (Initialization 1), after 3h exposure at standard conditions. Erosion can be observed as the less shiny zone on the left of the image, which represents about a third of the sample surface starting from the inner side.

By observing the sample using an *Olympus AX70* optical microscope, the change of roughness was confirmed. By comparing Figures 9a and 9b, which are bright field images of the inner and outer sides of the sample respectively, one can confirm that the inner part was eroded while the outer part was not. Indeed, Figure 9b shows regular pits on a mostly flat sample which appears light while Figure 9a shows a rougher surface, built by the adjacent water droplet impacts.

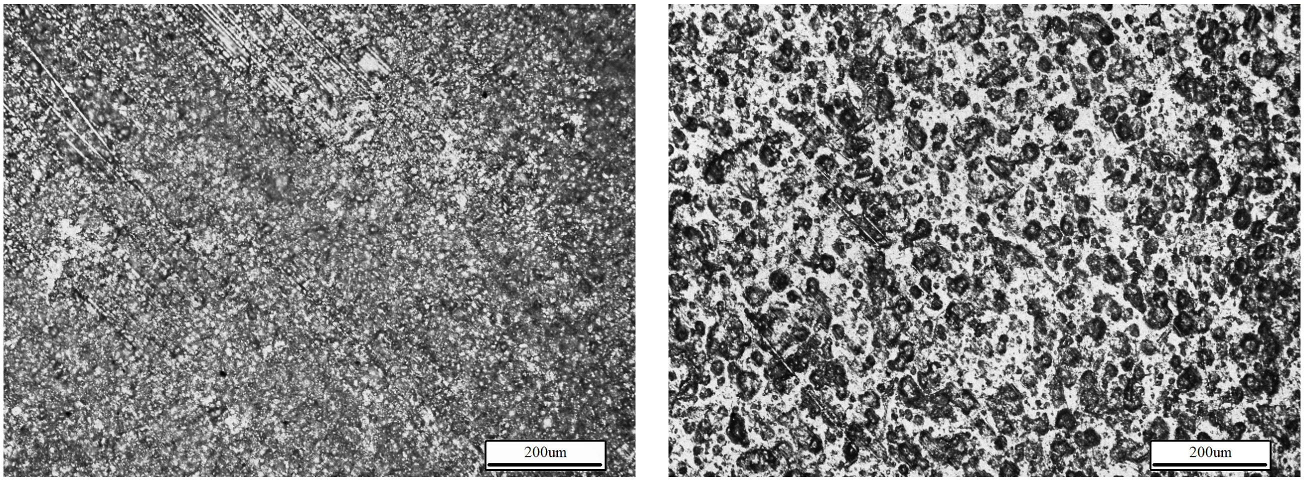

(a) Eroded, inner side

(b) Non eroded, outer side.

Figure 9: Comparison of the surface condition at (a) the inner side and (b) outer side of the first initialization sample (Initialization 1), made of carbon fiber reinforced epoxy resin, after 3 hours of accumulated exposure.

Based on these observations, the droplet dispensers were displaced outwards by 5 mm and this alignment was tested at standard conditions with another disk sample made of the same composite. As can be seen in Figure 10, the eroded, less shiny crescent this time covers around 80% of the surface of the sample, starting from the inner side.

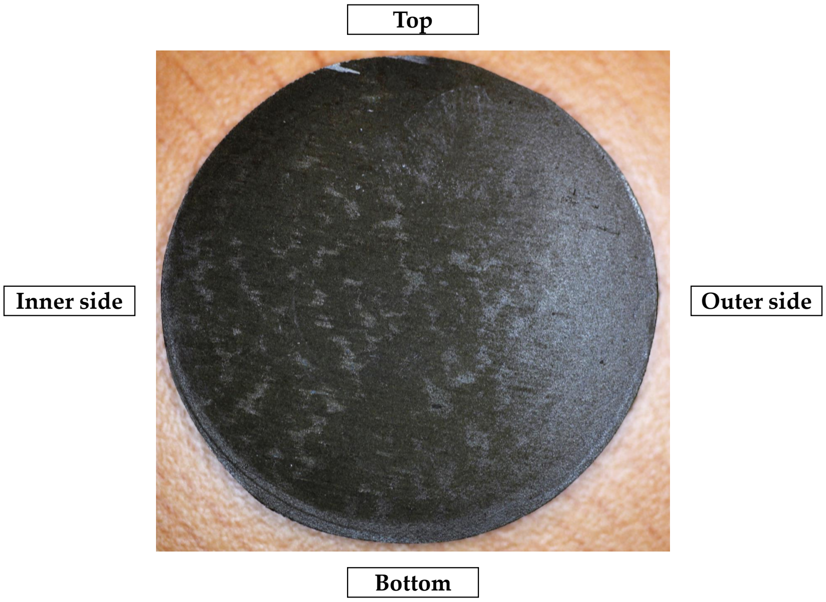

Figure 10: Visible erosion of the second fiber reinforced composite sample (Initialization 2), after 3h exposure. Erosion can be observed as the less shiny zone which represents about 80 % of the surface of the sample, starting from the inner side.

These two initialization settings confirmed the proper functioning of the whirling arm, ensuring that the droplet impacts happen mostly on the center of the sample. However, this initialization step highlights that the concentration of droplets is not uniform over the sample surface. This is due to the droplet dispensing system and the airflow pushing the artificial rainfall towards the outside of the circular path.

Unless otherwise mentioned, all the samples were tested for 18 hours in total under standard conditions in the WARER, systematically in batches of 3 hours. This corresponds to a total of 2.6 million impacts, spread inhomogeneously over the exposed surface of the sample, namely a disk of diameter 28 mm. The rainfall equivalent rate is 20 mm/h, with droplets of 2 mm diameter. Droplets of this size at impact speeds of 120 m/s each have a kinetic energy of 30.16 mJ.

### 3.1.2 PJET parameters

In order to have several points of comparison with the WARER results, 8 different erosion tests were performed on the samples. A first line of 4 erosion zones, named from A to D were tested at impact speeds of 225 m/s with increasing number of impacts, from 1 000 to 20 000. The second line of erosion zones, named from E to H, have the same number of impacts as the first one, but were tested at 180 m/s. Figure 11 illustrates the naming convention of the eight erosion zones. Table 3 summarizes the parameters used. Note that this reference of naming and of parameters for the PJET results is systematically used in this report, unless otherwise mentioned. Table 3 also compares the total energy received by the material, expressed as the product of the number of impacts and the kinetic energy of the droplets, as in equation (11). As mentioned by Rao et al. [44], only part of the kinetic energy of the droplets is absorbed by the material surface to cause erosion damage. They suggested that 90% of the energy is transformed in plastic work while the rest is dissipated in elastic wave energy.

$$\varepsilon_{tot} = n \cdot \frac{4}{3}\pi r_0^3 \rho_0 \frac{v_0^2}{2} \tag{11}$$

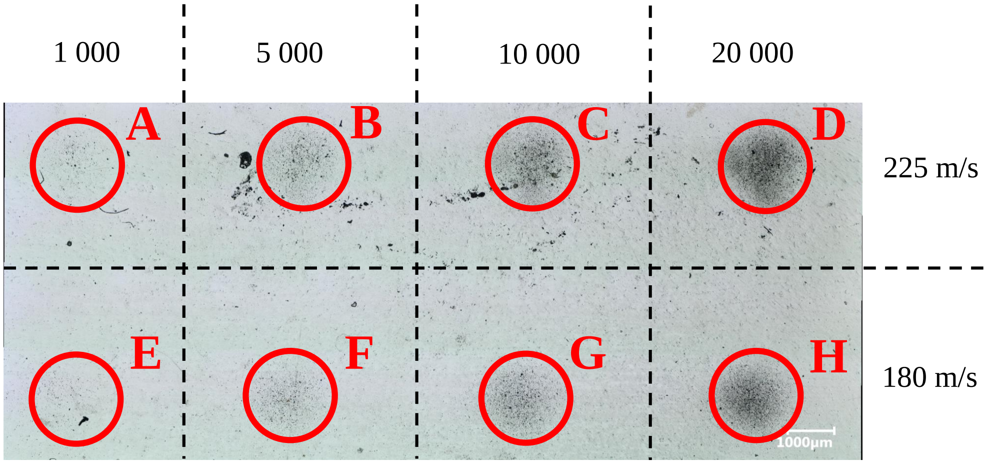

Figure 11: Macro image of the 8 erosion zones, named from A to H.

| Zone | $v_0$ [m/s] | $n$ [-] | $\varepsilon_{tot}$ [J] |
|---|---|---|---|
| A | 225 | 1 000 | 106 |
| B | 225 | 5 000 | 530 |
| C | 225 | 10 000 | 1 060 |
| D | 225 | 20 000 | 2 120 |
| E | 180 | 1 000 | 68 |
| F | 180 | 5 000 | 339 |
| G | 180 | 10 000 | 679 |
| H | 180 | 20 000 | 1 357 |

Table 3: Summary of the erosion conditions for each of the 8 zones, named A to H following the convention of Figure 11, tested using the PJET facilities. The impact speed $v_0$, number of impacts $n$ and total energy received $\varepsilon_{tot}$ are reported for each erosion zone. The temperature of the water used is 10°C and the impact frequency is 40 Hz, corresponding to a rainfall rate of 25 mm/h with droplets of 2 mm diameter. Note that the erosion zone is a disk of the order of 1.5 mm diameter.

## 3.2 Samples choice and preparation

Several materials with varying properties were tested in the present work, to observe different erosion mechanisms and behaviors. Note that no polymers were used, as literature proved they have poor resistance to erosion and limited lifetime. Indeed, that does not match with the objective of increasing the resistance and lifetime of the applications, namely leading edges in airplanes and wind turbines. Although from a weight and corrosion resistance point of view, polymers and composites globally dominate metals, their low hardness, low strength and low toughness are limiting factors for the long term resistance to erosion.

### 3.2.1 Nickel

The first category of materials tested is nickel. Two approaches were taken, namely electroplated nickel and bulk nickel. The choice for electroplated nickel samples was made for the very high hardness of the material, which can be 5 to 10 times higher than bulk nickel. Despite the high density of nickel, around 9 000 kg/m$^3$, the weight increase is limited as it consists of a coating, which can be applied on lighter materials such as the composites making the structure of wings or blades via an electroless deposition. When it comes to the bulk nickel, it was chosen to isolate the intrinsic bulk properties and remove the influence of the substrate.

The electroplated samples used a Watts bath prescribed by Karuppusamy et al. [45] to deposit a nickel coating on a copper disk substrate. During electroplating, pitting can appear due to substrate surface defects, attachment of air bubbles or oily residues on the substrate surface. To reduce the chances of pitting, the copper substrate was gently polished and was washed with a soapy solution to remove the possible surface grease. Then, the surface copper oxides were removed with $H_2SO_4$ to ensure nickel deposition on fresh, non-oxidized copper. In addition, the solution used, as prescribed by Karuppusamy et al., contained a wetting agent to reduce the surface tension and prevent the formation of bubbles on the substrate.

Three pairs of copper disks were sequentially electroplated using the same solution, for a duration from 120 to 135 minutes. Using a current density of 2 A/dm$^2$ for this duration resulted in an electroplated nickel coating of 60 µm thickness on average.

The second category of nickel samples were bulk annealed nickel disks, of grade 200. It consists of a commercially pure nickel sample at 99.2 %, with traces of carbon, copper, iron, manganese and silicon. Due to the annealing, the grain size is relatively large, of the order of 50 µm, according to Wasekar et al.

[46] Bulk nickel has low yield stress but good strain hardening and high ductility, an opposite behavior to the electroplated samples, which are harder but much more brittle.

Nickel is also known to have a good corrosion resistance, making it a durable candidate for aeronautic and wind power applications, provided that it sustains erosion. Due to its homogeneous nature, as opposed to the electroplated form, bulk nickel does not risk delamination and ensures to maintain corrosion resistance as erosion progresses. Indeed, it displays excellent resistance to intergranular corrosion.

### 3.2.2 Aluminum

The second category of materials tested is aluminum alloys, widely used in aviation for its high strength to weight ratio.

Currently, the reference in aeronautic leading edges is a Al2024 T3 clad sample, which is used for the calibration of the PJET at *Sonaca*. This sample is cladded with pure aluminum (1xxx series) to improve the corrosion and erosion resistance. The Al2024 alloy has a mass composition of 4.10 % Cu, 1.30 % Mg, 0.46 % Mn and traces of Fe, Cr, Si, Zn and Ti.

In order to identify individually which material parameters affect the WDE resistance, three different samples of Al7075 alloy were tested. This series was chosen because of its remarkable strength and because it undergoes broad research within *UCLouvain*. Note that the microstructure of the samples was not studied through metallography observations in the present work but rather through the extensive literature. The Al7075 series displays better strength and hardness than the reference Al2024 clad sample but poorer corrosion and impact resistance performances. The Al7075 series are alloyed with 5.5% in mass of Zn, 2.3% Mg, 1.4% Cu and less than 0.5% of Fe, Cr, Si, Mn and Ti. The three samples tested of this alloy have undergone different heat and mechanical treatments.

The first one is a reference Al7075 T4 alloy, which means it has undergone a solution heat treatment at 470 °C for 30 minutes, then was quenched and naturally aged. This is an intermediate state between the solution treatment and an actual heat treatment. It therefore does not lead to a thermodynamically stable state. The second sample is a Al7075 T6, in which case the homogenized solution was quenched then artificially aged at 120 °C for 24h, as reported by Lezaack et al. [47] and Li et al [48]. This heat treatment increases the tensile strength of the alloy up to over 500 MPa and is the hardest temper as shown by Yang et al. [49] However, it leads to a decrease of the strain-hardening capacity, which has an opposite, negative effect on the toughness. Finally, the last sample is a Al7075 which was friction stir processed then heat treated with a T6 procedure, hence called Al7075 FSP T6.

The friction stir process (FSP), derived from the friction stir welding technique, consists in locally modifying the microstructure through solid state mixing. Indeed, the material properties are modified by inducing localized plastic deformation with a rotating tool. As shown by F. Hannard [50], the friction stir process, via the solid mixing of the material, reduces the grain size, closes initial porosity and homogenizes the spatial distribution of particles and inclusions. The main advantage of this technique is that it increases the fracture strain by reducing the causes of ductility loss.

One should note that the main damage mechanism in these alloys is due to the stress build-up in inclusions, which are micron-sized $Fe-$ and $Si-$rich intermetallic particles. Indeed, intermetallic particles affect the ductility through the void nucleation, growth and coalescence, which can happen within the particle or at the interphase between the particle and the matrix. Therefore, the friction-stir processing allows to break those inclusions into much smaller, more spherical particles, resulting in greatly improved ductility. Another result of this FSP technique is that it leads to an isotropic fracture behavior due to the remodeling of the intermetallic particles into smaller, more spherical inclusions.

The 7xxx aluminum alloys series show the highest yield stress compared to other series due to the formation of precipitates, which harden the material greatly. As shown by Su et al. [51], the precipitation sequence of Al-Zn-Mg-Cu alloys, like the Al7075 series, consists in a supersaturated solid solution phase forming coherent Guinier-Preston zones which then form semi-coherent $\eta'$ phase. Finally, the $\eta'$ phase turns into an incoherent $\eta$ phase, with composition $MgZn_2$ which is the main phase responsible for precipitation hardening. The control of the size and distribution of the precipitates via the heat-treatment are key factors influencing the strength of the Al7075 series. Indeed, as shown by Aoba et al. [52], by combining work hardening such as forging or rolling to an age-hardening heat treatment, the material is greatly strengthened through precipitation and dislocation hardening. In addition, as confirmed by Garcia do Vale et al. [53], upon rolling of the Al7075 sheet prior to the sample machining, the $MgZn_2$ and $CuMgAl$ precipitates align with the rolling direction, which causes oriented strengthening.

It was shown by Joshi et al. [54] that the heat treatment undergone by the different Al7075 samples determine the solute concentration and distribution at the grain boundaries. Indeed, the number and size of precipitates are dictated by the heat treatment, thereby influencing the yield strength and plastic properties of the samples by blocking the motion of dislocations. The heat treatment also slightly changes the composition of the precipitates at the grain boundaries, despite the same solution heat treatment. Indeed, the relative amounts of Mg, Zn, Cu, Fe and Ni in the precipitates change with the heat treatment. Because of this migration during aging, dominated by Mg and Zn, a high corrosion potential is observed at the grain boundaries.

Finally, a Al2024 sample which was chromium anodized then covered with an epoxy coating was also tested in the early stages of experiments. The anodizing step was used to provide a more rugged surface, allowing a better adhesion of the epoxy coating.

### 3.2.3 Titanium

The last category of samples tested was Ti6Al4V, a material chosen for its high strength-to-weight ratio and its good corrosion resistance. Titanium, alongside composites and aluminum, is widely used in new generation aircraft because of its high strength, up to 1 000 MPa, and low density, around 4 500 kg/m$^3$.

Ti6Al4V is an alloy comprising two phases: an $\alpha$ phase with an hexagonal close packed (HCP) crystallographic structure and a $\beta$ phase of body centered cubic (BCC) structure. The alloy takes the structure of $\alpha + \beta$ lamellae incorporated in the $\beta$ grains. The size of the grains is comprised between 10 and 30 µm in the as-received material. [55]

It was shown by Dina Ma [23] that the main erosion mechanism is the initiation of cracks between the $\alpha$ and $\beta$ phases. In addition, she demonstrated that applying a surface plastic treatment inducing compressive surface stresses, such as burnishing or shot peening, does not improve significantly the erosion rate. Indeed, the treated materials showed comparable mass loss rate. However, surface compressive stresses modify the morphology of the pits generated as they were wider and shallower than in non-treated Ti6Al4V. In other words, the surface developed less abrupt topography thanks to the treatment.

### 3.2.4 Samples surface preparation

After machining, the samples were polished. Indeed, the initial surface roughness seems to have a significant influence on the duration of the incubation period and the erosion rate in general. As shown by Kirols et al. [18], the presence of asperities and irregularities accelerates erosion. In order to start all the experiments on the same basis, all the samples were mirror polished before being submitted to the erosion tests.

The polishing procedure consisted in first 4 steps of sand paper polishing with the following grits: 320, 500, 800 and 1200. After these steps, the samples were further polished with cloths of 3 different grain sizes: 9 µm, 3 µm and 1 µm. The surface roughness upon polishing is of the order of $R_a = 40$ nm.

Note that this procedure was not performed on the electroplated nickel samples. Indeed, the electroplated nickel samples already had a shiny, mirror aspect and since the coating was rather thin, a polishing step risked unveiling the copper substrate.

## 3.3 Techniques of analysis

In order to compare the results of the different erosion tests, the following properties of the samples were measured: weight, hardness, Young's modulus. In addition, the topography and roughness of the samples were observed using different microscopy techniques as well as laser interferometry. The different techniques of analysis are presented in this section, illustrated with two preliminary samples.

### 3.3.1 Mechanical properties tests

Prior to each experiment, the samples were **weighed** individually. Note that the samples submitted to the PJET did not allow a measure of the weight loss. Indeed, the impacts are concentrated on a very restricted area, which would lead to insignificant measurements. In addition, as all the tests were performed on a single panel of the samples, the variation of mass cannot be associated with each erosion zone.

The hardness of the samples was measured using a **micro-indentation** Vickers test. The machine used is an *EMCO DuraScan G5* automated micro-indenter. A total of 10 indents were made across the surface of each sample using a 300 g load with a Vickers indent, for a standard duration of 10 s. The value of the **Vickers hardness** (HV0.3) was averaged between the 10 measurements.

In addition, **nano-indentation** was performed with a Berkovich tip, using an *Agilent G200* nano-indenter in continuous stiffness measurement mode. Thanks to the instrumented indentation, the evolution of the **Young's modulus** and the **hardness** throughout the indentation were obtained, for 16 different indents on each sample. The parameters are a surface approach velocity of 10 nm/s, a strain rate of 0.05 $s^{-1}$, a harmonic displacement of 2 nm at a frequency of 45 Hz and a penetration depth down to 2 µm. Note that the software uses an Oliver-Pharr model to compute the projected area as a function of the depth of penetration of the indent. This model considers a sink-in phenomenon in the computation of the projected area. However, since all five materials tested have the opposite tendency, namely to create pile-up, another model was used on the data to compute Young's modulus and hardness: Loubet's model, as detailed by Bec et al. [56]

The nano-indenter measures the stiffness $S$, the load $P$ and the depth of penetration $h$ in real time. Loubet's model estimates the corrected depth of the indent $h_c$, considering the pile-up phenomenon, thanks to a parameter $\alpha = 1.2$ as in equation (12).

$$h_c = \alpha \left( h - \frac{P}{S} \right) \tag{12}$$

From this corrected penetration depth, the projected area $A$ can be estimated as in equation (13), based on the geometry of the Berkovich tip, as mentioned by Dao et al. [57]

$$A = 24.56\, h_c^2 \tag{13}$$

From this projected area, the hardness can be directly computed as the ratio of the load divided by the area, $H = \frac{P}{A}$. Finally, to compute Young's modulus $E$, a first step is to compute the reduced modulus $E_r$ using Sneddon's relation as in equation (14). Young's modulus $E$ can then be obtained as in equation (15) where the parameters $\nu_i = 0.07$ and $E_i = 1141$ GPa are respectively Poisson's ratio and Young's modulus of the indenter.

$$E_r = \frac{\sqrt{\pi}}{2} \frac{S}{\sqrt{A}} \tag{14}$$

$$E = \frac{1 - \nu^2}{\left( \frac{1}{E_r} - \frac{1-\nu_i^2}{E_i} \right)} \tag{15}$$

Besides these indentation tests, a tensile test was performed on the Ti6Al4V sample, in both longitudinal and transverse orientations compared to the rolling direction. The dog-bone traction sample dimensions followed the ASTM E8 reference. The test was performed at a pulling speed of 1 mm/s and the yield strength, measured at 0.2 % plastic strain, was obtained by drawing a shifted parallel to the stress-strain curve. Note that the toe region was not corrected.

### 3.3.2 Observation techniques

The surface topography of each sample was recorded, as well as its evolution. Before testing, the surface condition of each sample was observed using an *Olympus AX70* **optical microscope** to ensure the lack of significant, abnormal scratches and defects.

Then, to observe the evolution of the surface profile and the damage mechanisms, several other methods were used. The samples were observed with a **digital microscope**, namely the *Keyence VHX 6000 950F*. Images were also taken using *Zeiss FEG SEM Ultra55* **scanning electron microscope**, which allows higher resolution enabling to observe the damage mechanisms undergone by the samples at lower scale.

Let's compare a few images to illustrate the versatility of each observation technique. The reference aluminum alloy used for calibration at *Sonaca*, the Al2024 T3 clad, was eroded with the PJET and serves as example for the elaboration of the analysis strategy. This material was exposed with the PJET to 10 erosion zones with increasing number of impacts, each at impact speed of 180 m/s. Each zone was named from `I` to `X`, as illustrated in Figure 12. The number of impacts corresponding to each zone is given in Table 4. Note that this does not correspond to the erosion pattern used on the other PJET samples, named from A to H, since the Al2024 T3 clad sample only serves as illustration for the observation techniques.

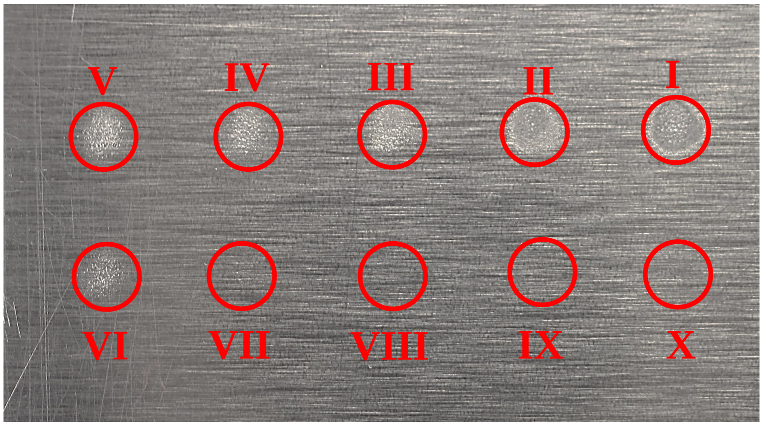

Figure 12: Macro image of the reference Al2024 T3 clad sample eroded using the PJET with the erosion zones named from `I` to `X`.

| **Zone** | **V** | **IV** | **III** | **II** | **I** |
|---|---|---|---|---|---|
| $n$ | 1 000 | 2 000 | 3 000 | 6 000 | 10 000 |
| **Zone** | **VI** | **VII** | **VIII** | **IX** | **X** |
| $n$ | 500 | 250 | 100 | 50 | 20 |

Table 4: Number of impacts $n$ using the PJET for each of the 10 zones of erosion testing, named from `I` to `X`.

This sample was thoroughly used to compare the observation techniques and to develop the analysis strategy. Indeed, this sample showed for example that using dark field optical microscopy better highlights the surface condition of highly eroded zones (e.g. zone `I`) while using bright field microscopy is more appropriate for less eroded zones (e.g. zone `V`). This comparison is illustrated in Figure 13.

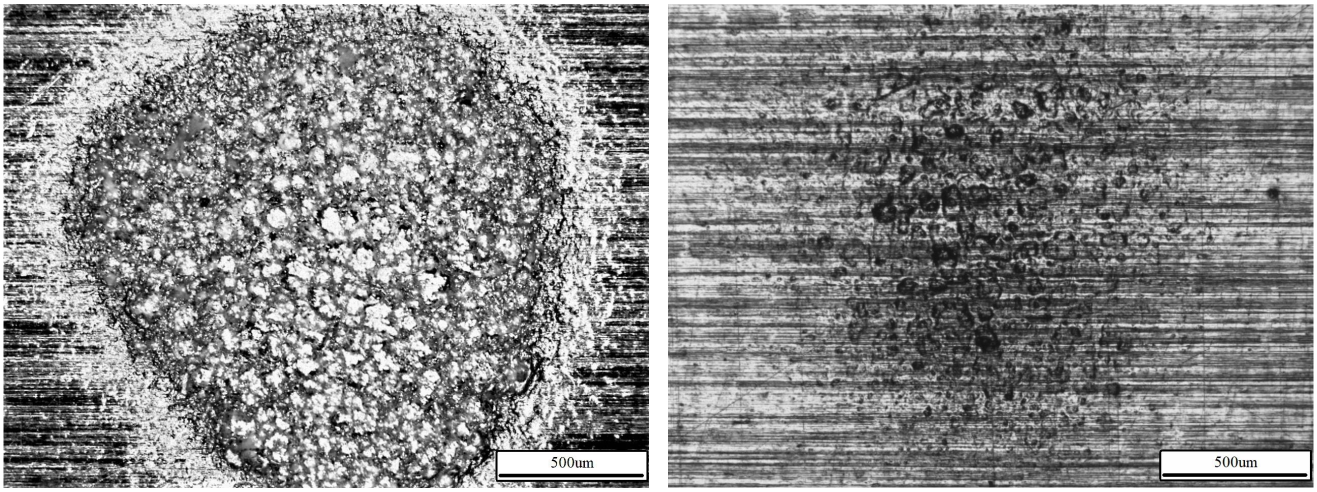

(a) Zone `I` - Dark field

(b) Zone `V` - Bright field

Figure 13: Comparison of optical microscopy techniques depending on erosion level. (a) Dark field optical microscopy is more relevant for heavily eroded samples. (b) Bright field microscopy highlights surface condition with better contrast for less eroded samples.

This sample also highlighted that scanning electron microscopy techniques are more relevant for highly eroded zones than poorly eroded ones. Indeed, despite working with different electron detectors, different high voltages or opening the aperture wider, the contrast remained very low for samples with lower levels of erosion. This limitation is illustrated in Figure 14, which compares SEM images in the best conditions for zones `I` and `V`.

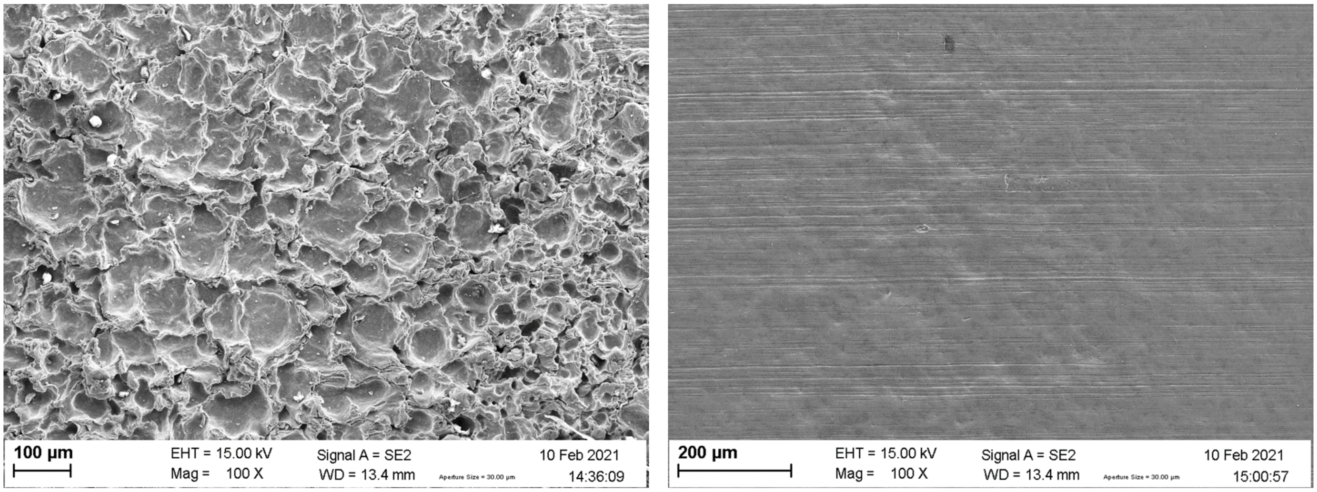

(a) Zone `I` (b) Zone `V`

Figure 14: Scanning electron microscopy highlights with excellent resolution and depth of field the surface condition of heavily eroded samples (a) while low erosion levels are smoothed out (b).

Finally, this calibration sample revealed that digital microscopy seemed to be the best suited, easiest and fastest technique to assess surface condition. Indeed, thanks to the large depth of field, the surface relief is highlighted with excellent resolution. This observation technique is illustrated in Figure 15, again comparing images of zones `I` and `V` of the reference sample.

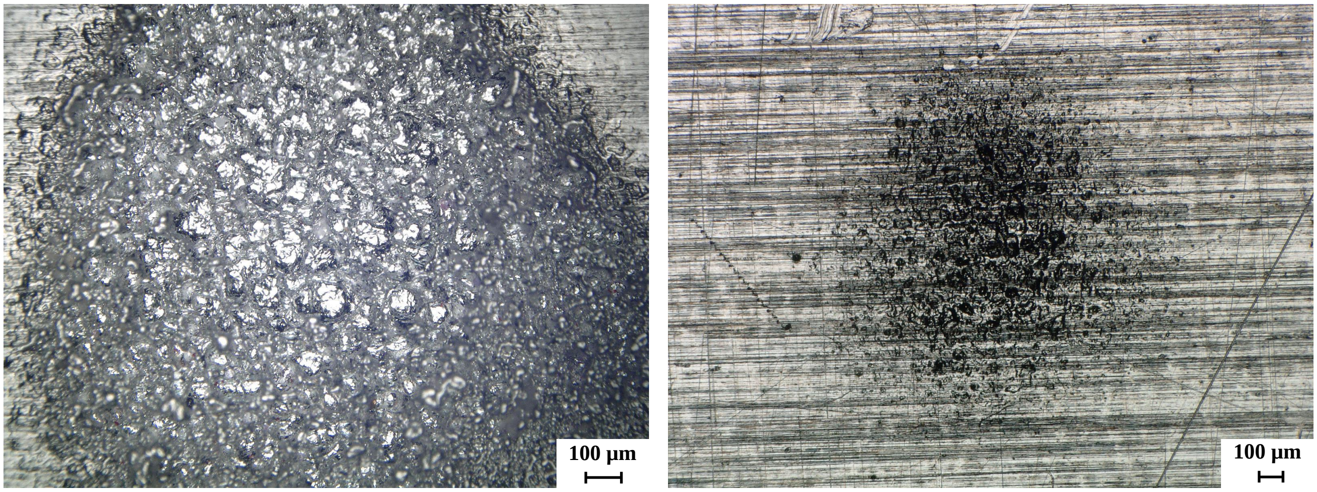

(a) Zone `I` (b) Zone `V`

Figure 15: Digital microscopy seems to be the most versatile technique for a broad range of erosion levels, from (a) advanced erosion to (b) low erosion levels, due to high resolution and large depth of field.

With this sample, the observation techniques were compared and it was shown that the digital microscopy technique is the most appropriate for its versatility, flexibility and ease of use.

### 3.3.3 Roughness measurement techniques

Besides its high contrast images, **digital microscopy** can also be used to measure the surface profile and roughness. Figure 16 illustrates the surface profile of zone `V` of the Al2024 T3 clad sample along the red line drawn. This shows a rather accurate profile, which allows to compute roughness parameters such as $R_a$ or $R_z$ as well as the depth, width and spacing between the pits.

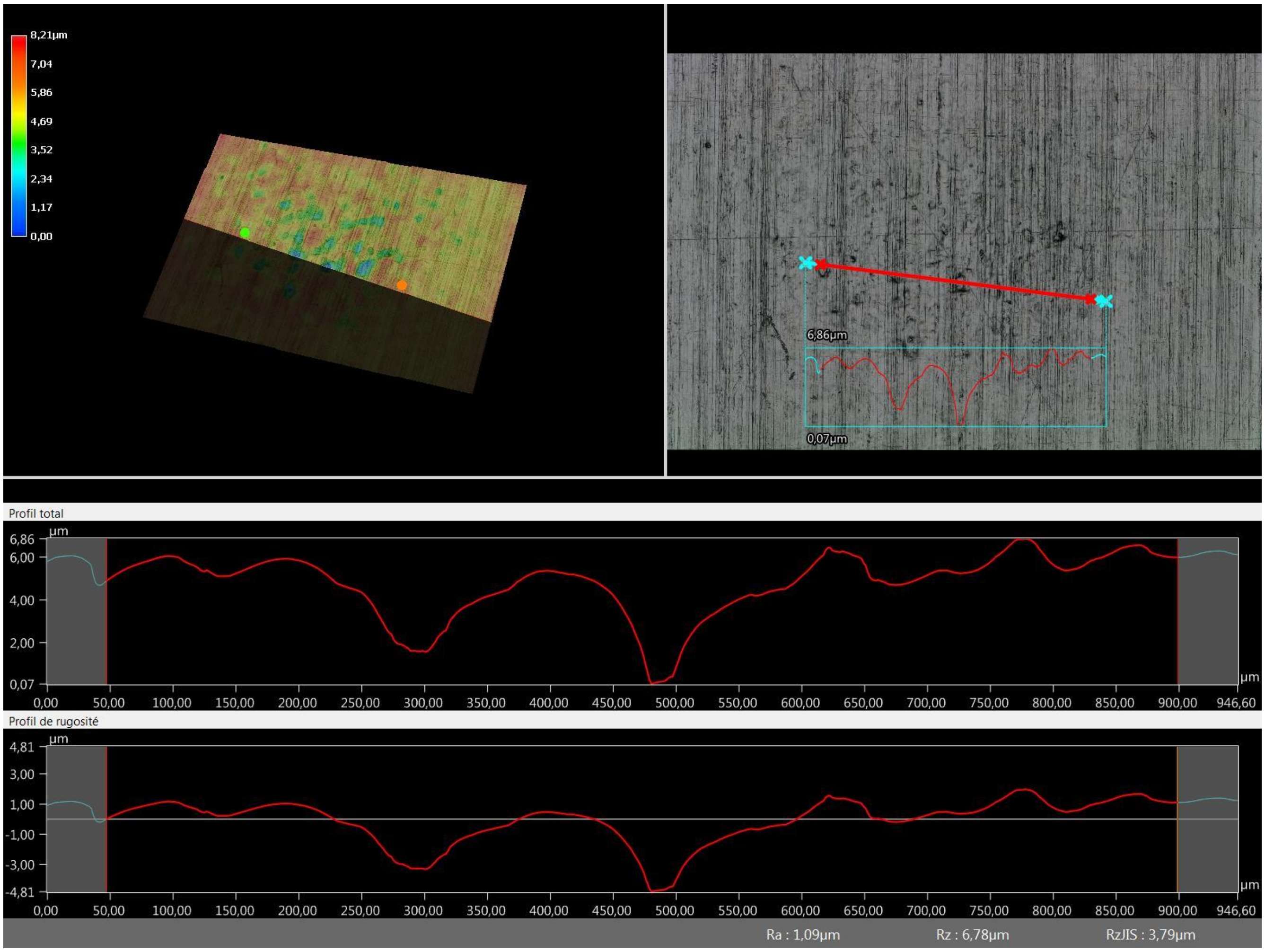

Figure 16: 3D surface profile of zone `V` of the calibration sample obtained with digital microscopy. Along the profile of the red line, the $R_a$ and $R_z$ values measured are 1.09 µm and 6.78 µm respectively. Along this profile, two pits of depth 3 and 5 µm can be measured, as well as their width respectively of 100 and 80 µm.

This seems to be a very useful tool for such samples, with intermediate levels of erosion and $R_a$ values around 1 µm. Indeed, the profile is closely followed and it clearly shows the pits of depth around 5 µm created by the WDE. However, the digital microscope used, namely *Keyence VHX 6000 950F*, has limitations. Indeed, the software requires to manually determine the uppermost and lowermost points of the surface in order to scan in that vertical range. Within that range, only 200 images can be taken, which greatly limits the resolution of profiles that can be observed. This limitation becomes critical for non-planar samples or for samples with very deep valleys and peaks, for which the profile is mostly influenced by the long wavelength surface fluctuation rather than the actual surface profile.

To counter this problem, **laser interferometry** can be used to obtain an accurate measure of the roughness of the samples. In the present work, a *Polytec Micro System Analyzer* was used. This apparatus scans an area of 850 µm by 650 µm and takes 88 profiles from which roughness parameters such as $R_a$, $R_z$, $R_{ku}$ or $R_{sk}$ are computed. The vertical profile is limited to 220 µm, which corresponds to $R_a$ around 35 to 40 µm, far above the surface damage occurring in the experimental conditions of the present work. Laser interferometry is an easy, contact-less technique for precise roughness and profiles measurements. Figure 17 shows the surface profile of the same erosion zone as in Figure 16, namely zone `V` of the Al2024 T3 clad sample, using laser interferometry.

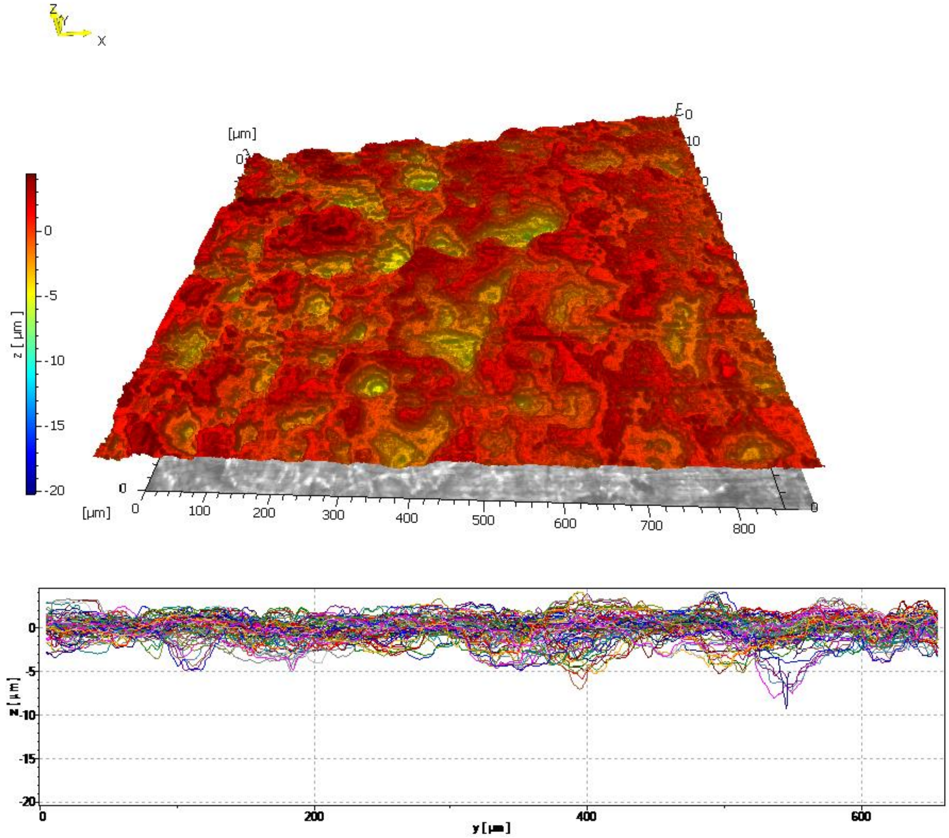

Figure 17: 3D surface profile of zone `V` of the calibration sample obtained with laser interferometry. The average $R_a$ and $R_z$ values measured over the entire surface are 0.89 µm and 3.66 µm respectively.

Figure 17 shows that the laser interferometry technique brings better resolution in terms of profile features than the digital microscope. Indeed, the width and depth of the pits can be measured with better accuracy. In addition, the roughness parameters such as $R_a$, $R_z$, $R_{sk}$ or $R_{ku}$ are automatically computed on 88 parallel profiles along the y-axis, then averaged. However, this technique also has limitation, namely interference fringes, which appear for slightly sloping samples with very smooth, shallow features. Still, as it offers better lateral resolution than the digital microscope, laser interferometry was chosen for a more relevant comparison of the roughness of different samples of the present work. The digital microscopy technique was therefore not used for the profile measurement but only for imaging due to the high contrast and depth of field.

Another preliminary sample can be used to illustrate the capability of the laser interferometer, namely the chromium anodized Al2024 covered with an epoxy coating. This sample was first exposed to erosion in the WARER for 6 hours at standard conditions, then for an additional 6 hours. The results are illustrated by macro pictures in Figure 18.

(a) 6 hours

(b) 12 hours

Figure 18: Macro images of the chromium anodized Al2024 with an epoxy coating sample, exposed for (a) 6 hours and (b) 12 hours to erosion at standard conditions in the WARER.

As can be seen in those pictures, the erosion damage is unsurprisingly more pronounced after 12 hours than after 6 hours of exposure. One should also note the shape of the erosion area, which roughly follows the numerical simulations performed by S. Masson. [58] Indeed, the path of the falling droplets in the turbulent regime created by the rotating arm can be retrieved based on the shape of the impacted region. As can be seen in Figure 18, most droplets are impacted on the top left of the sample. This confirms that the WARER was correctly configured.

This sample was also used to evaluate the laser interferometry as a technique to compare surface roughness. The two zones highlighted (1 and 2) in Figure 18b correspond to spots where interferometry measurements were made. Figure 19 shows the laser interferometry profiles measured for both zones 1 and 2.

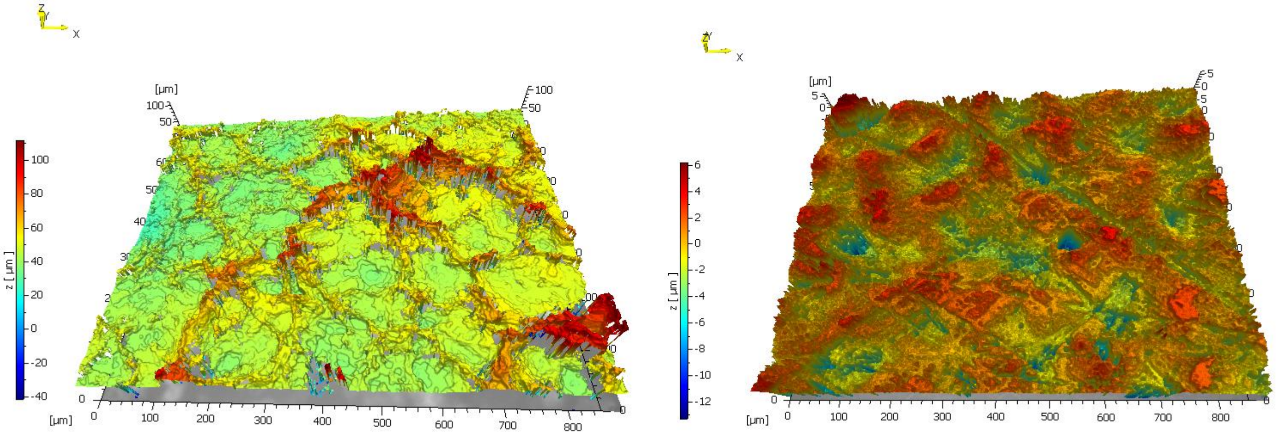

(a) Zone 1

(b) Zone 2

Figure 19: Laser interferometry profiles captured for (a) zone 1 and (b) zone 2 of the chromium anodized Al2024 sample with epoxy coating.

Zone 1 corresponds to a zone which was severely eroded and has a measured arithmetic mean roughness of $R_a = 6.5$ µm. Zone 2, which corresponds to the non-eroded epoxy coating, has a roughness of $R_a = 1$ µm. This relatively high roughness for a coating is due to scratches suffered during the transport and storage of the sample, which can be observed in Figure 19b.

### 3.3.4 Comparison of roughness parameters

Thanks to laser interferometry, profiles can be measured on the surfaces, from which roughness values such as $R_a$, $R_z$, $R_{sk}$ or $R_{ku}$ can be computed. However, these values are not all suited for erosion level comparison, as shown by U. Ghantasala. [59]

From a surface line profile, the most commonly computed value is $R_a$, which is the arithmetic mean roughness, computed as in equation (16), where $y(x)$ is a line profile height.

$$R_a = \frac{1}{L}\int_0^L |y(x)|\, dx \tag{16}$$

In the measurements made with laser interferometry, the length $L$, called cut-off wavelength, is fixed to 0.6 mm, with five segments within this length. The $R_a$ value is not suited for roughness comparison in the case of erosion behavior as it hides all the features of the profile. Indeed, as can be seen in Figure 20, very different profiles can lead to a similar $R_a$ value. Whether peaks or valleys are present, their number and distribution are not reflected in the $R_a$ value.

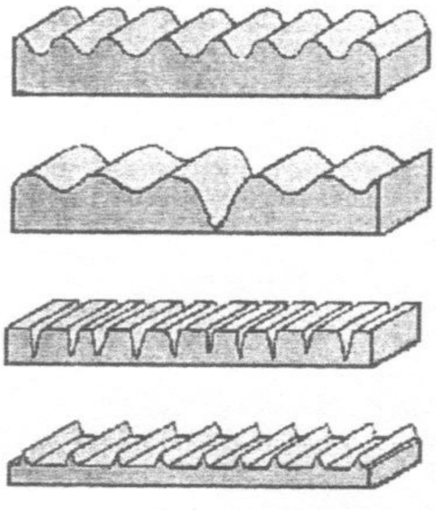

Figure 20: Four different surface profiles with similar $R_a$. Image from Matuszewski et al. [60]

A better parameter is the $R_z$, defined as the average of the maximum peak to valley vertical distance to each of the assessed segments. This gives a better idea of the dimensions of the defects but does not tell whether there is a majority of valleys or peaks.

For that, the most appropriate parameter is the $R_{sk}$, which measures the skewness of the height distribution. This qualifies the asymmetry of the height distribution around the mean line. Negative values of $R_{sk}$ indicate a surface with deeper valleys while positive values of $R_{sk}$ indicate higher peaks. The $R_{sk}$ is defined as in equation (17). Note that in equation (17), the parameter $R_q$ is the root mean square height, the standard deviation of the profile, defined as $R_q = \sqrt{\frac{1}{L}\int_0^L y^2(x)\, dx}$.

$$R_{sk} = \frac{1}{R_q^3}\left[\frac{1}{L}\int_0^L y^3(x)\,dx\right] \tag{17}$$

Figure 21 compares two profiles with positive and negative $R_{sk}$. It clearly shows that negative profile skewness corresponds to a surface with a majority of deep cracks while a positive skewness corresponds to a majority of high peaks.

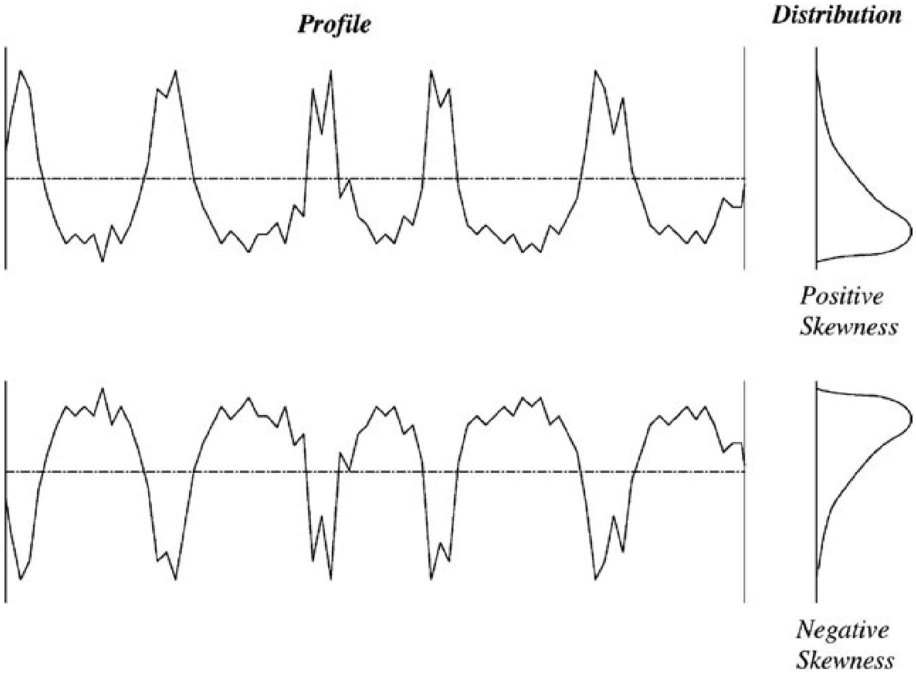

Figure 21: Two profiles with different skewness. The top profile has a positive $R_{sk}$, meaning that it is dominated by high peaks while the bottom profile has a negative $R_{sk}$, corresponding to a dominance of cracks. Image from Gadelmawla et al. [61]

A final parameter that can bring useful information for the assessment and comparison of the samples roughness is the $R_{ku}$, standing for kurtosis. The kurtosis qualifies the sharpness of the profile features and is defined as in equation (18). A critical value of $R_{ku}$ is 3 as it qualifies a Gaussian distribution. Values of $R_{ku}$ lower than 3 indicate broader peaks or valleys while values above 3 indicate narrower, sharper features.

$$R_{ku} = \frac{1}{R_q^4}\left[\frac{1}{L}\int_0^L y^4(x)\,dx\right] \tag{18}$$

Figure 22 shows two profiles with different values of $R_{ku}$, to illustrate that this parameter reflects the sharpness of the profile.

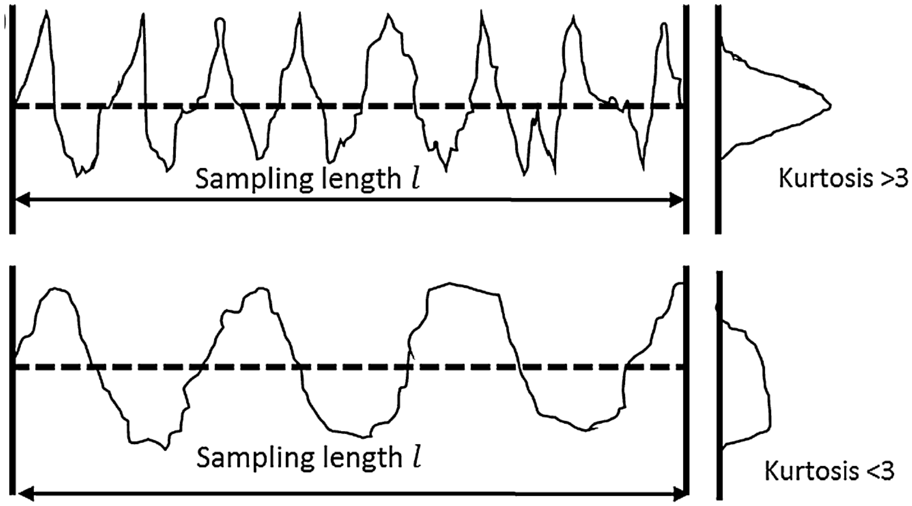

Figure 22: Two profiles with different kurtosis. The top profile, with a value of $R_{ku} > 3$, has sharp, narrow peaks and cracks while the bottom profile, with a value of $R_{ku} < 3$, shows a much smoother evolution, with wider features. Image from Taro et al. [62]

Note that many other parameters can be computed if the full surface profile is known, as extensively listed by Gadelmawla et al. [61] However, the laser interferometer used in the present work did not give direct access to the entire surface profile but only to the above mentioned computed parameters.

# 4 Results and analysis

With the erosion parameters chosen and the techniques of analysis described in the methodology section, let's now look at the results of the experiments and their analysis. Both Al2024 T3 clad and the chromium anodized Al2024 with an epoxy coating samples were used to determine the best set of analysis techniques and will not be further studied. Instead, erosion tests using both WARER and PJET are performed on the five samples previously presented, namely three Al7075, the Ni bulk and the Ti6Al4V. Only homogeneous materials were compared in this section as the objective is to isolate material properties influencing the resistance to WDE. Therefore, the electroplated Ni samples will be covered separately in a subsequent section.

## 4.1 Materials test results

### 4.1.1 Material properties

The nano-indentation tests were performed on all five samples, giving the evolution of the hardness and Young's modulus as a function of the indenter penetration depth. All five samples had similar behavior, showing pile-up and curves of similar evolution reaching however different values. Figure 23 shows the load-penetration depth curve of an indent of the Al7075 T4 sample, which is representative for all the other samples. Figures 24 and 25 show the evolution of Young's modulus and the hardness of the Al7075 T4 sample as a function of the penetration depth. Note that an average curve of the load, Young's modulus and the hardness of each of the five samples can be found in the Annex 6.1.

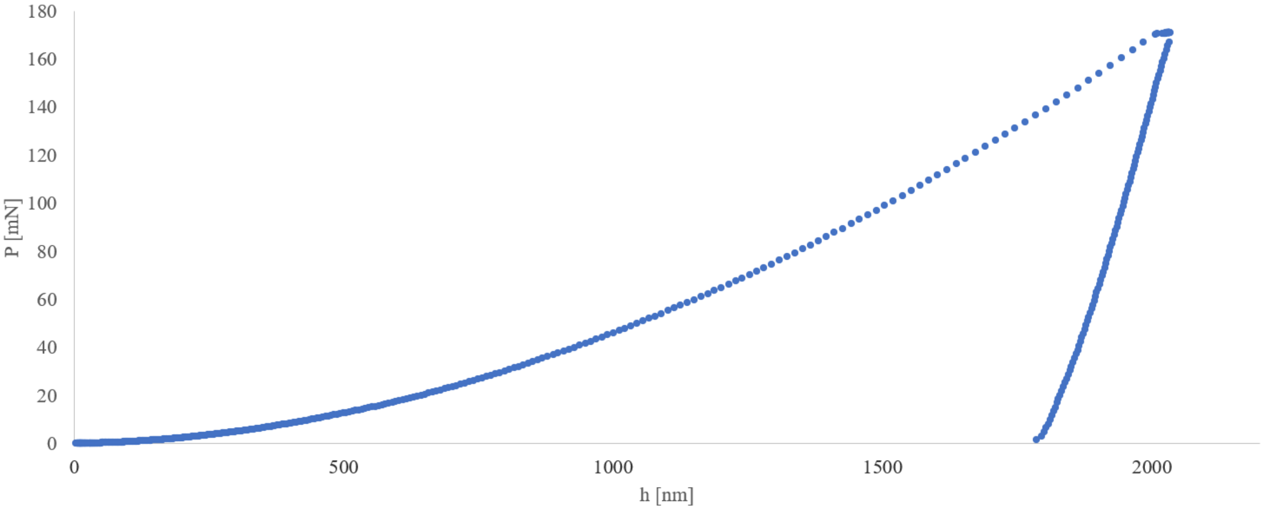

Figure 23: Load $P$ as a function of the penetration depth $h$ for sample Al7075 T4.

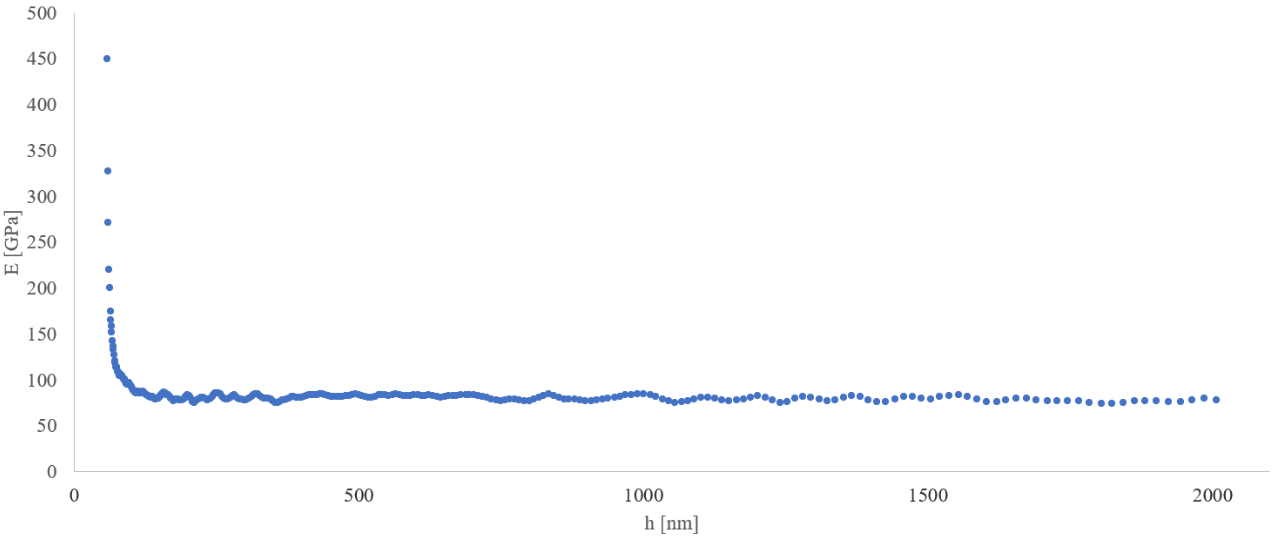

Figure 24: Evolution of Young's modulus $E$ of the Al7075 T4 sample as a function of the penetration depth $h$.

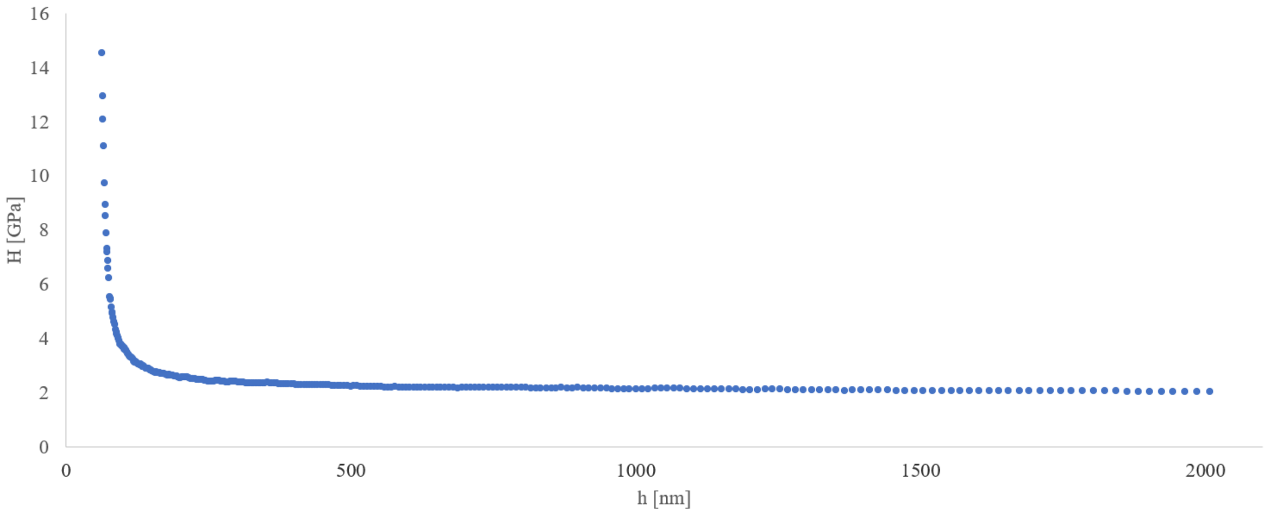

Figure 25: Evolution of the hardness $H$ of the Al7075 T4 sample as a function of the penetration depth $h$.

Figure 23 shows a typical load-depth curve for ductile materials, with no pressure induced change, cracks or creep. Figures 24 and 25 show that the measures of Young's modulus and the hardness stabilize with the indentation depth. As can be seen in the Annex 6.1, this stabilization was not as marked in the Ni bulk sample, which showed a continuous slight decrease of both measures with the depth. This means the Ni bulk sample is more sensitive to the indentation size effect, which can be explained by the fact that it is a rather soft bulk material. Due to the high strain gradient at low penetration depths, geometrically necessary dislocations are nucleated and increase the measured hardness. In addition, the Ni bulk sample showed a more ductile behavior, with very limited spring back upon unloading compared to the other four samples, as can be seen in Figure 66a in Annex 6.1.

From these curves obtained through nano-indentation, the hardness and Young's modulus of the samples can be evaluated as the mean value between 1 µm and 2 µm depth. This average was performed for all the samples, except for the Ni bulk. For this sample, which is severely influenced by the indentation size effect, the average between 1.9 µm and 2 µm depths was taken.

In addition, the Vickers hardness of the samples, in HV as an average of 10 indents, was obtained using the micro-indentation procedure mentioned earlier. Note that multiplying the Vickers micro-hardness value in HV by a factor 9.807 transforms the kgf/mm$^2$ unit into MPa, which is the unit of the nano-indentation measured hardness. The results of both nano- and micro-indentation are summarized in Table 5.

| Material | Al7075 T4 | Al7075 T6 | Al7075 FSP T6 | Ti6Al4V | Ni bulk |
|---|---|---|---|---|---|
| Nano-hardness [MPa] | 1 240 (32) | 1 380 (50) | 1 390 (22) | 2 360 (101) | 1 090 (20) |
| Young's modulus [GPa] | 72 (0.71) | 75 (1.2) | 69 (0.61) | 102 (1.5) | 172 (7.3) |
| Micro-hardness [MPa] | 1 510 (14) | 1 800 (12) | 1 850 (15) | 3 170 (73) | 1 000 (46) |

Table 5: Measures of hardness and Young's modulus of the five samples, using nano- and micro-indentation. The standard deviation of each measure is between brackets.

As can be seen in Table 5, the results from the micro- and nano-hardness come in agreement, as they both classify the materials in the same order of increasing hardness, namely Ni bulk, Al7075 T4, Al7075 T6, Al7075 FSP T6 and Ti6Al4V. However, what is more surprising is that the hardness measured by the nano-indenter is significantly lower than the one measured with the micro-indenter. This is contradicting the indentation size effect, which predicts that the hardness of the material is higher at low penetration depth due to the geometrically necessary dislocations nucleated. One possible explanation to this slight shift between both measurements is the Loubet model used, for which the parameters of the actual contact surface or effective stiffness may not be optimal. Another possible explanation is the misprediction of the tip defect caused by wear.

The Vickers hardness can be related to the ultimate tensile strength of the materials once expressed in MPa by dividing the value by a factor 3. This gives the following ultimate tensile strengths: $\sigma_{u,T4} = 500$ MPa, $\sigma_{u,T6} = 600$ MPa, $\sigma_{u,FSP} = 620$ MPa, $\sigma_{u,Ti} = 1050$ MPa and $\sigma_{u,Ni} = 330$ MPa. This corresponds correctly with what can be found in the literature. [48] [55] [63]

One should note that Young's moduli measured for the aluminum alloys are rather surprising compared to the literature. First of all, all three Al7075 alloys should show a similar Young's modulus as it is not influenced by the heat treatment, nor by the friction stir processing. According to the literature, Young's modulus should be around 72 GPa, as measured for the Al7075 T4 sample.

In addition, Young's modulus evaluated for the Ti6Al4V sample seems underestimated. Indeed, in the literature, common values are around 110 GPa, slightly higher than the measured modulus using nano-indentation. To confirm this value, two tension tests were performed on the Ti6Al4V plate. The tests were performed parallel to the rolling direction, called longitudinal, and perpendicular to this direction, called transverse. The stress-strain curve can be found in Figure 68, in Annex 6.2. These traction tests gave a Young's modulus of 114 GPa and 126 GPa in the transverse and longitudinal directions respectively. The yield stress is $\sigma_{y,0.002} = 950$ MPa for both directions while the ultimate tensile strengths are $\sigma_u = 1017$ MPa and $\sigma_u = 1050$ MPa for the transverse and longitudinal directions respectively. As for the aluminum alloys, the measure of the strength through the nano-indentation matches these results but Young's modulus is significantly offset.

It is interesting to note that since the samples seem to be anisotropic due to the direction of rolling, the water droplet erosion may probably also induce a non isotropic response. This will be discussed in the following section, covering the erosion mechanisms.

Besides the mechanical properties, one should also look at the microstructure of the samples. For that purpose, scanning electron microscopy is of great use, as it can show the inclusions distribution. In the case of the present work, the analysis of the influence of the FSP technique on the size, shape and spatial spreading of the inclusions in the Al7075 FSP T6 sample is the most relevant. Figure 26 compares SEM images of the Al7075 FSP T6 sample inside and outside the FSPed zone. As highlighted with the red bars in Figure 26a, the zone that has been rolled but not FSPed shows orientation of the intermetallic particles as beads aligned with the rolling direction. This is equivalent to the Al7075 T6 sample, which has not been friction stir processed. On the other hand, as shown in Figure 26b, the zone that has been friction stir processed has much smaller inclusions, spread out in clouds. One should note that by increasing the number of passes of the FSP head, these intermetallic particles would have been even smaller and more homogeneously spread, as shown by Hannard et al. [64]

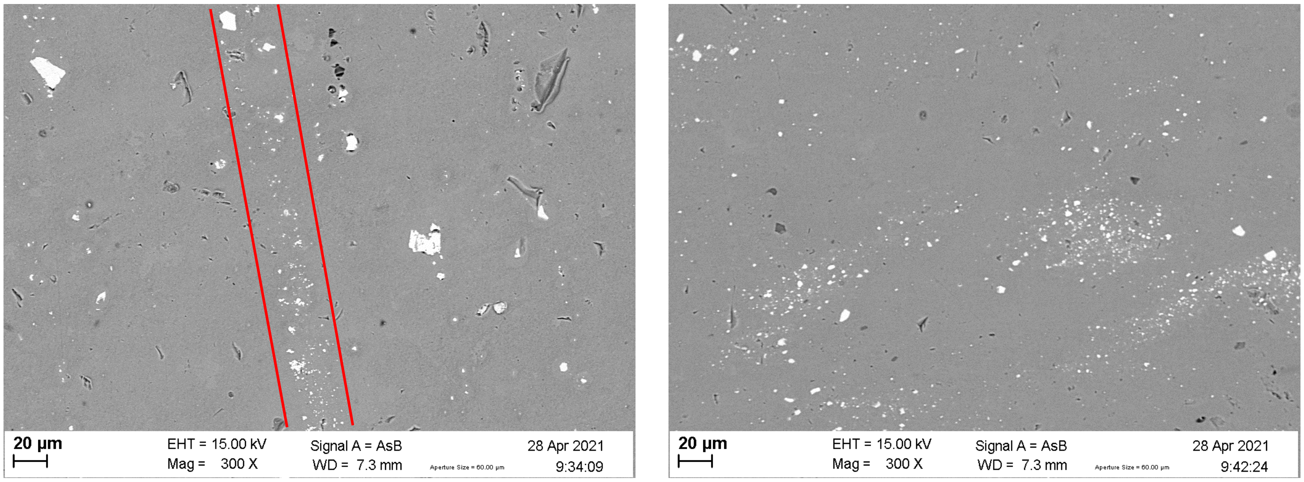

(a) Al7075 FSP T6 - Outside FSPed zone

(b) Al7075 FSP T6 - Inside FSPed zone

Figure 26: Al7075 FSP T6 sample pictured (a) outside and (b) inside the FSPed zone. Note that the microstructure illustrated in (a) is equivalent to the Al7075 T6 sample.

In order to confirm the composition of the matrix and the inclusions, energy-dispersive X-ray spectroscopy (EDX) was performed on the Al7075 FSP T6 sample, using the *Zeiss FEG-SEM Ultra 55* scanning electron microscope. As shown in Figure 27, two zones free of inclusions were defined for the matrix and some inclusions were individually pointed out, to get their composition.

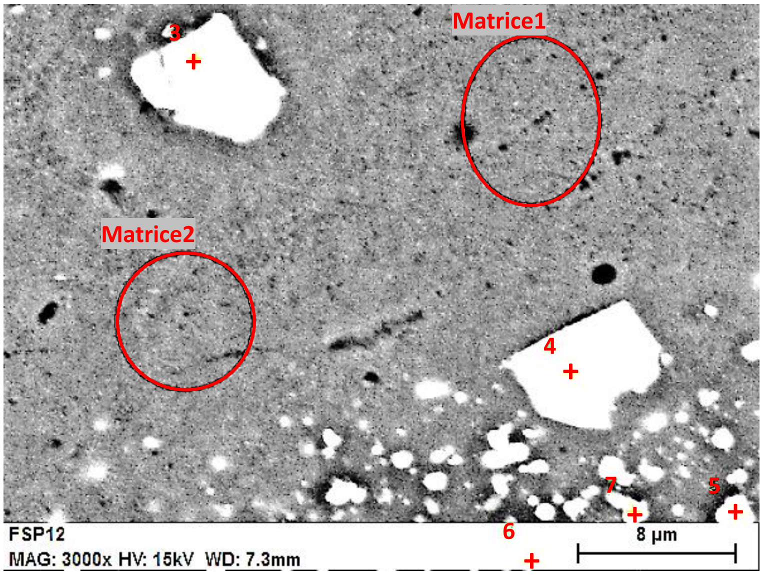

Figure 27: SEM image of the zones where energy-dispersive X-ray spectroscopy was performed.

In the zones highlighted, the following elements were detected: Al, Mg, Zn, Cu, Si, Cr, Fe, C and O. Once the C and O are removed as they are caused by surface oxidation and grease, the composition closely matches what can be found in literature. Indeed, the mass composition measured for both matrix zones is 89% Al, 5.6% Zn, 3.3% Mg, 1.3% Cu, 0.4% Si, 0.17% Cr and traces of Fe. When it comes to the inclusions pointed out, however, they seem to have different compositions. Indeed, depending on the inclusion pointed, a dominance of Fe, Cr, Mg or Zn can be found. This highlights a non-homogeneous distribution of elements between the different inclusions. Note that the full spectrum as well as the normalized mass and atomic composition of each zone highlighted can be found in the Annex 6.3.

Several critics must be made about this EDX test.

1. The EDX detector is calibrated for a working distance of 6 mm while these measurements are made at 7.3 mm. Therefore, the accuracy of the proportion of each element is not optimum.
2. The interaction pear of the EDX spectroscopy is of the order of 1 $\mu m^3$. As a result, if the inclusions are flat, there is an influence of the underlying matrix, which can modify their measured composition.
3. To have a better understanding of the composition, other spectroscopy measurements should be performed in different zones of different samples. Since this is not the main subject of the present work, no further investigation was performed and instead reference to literature was chosen.

This EDX spectroscopy shows the non-uniformity of the inclusion phases. Indeed, large Fe-rich inclusions were found, as well as particles containing mainly Cr, Mg or Zn. These inclusions, broken into smaller, round particles and spread out by the FSP process, constitute the main damage mechanism in the 7xxx alloys, as mentioned by Lezaack et al. [47]

Table 6 summarizes the properties measured as described in this section and compares it to what can be found in literature. [47] [48] [55] [63]

| **Property** | **Al7075 T4** | **Al7075 T6** | **Al7075 FSP T6** | **Ti6Al4V** | **Ni bulk** |
|---|---|---|---|---|---|
| $\sigma_u$ (Micro-hardness) | 500 MPa | 600 MPa | 620 MPa | 1050 MPa | 330 MPa |
| $\sigma_u$ (Nano-hardness) | 410 MPa | 460 MPa | 460 MPa | 790 MPa | 360 MPa |
| $\sigma_y$ | 450 MPa | 540 MPa | 550 MPa | 900 MPa | 300 MPa |
| $E$ | 72 GPa | 75 GPa | 69 GPa | 102 GPa | 172 GPa |
| $E$ | 72 GPa | 72 GPa | 72 GPa | 114 GPa | 200 GPa |
| $\rho_s$ | 2 800 kg/m$^3$ | 2 800 kg/m$^3$ | 2 800 kg/m$^3$ | 4 500 kg/m$^3$ | 8 900 kg/m$^3$ |

Table 6: Summary of the mechanical properties obtained with the experiments, compared with the values found in literature. Note that the values from literature are highlighted in orange the table.

### 4.1.2 Erosion mechanisms

In order to have an insight on the erosion mechanisms, the samples were observed with scanning electron microscopy (SEM). Let's start by looking at the samples exposed to the **PJET**.

#### PJET

As a reminder, the erosion pattern of the PJET consists in 2 sets of 4 impact zones, one at 225 m/s (zones A to D) and the other at 180 m/s (zones E to H). The number of impacts $n$ and total received energy $\varepsilon_{tot}$ is reminded in Table 7.

| **Zone** | $v_0$ **[m/s]** | $n$ **[-]** | $\varepsilon_{tot}$ **[J]** |
|---|---|---|---|
| A | 225 | 1 000 | 106 |
| B | 225 | 5 000 | 530 |
| C | 225 | 10 000 | 1 060 |
| D | 225 | 20 000 | 2 120 |
| E | 180 | 1 000 | 68 |
| F | 180 | 5 000 | 339 |
| G | 180 | 10 000 | 679 |
| H | 180 | 20 000 | 1 357 |

Table 7: Erosion conditions for each of the 8 zones, named A to H following the convention of Figure 11, tested using the PJET facilities.

As foreword, one should note that the Ti6Al4V sample has undergone a different erosion pattern. Indeed, the Ti6Al4V tested using the PJET facilities showed excellent resistance to erosion. The first set of impacts at 225 m/s (zones A to D) still had almost a mirror like appearance. Therefore, instead of testing zones E to H with impacts at lower speeds, namely at 180 m/s, the second line was used for more impacts at 225 m/s. The idea was to reach a surface roughness that would be similar to other materials in order to make a correlation between the number of impacts and the materials properties. Still, for a question of time of experiment, only zones E and F were tested, with 30 000 and 40 000 impacts respectively, at 225 m/s. As a result, the total energy received by zones E and F for the Ti6Al4V sample is 3 180 J and 4 240 J respectively.

As previously highlighted, SEM works best for heavily eroded samples, where the contrast is sufficient to observe the erosion mechanisms down to the sub-micron scale. This means that only the zones D and H of the PJET samples, which are the most heavily eroded, give relevant images.

When it comes to erosion mechanisms, two categories can be distinguished: the macro-scale and the micro-scale.

At the macro-scale, every sample showed shallow depressions, similar to a soft peening. The surface is not perfectly smooth and flat but shows a smooth profile, with valleys of the order of 10 µm width. This is illustrated on the zones H of the Ni bulk and Al7075 T4 samples in Figure 28, observed with scanning electron microscopy. Similar behavior can be seen with digital microscopy, with a higher contrast, as illustrated in Figure 29.

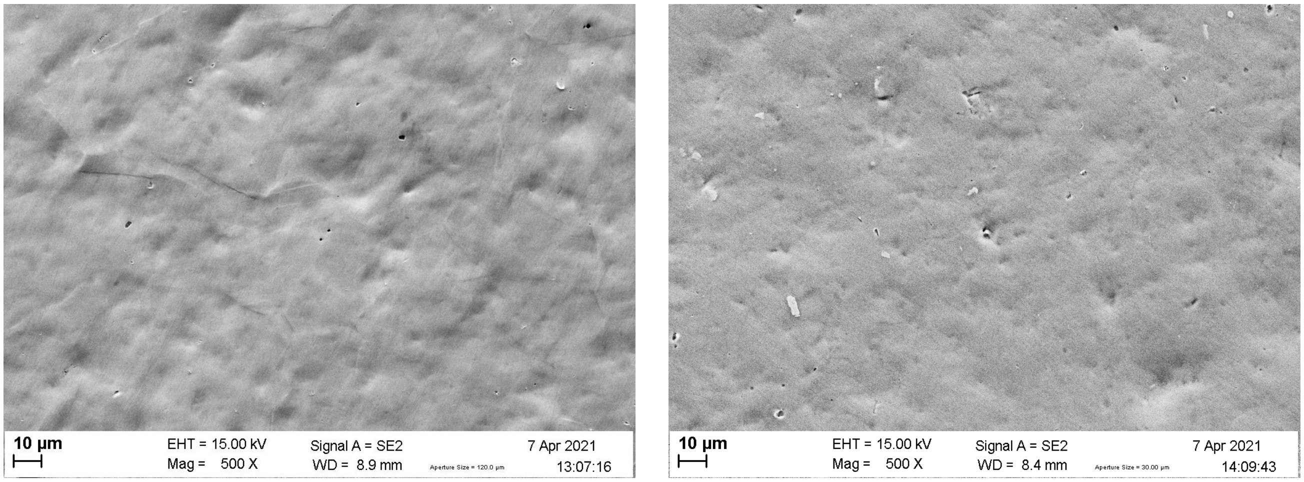

(a) Ni bulk - Zone H

(b) Al7075 T4 - Zone H

Figure 28: SEM low magnification images showing the smooth depressions on two PJET samples, namely (a) Ni bulk and (b) Al7075 T4.

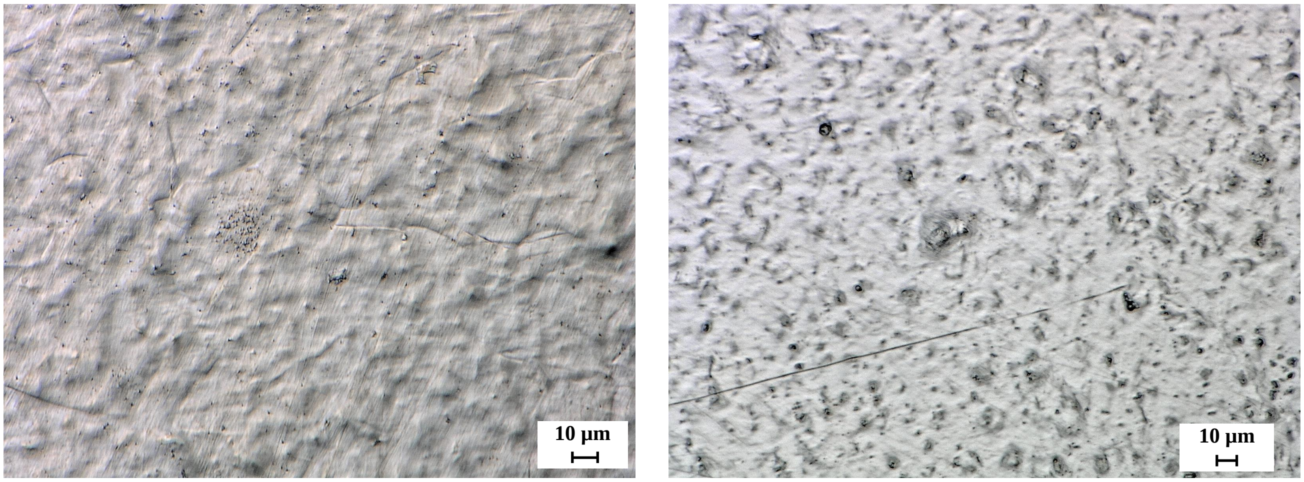

(a) Ni bulk - Zone H

(b) Al7075 T4 - Zone H

Figure 29: Digital microscopy images showing the smooth depressions on two PJET samples, namely (a) Ni bulk and (b) Al7075 T4.

One can see on the images of Figures 28 and 29 wide craters of the order of 10 to 20 µm in diameter interpenetrated, creating soft, smooth hills on the sample surface. In certain positions, the relief is more accentuated but at this macro-scale, only shallow depressions can be observed using SEM. However, due to its higher contrast, digital microscopy allows to have more details on the shape and distribution of these shallow depressions.

It is interesting to note that these smooth depressions can be observed in the most heavily eroded zone (D and H) of every sample. This large scale phenomenon is not responsible for material loss as it simply redistributes the matter, creating smooth valleys and peaks of tens of microns width. However, these localized depressions lead to the generation of surface asperities, which can in turn trigger material loss. As shown by Kirols et al. [65] these created surface asperities increase the local impact pressure, triggering further damage.

These shallow depressions are also present, but less sharp on the Ti6Al4V sample, probably because of the higher hardness of this material, as illustrated in Figure 30. This figure compares the contrast obtained by scanning electron microscopy and by digital microscopy, around the depression highlighted. One should note that the digital microscopy image gives the impression of a peak while both images correspond to the same depression.

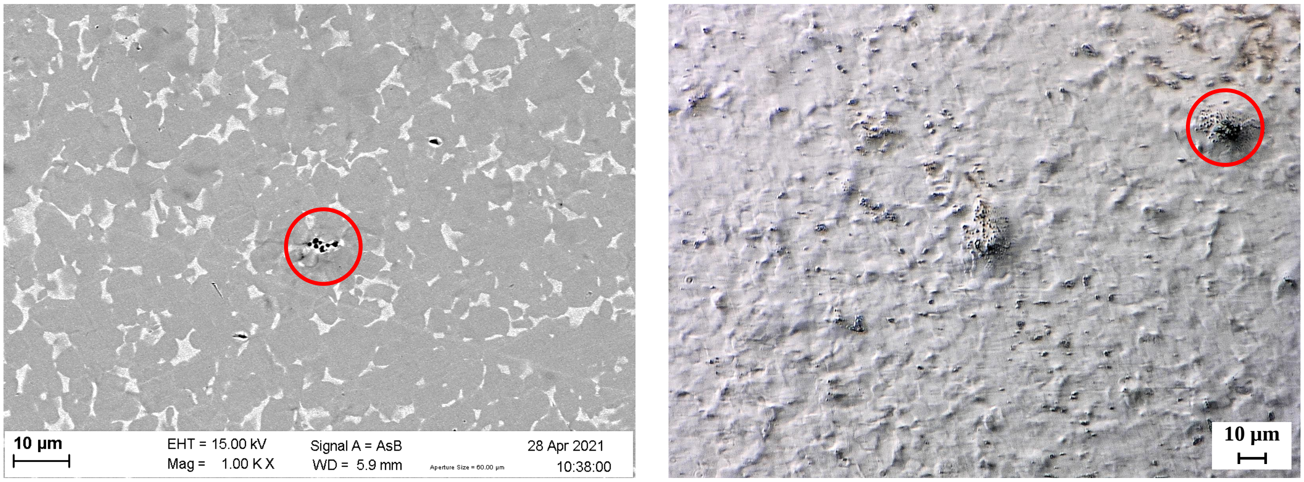

(a) Scanning electron microscopy

(b) Digital microscopy

Figure 30: Comparison of (a) scanning electron microscopy and (b) digital microscopy images at low scale of sample Ti6Al4V - Zone F. The two phases ($\alpha$ and $\beta$) constituting Ti6Al4V can be seen in image (a) while image (b) better highlights the contrast of the topography.

In addition, Figure 30 clearly shows the distribution of both phases constituting the Ti6Al4V alloys, namely phases $\alpha$ and $\beta$. One notices that the shallow depressions observed with high contrast on the digital microscopy image seem to correspond in terms of shape and size with the two phases illustrated in the SEM images. The $\beta$ phase has a lower Young's modulus but a higher strength than the $\alpha$ phase. As a result, a possible explanation for the shape of the depressions is that the $\alpha$ phase is impinged, due to its lower strength while the $\beta$ phase remains at the original level. Therefore, the surface remains globally flat, except at the location of the $\alpha$ phase, where it collapses.

On the other hand, if the samples are observed at much higher magnification, sub-micron damage phenomena can be observed, such as pitting. As shown by Kirols et al. [18], pits are nucleated in isolated locations in polished samples, then grow and merge to form erosion craters. Sample Al7075 T6 shows very interesting results, as can be seen in Figure 31.

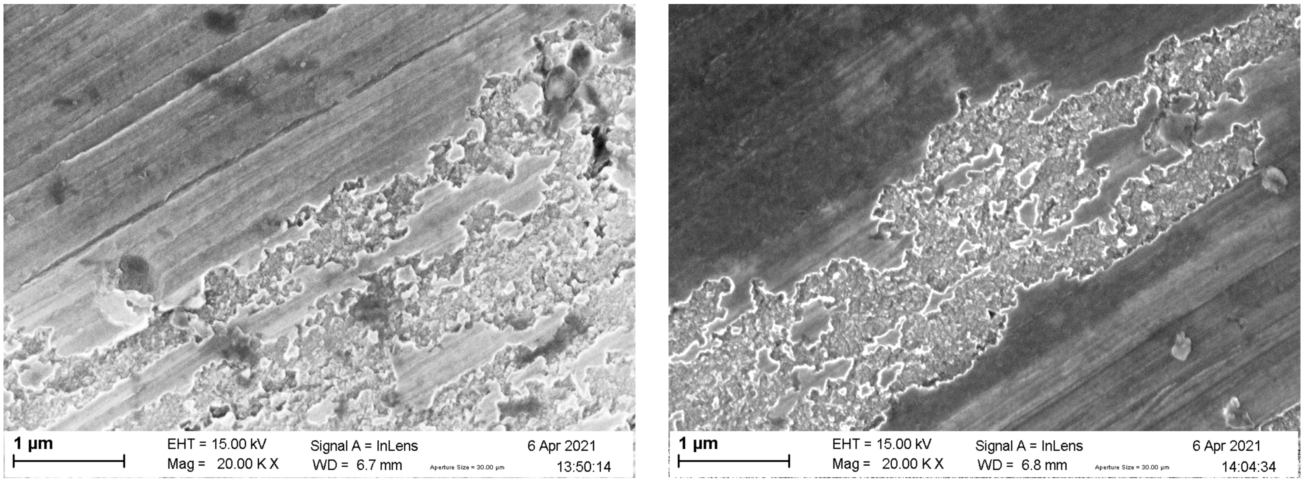

(a) Al7075 T6 - Zone D

(b) Al7075 T6 - Zone H

Figure 31: SEM high magnification images showing the pitting of the Al7075 T6 sample after PJET erosion, in (a) Zone D and (b) Zone H.

Both pictures of Figure 31 show very specific, oriented direction of pitting. This direction follows perfectly the grooves created by the polishing. WDE therefore seems to start the pitting along the weakest direction, which is following the existing defects, in this case the aligned grooves. Figures 31a and 31b demonstrate that the zones of pitting start along the scratches then grow transversely, broadening the aligned pits. The pits have dimensions around 100 nm individually and coalesce along the preferential direction.

Surprisingly, this alignment of pitting with the polishing scratches was not as heavily marked on the other samples. It is still present, as can be seen in Figure 32, but to a lesser extent.

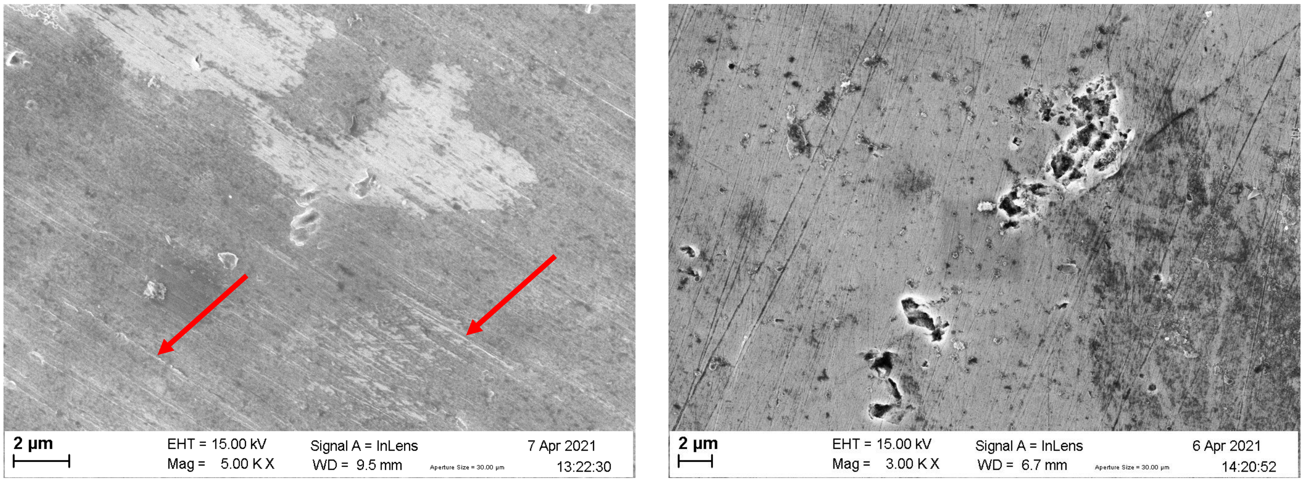

(a) Al7075 FSP T6 - Zone D

(b) Ni bulk - Zone D

Figure 32: SEM high magnification images showing the orientation of pitting following the scratches direction of samples (a) Al7075 FSP T6 and (b) Ni bulk samples after PJET erosion.

On top of this oriented cluster of pitting points, isolated pitting zones are also present. Indeed, during the first stages of erosion, a few localized damage initiation zones create isolated pits, which then grow with the directional preference as shown above. Two examples are shown in Figure 33 on the Al7075 T4 and Ni bulk samples.

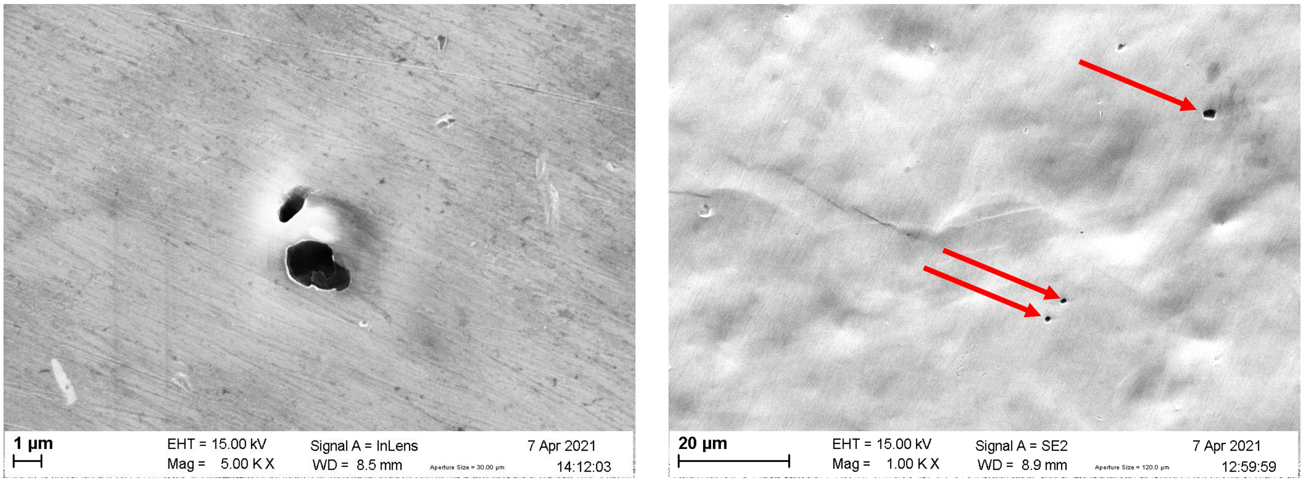

(a) Al7075 T4 - Zone H

(b) Ni - Zone H

Figure 33: SEM high magnification images showing the localized pitting of samples (a) Al7075 T4 and (b) Ni bulk after PJET erosion.

The pits seen in Figure 33 have dimensions between 2 µm and 5 µm. This is significantly larger than the width of the grooves observed in Figure 31. A possible explanation for this difference in scale is the damage initiation feature. Indeed, the erosion mechanism in Figure 31 is initiated by the scratches, which are local stress concentrating points of very small dimensions ($\approx$ 100 nm wide). On the other hand, the pits which appear in a more random pattern, as in Figure 33, are probably initiated by a local, point defect, most likely due to an intrinsic weak point of the material.

Figure 33a is of particular interest as it shows that the water droplets first infiltrate a sub-surface cavity, which is probably a material defect. Then, the cavity entry is broadened, allowing more water to infiltrate and blowing it open. Because of the lateral jetting, the material that was pushed up by the infiltrating water will be sheared away, leaving a 2 µm wide circular pit. Such pits can be observed in Figure 33b.

Note that Figure 32b shows an erosion behavior in the Ni bulk sample that is in between both damage mechanisms. Indeed, since the scratches are not as deep as in the Al7075 samples, the pits are still preferably nucleated on the scratches but are not as aligned in the Ni bulk sample. In addition, the width of those pits is comprised between the individual larger pits and the scratches-nucleated oriented pits.

When it comes to the Ti6Al4V sample, eroded in the PJET, a pitting behavior similar to the Ni bulk sample can be observed. Indeed, as can be seen in Figure 34, several pits are nucleated in a localized depression, with no significant alignment. As the material is hard compared to the aluminum alloys, the scratches from the polishing are less pronounced, leading to an erosion damage in the form of localized pitting zones. Note that in Figure 34, the pitting initiation zone seems to coincide with the boundary between phases $\alpha$ and $\beta$, which is known to be a weak point, initiating damage.

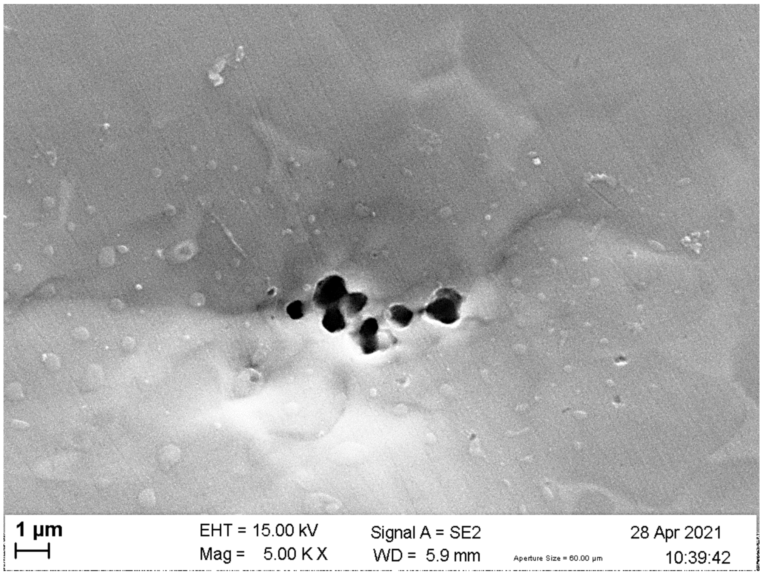

Figure 34: SEM images showing localized pitting of the PJET-eroded sample Ti6Al4V - Zone F.

Both micro-size erosion mechanisms, namely the localized random pitting and the scratches widening, can be observed with high contrast using digital microscopy. This is illustrated in Figure 35, where both aligned, broadening scratches and localized round pits can be seen on samples Al7075 T6 and Al7075 FSP T6.

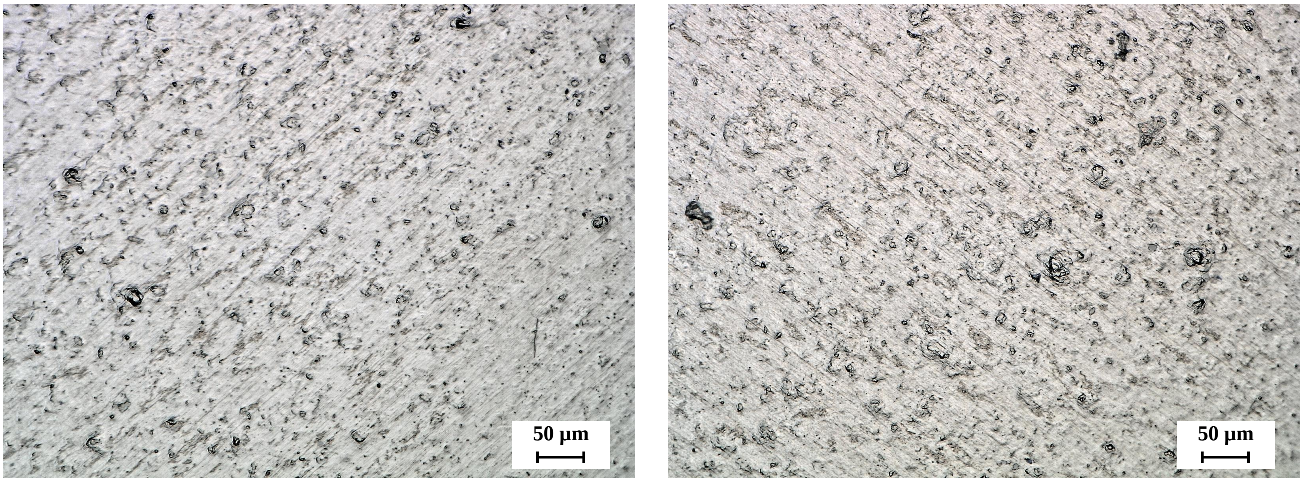

(a) Al7075 T6 - Zone D

(b) Al7075 FSP T6 - Zone D

Figure 35: Digital microscopy images of zone D of samples (a) Al7075 T6 and (b) Al7075 FSP T6 showing both micro-scale erosion mechanisms: localized pitting and grooves widening.

### WARER

Let's now look at the erosion mechanisms in the samples eroded in the **WARER** and compare them with the PJET erosion mechanisms. As a reminder, the erosion conditions in the WARER are 2 mm diameter droplets impacting the rotating sample at a speed of 120 m/s. The erosion zone is a 28 mm diameter disk, impacted by the droplets at a frequency of 40 Hz. The total exposure duration is 18 hours, corresponding to 2.6 million droplet impacts over the entire surface.

As shown earlier, the distribution of droplet impacts on the sample surface is uneven. Therefore, in order to compare the damage of the samples with similar exposure to erosion, all the WARER samples were observed in the SEM at the center of the 28 mm diameter disk. The following images illustrate the erosion mechanisms of the samples tested with the WARER using scanning electron microscopy. Still, in the Annex 6.4, images of each sample taken with the digital microscope can be found. One should note that because of the flow of air and water, corrosion and oxidation are highly present on the surface of the WARER eroded samples. As a result, the images taken with digital microscopy do not give a good topographic contrast, unlike the SEM images.

As can be seen in Figure 36, the Al7075 T4 sample shows severe erosion, with distinct alignment of the pitting with the polishing scratches. Indeed, Figure 36a shows that the polishing grooves are nucleating sites for the pitting mechanism, widening the scratches as erosion progresses. In addition, more random pitting zones can be observed in Figure 36b where the cracks merge into larger pits of dimensions up to 5 µm in diameter.

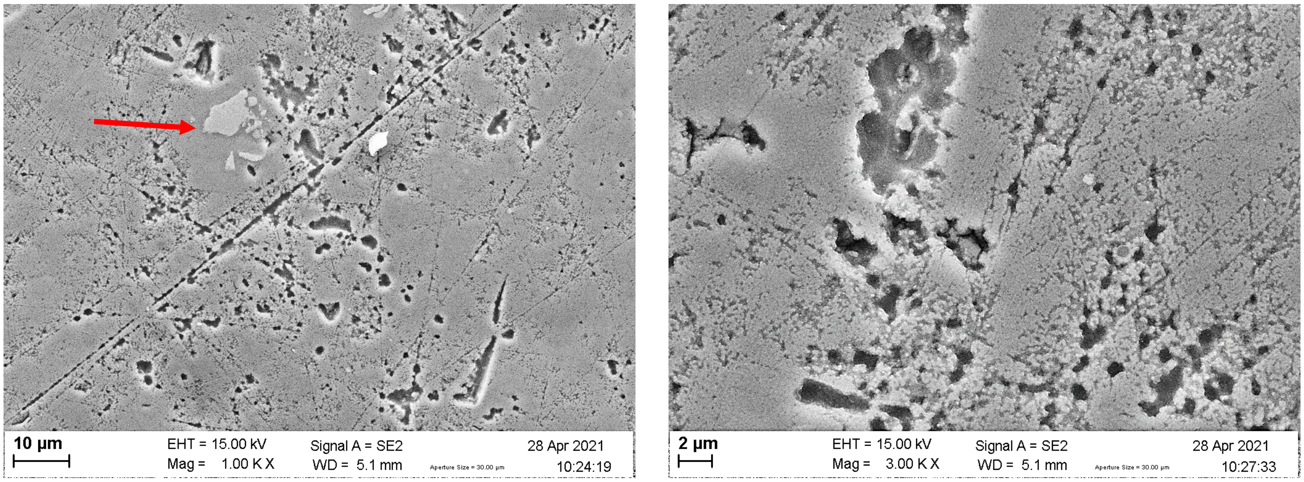

(a) (b)

Figure 36: Scanning electron microscopy of the Al7075 T4 sample eroded using the WARER for 18 hours at (a) low magnification and (b) higher magnification.

One should note, as highlighted in Figure 36a with a red arrow, that no damage is observed on and around the inclusion. This can be explained by the nature of this inclusion, which is significantly harder than the matrix. This will be discussed in more details further.

The WARER Al7075 T6 sample does not show as deep scratches as the PJET Al7075 T6 despite a similar polishing technique. As a result and as can be seen in Figure 37, there is no preferential direction of erosion. The damage mechanism is isolated pits, with diameters up to 5 µm. One should note that compared to the WARER Al7075 T4 sample, those pits are less abundant but still merge to form deeper, wider ditches.

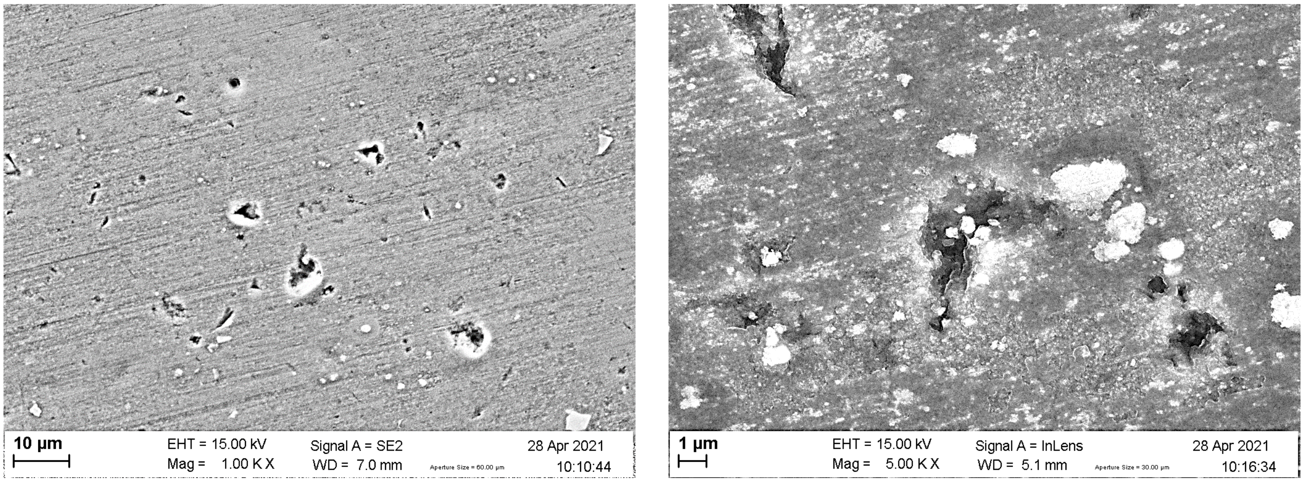

(a) (b)

Figure 37: Scanning electron microscopy of the Al7075 T6 sample eroded using the WARER for 18 hours at (a) low magnification and (b) higher magnification.

When it comes to the Al7075 FSP T6 sample, as can be seen in Figure 38, the number and size of the pits are comparable to those of the WARER Al7075 T6 sample. Indeed, the pits are individually nucleated, then merge with the adjacent ones, creating ditches of about 5 µm diameter. Note that on the right of Figure 38a, a trench can be observed, which seems to follow the vertical direction of the polishing grooves. This confirms the two parallel damage initiation mechanisms: locally nucleated pits and pits initiated along scratches. Based on both PJET and WARER eroded samples, at this level of WDE, the influence of the improved ductility brought by the friction stir processing does not seem to be significant. Further tests should be performed at heavier or longer erosion conditions to confirm or infirm this observation.

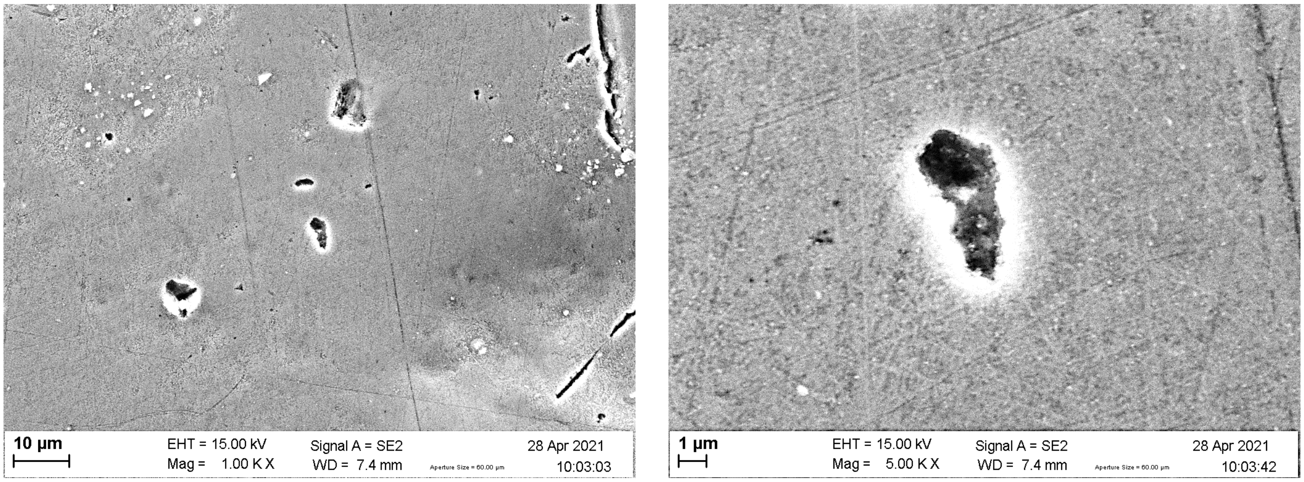

(a) (b)

Figure 38: Scanning electron microscopy of the Al7075 FSP T6 sample eroded using the WARER for 18 hours at (a) low magnification and (b) higher magnification.

Figure 39 shows the damage mechanisms on the Ni bulk sample eroded in the WARER. Note that this sample was exposed during 12 hours, while the other ones were exposed during 18 hours. Still, the erosion mechanism is similar to the PJET eroded sample and consists mostly of isolated pits, of size 1-2 µm, which are spaced by around 20-50 µm.

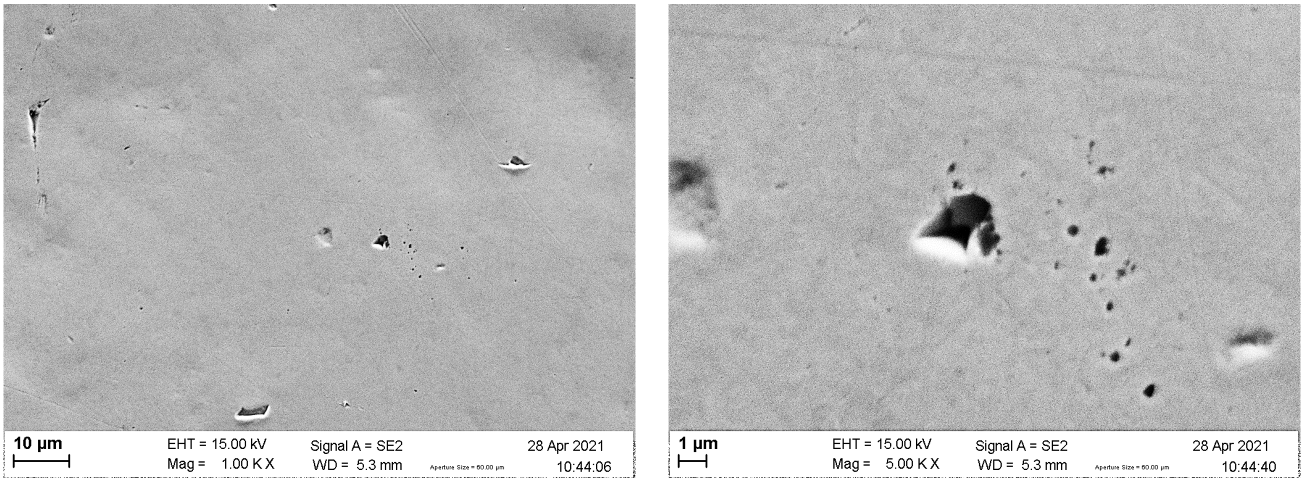

(a) (b)

Figure 39: Scanning electron microscopy of the Ni bulk sample eroded using the WARER for 12 hours at (a) low magnification and (b) higher magnification.

Finally, the damage mechanism of the Ti6Al4V sample eroded with the WARER can be seen in Figure 40. One notices that the damage is mostly in the form of randomly distributed circular pits. In addition, deep and sharp scratches can be observed, but these correspond to solid particle impacts, as discussed further.

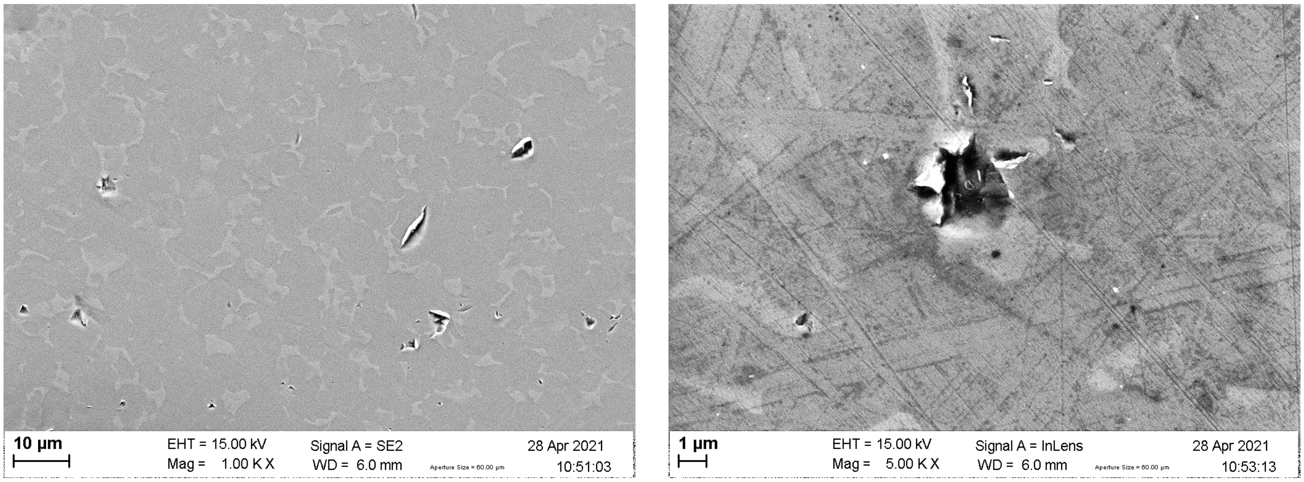

(a) (b)

Figure 40: Scanning electron microscopy of the Ti6Al4V sample eroded using the WARER for 18 hours at (a) low magnification and (b) higher magnification.

Note that on all the samples eroded with the WARER presented above, another type of damage can be observed, in the form of narrow sharp scratches, sometimes ending with a neat bend. Representative examples on the Al7075 FSP T6 and Ti6Al4V samples are shown in Figure 41, but this was observed on every WARER eroded sample. The damaged zones highlighted with the red circles show distinct and sharp edges, which are presumably explained by another mechanism than water droplet impingement. The most probable explanation for this type of damage is the erosion due to solid dust particles, present in the chamber of the WARER machine. Indeed, such particles, of the order of 10 µm can be in suspension in the air of the chamber and be impacted by the rotating arm. This is confirmed by the presence of a pile-up flange, indicating the direction of the impacting solid-particle, which is then dislodged leaving a sharp and rectilinear scratch. In addition, this is not observed in the PJET samples as they are stationary, avoiding this solid particle impingement.

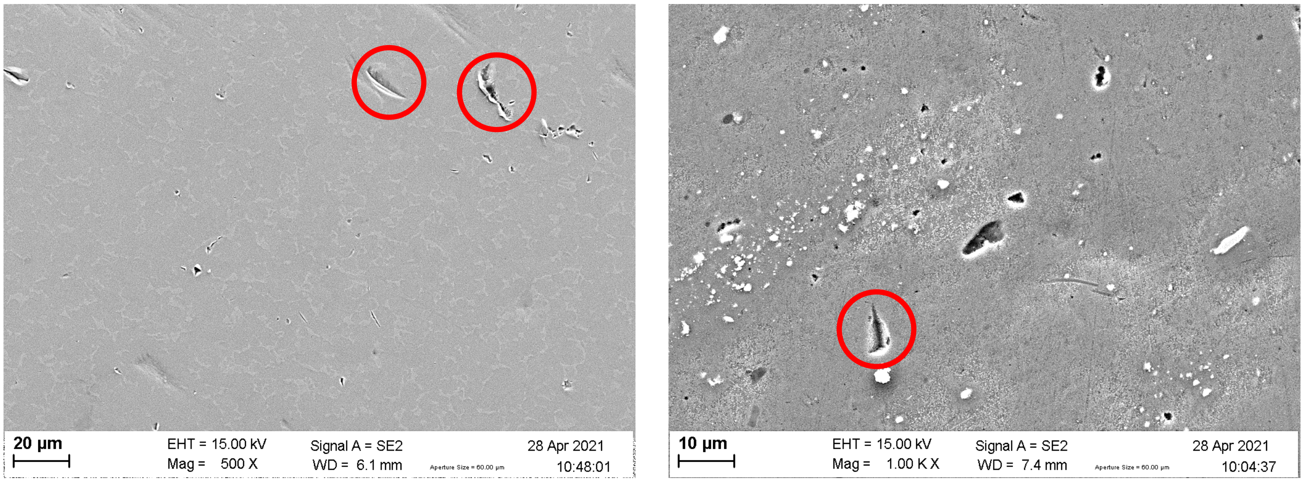

(a) Ti6Al4V - WARER

(b) Al7075 FSP T6 - WARER

Figure 41: Scanning electron microscopy images of the (a) Ti6Al4V and (b) Al7075 FSP T6 samples eroded 18h in the WARER facility showing deep, sharp scratches, probably caused by solid particles impingement.

Finally, one should also notice that the size distribution of the pits is broader in the WARER samples than in the PJET samples. This could be explained by the broader distribution of the droplet size in the WARER. Indeed, some droplets fall against the wall of the dispenser tubes, merging into larger droplet, which are known to cause more erosion damage due to their higher kinetic energy. As a result, the erosion conditions vary more significantly in the WARER than in the PJET, which is calibrated to give a narrow droplet size distribution. This explains why the pits have more varied sizes in the WARER eroded samples.

In conclusion, the damage mechanism seems globally comparable between the PJET and WARER techniques for the samples tested in the present work. Still, some differences should be highlighted:

1. The erosion mechanism at the macro-scale is not identical. Indeed, in the PJET eroded samples, wide and shallow depressions are created due to the consecutive droplets impacting the same zone of the sample. Because of this higher number of impacts per unit surface, the PJET creates a smooth, macro-scale peening-like relief. This cannot be observed on the WARER samples.
2. At a small, micro-scale, both WARER and PJET techniques lead to pitting. Both testing techniques show two similar damage mechanisms. On one hand, pits are nucleated at the scratches and groves created by the polishing step. This causes long, oriented and parallel trenches widening with erosion. On the other hand, isolated pits are also nucleated in a more random fashion, probably at local point defects of the material. Those pits then grow in diameter, possibly merging with neighboring ones, reaching a maximum final diameter of 5-10 µm in the erosion conditions of the present work.
3. The samples eroded with the WARER technique show an additional damage mechanism, expressed as short and narrow but deep scratches. This damage mechanism is probably explained by dust particles present in the WARER, which are impacted by the rotating arm.

### 4.1.3 Roughness evolution

Despite the observed damage mechanisms, no significant material loss was measured for the WARER samples. Indeed, these samples probably remained in the incubation stage, where the surface topography is altered without significant mass loss. In addition, as already mentioned, for the PJET samples, due to the machine configuration and the large dimensions of the sample compared to the eroded zone, the possible material loss could not be measured. Therefore, the evolution of the cumulative weight loss typically used to characterize the evolution of erosion, as in Figure 2, could not be used in the present work. Instead, the erosion of the materials was quantified using roughness measurement parameters.

Before looking at the evolution of the roughness parameters, let's compare visually the different PJET-eroded samples. Figures 42 and 43 show digital microscopy images of the eroded regions for each of the 8 zones of the three different Al7075 samples. The eight erosion zones of the Ni bulk sample are displayed in Figure 44 while Figure 45 illustrates the 6 eroded zones on the Ti6Al4V sample. Note that all these pictures depict the entire erosion zone. Therefore, each picture represents a zone of dimensions 1.4 mm by 2 mm. Note that slight variations in scale are present in certain images, but this does not affect the global picture comparison.

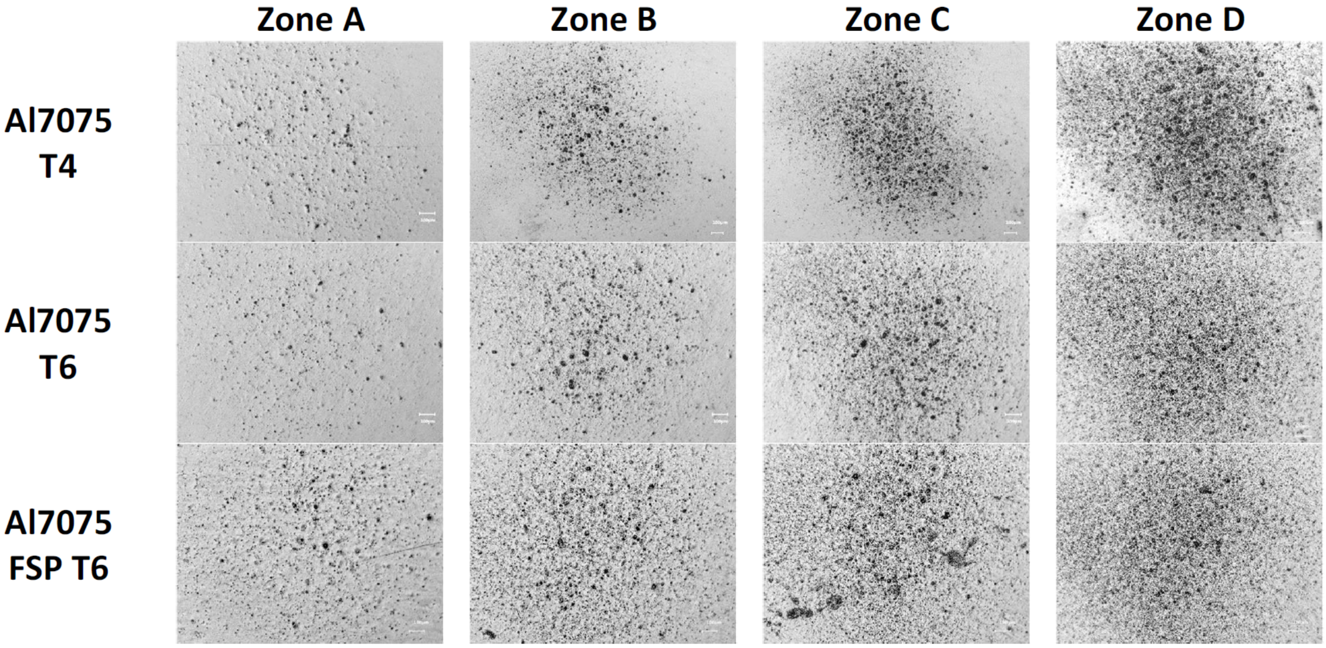

Figure 42: Digital microscopy images of the PJET zones A to D (impacts at 225 m/s) of the samples Al7075 T4, Al7075 T6 and Al7075 FSP T6.

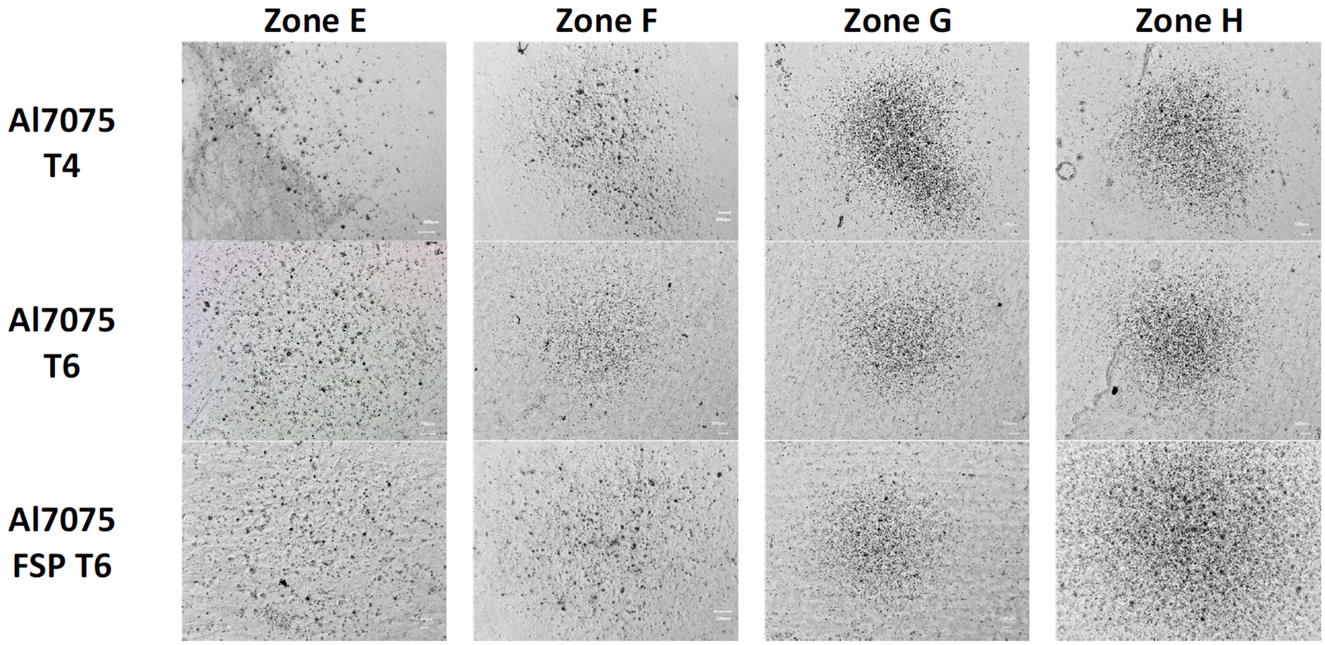

Figure 43: Digital microscopy images of the PJET zones E to H (impacts at 180 m/s) of the samples Al7075 T4, Al7075 T6 and Al7075 FSP T6.

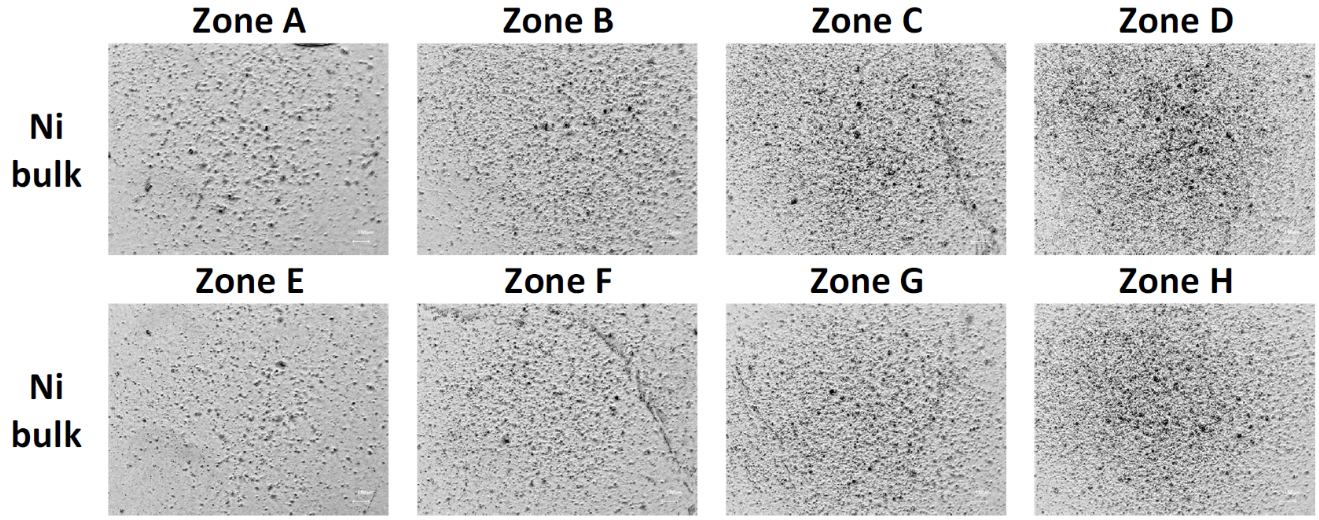

Figure 44: Digital microscopy images of the PJET zones A to D (impacts at 225 m/s) and E to H (impacts at 180 m/s) of the sample Ni bulk.

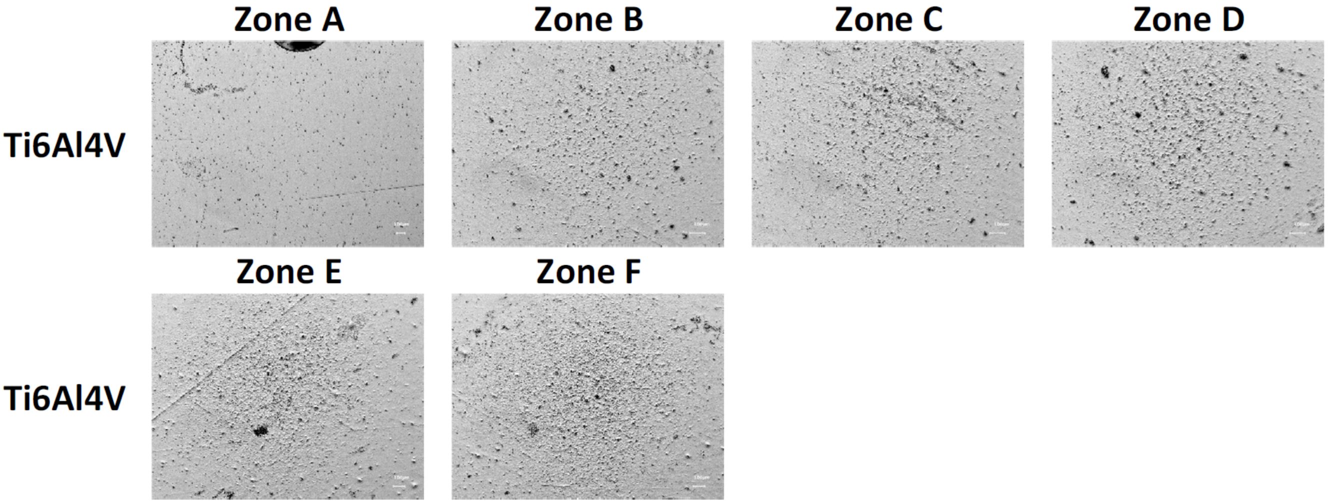

Figure 45: Digital microscopy images of the PJET zones A to F (impacts at 225 m/s) of the sample Ti6Al4V.

Let's look at the evolution of the roughness parameters computed using laser interferometry for the different erosion zones made by the PJET. Note that, due to the fringe interference limitation of the laser interferometer, the roughness parameters of the two first impact zones of the Ti6Al4V sample (zones A and B) could not be measured with significant results. The values of the roughness parameters discussed, namely $R_a$, $R_{ku}$ and $R_{sk}$, of every zone of each material eroded using the PJET can be found in the Annex 6.5. The same roughness parameters computed for the samples eroded in the WARER are also summarized in Annex 6.5.

Since the damage mechanisms are comparable in all the samples due to similar erosion conditions, one could use the arithmetic mean roughness, $R_a$, as a way to classify their resistance to erosion. Still, the information given by this parameter is limited. Figure 46 shows the evolution of the $R_a$ value of the Al7075 samples as a function of the total received energy, defined as the number of impacts times the kinetic energy of a single droplet, for tests at 180 m/s. Figure 47 also shows the evolution of the $R_a$ value as a function of the total energy received but for impact speeds of 225 m/s.

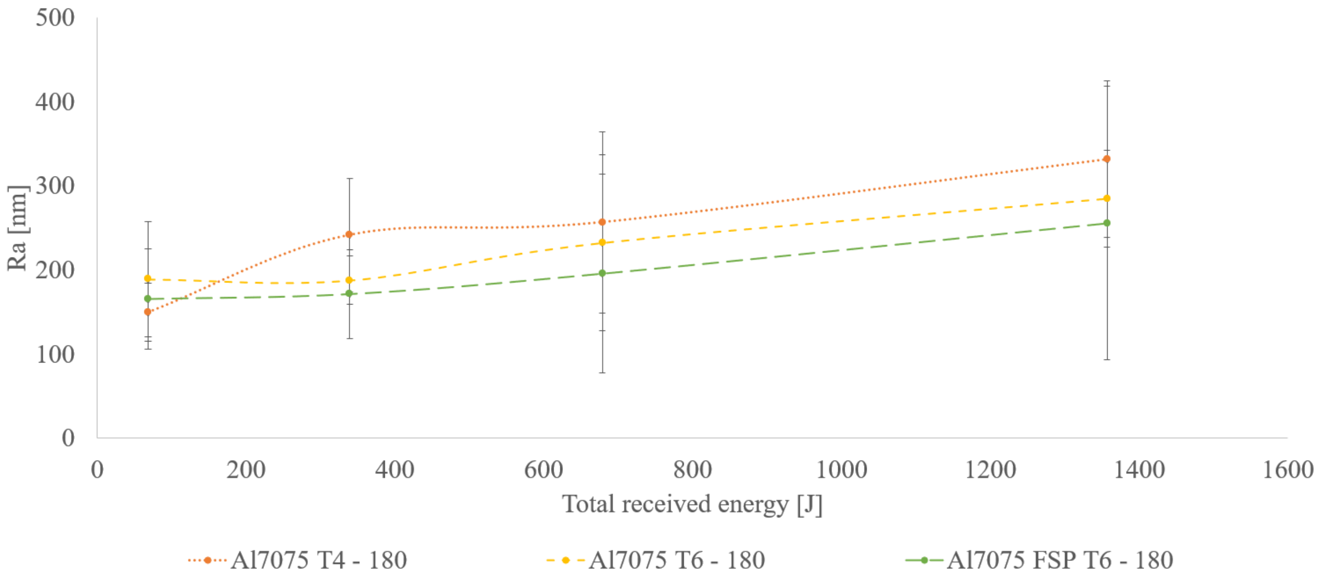

Figure 46: Evolution of the $R_a$ of the Al7075 T4, Al7075 T6 and Al7075 FSP T6 samples as a function of the energy received, for impact speeds of 180 m/s in the PJET.

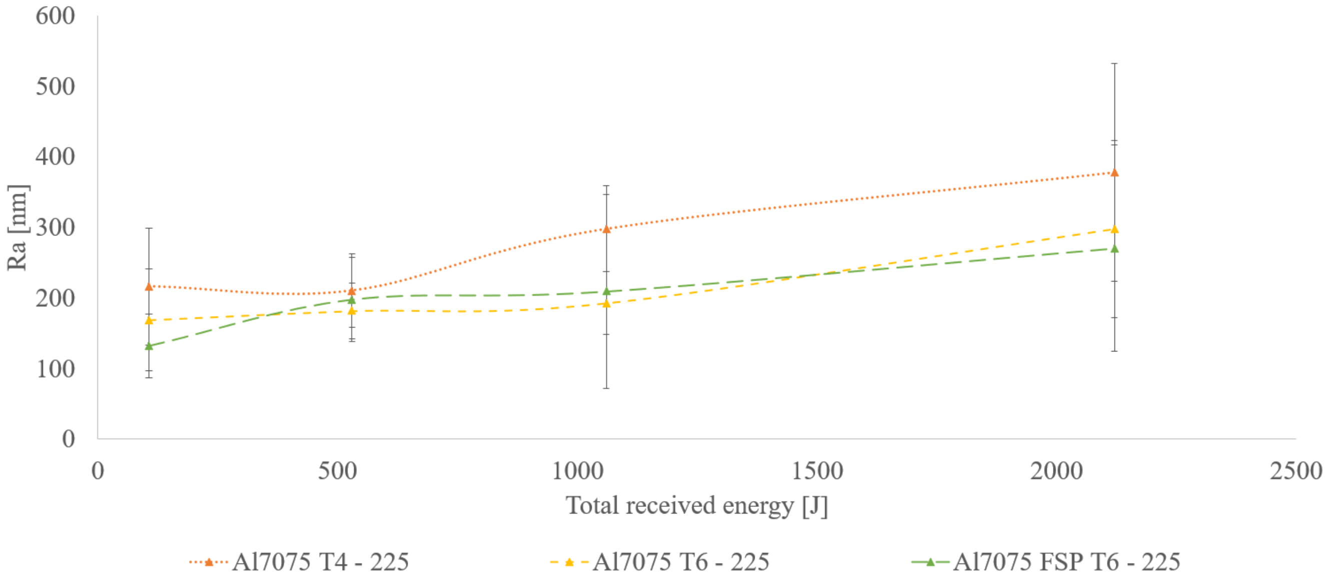

Figure 47: Evolution of the $R_a$ of the Al7075 T4, Al7075 T6 and Al7075 FSP T6 samples as a function of the energy received, for impact speeds of 225 m/s in the PJET.

A first disclaimer regarding Figures 46 and 47 is that the error bars represent the standard deviation of the 88 parallel profiles computed on the area scanned by the laser interferometer. Despite the large deviation shown by these error bars, global trends can be deduced from the profiles. This remark holds true for the following roughness evolution and comparison graphs, as they all show significant error bars.

In both Figures 46 and 47, the $R_a$ of the samples increases with the energy received. This is in accordance with the erosion mechanisms in which shallow depressions first appear, then pits are nucleated within these depressions and grow. This would justify the increasing $R_a$, which could be assessed with the naked eye.

Note that based on Figures 46 and 47, the three alloys can be classified by increasing erosion resistance as Al7075 T4, then Al7075 T6 then Al7075 FSP T6, which corresponds to the same ranking as the hardness. The comparison using $R_a$ is relevant because all three samples are of the same material, with only slightly varying mechanical properties.

When the $R_a$ values of all five samples tested at 225 m/s are drawn on the same graph, as in Figure 48, two classes of materials can be distinguished. Indeed, the three aluminum alloys and the Ni bulk sample show a significant increase in $R_a$ with erosion while the Ti6Al4V sample has a more stable and lower value of $R_a$ with erosion. Based on Figure 48, looking at zone D which corresponds to a total received energy of 2120 J, the materials can be ranked in increasing resistance to WDE as follows: Al7075 T4, Al7075 T6, Ni bulk, Al7075 FSP T6 and Ti6Al4V. This ranking does not perfectly correspond to the visual observation seen in Figures 42, 43, 44 and 45, where the Ni bulk sample seems to sit in between the Al7075 samples and the Ti6Al4V sample.

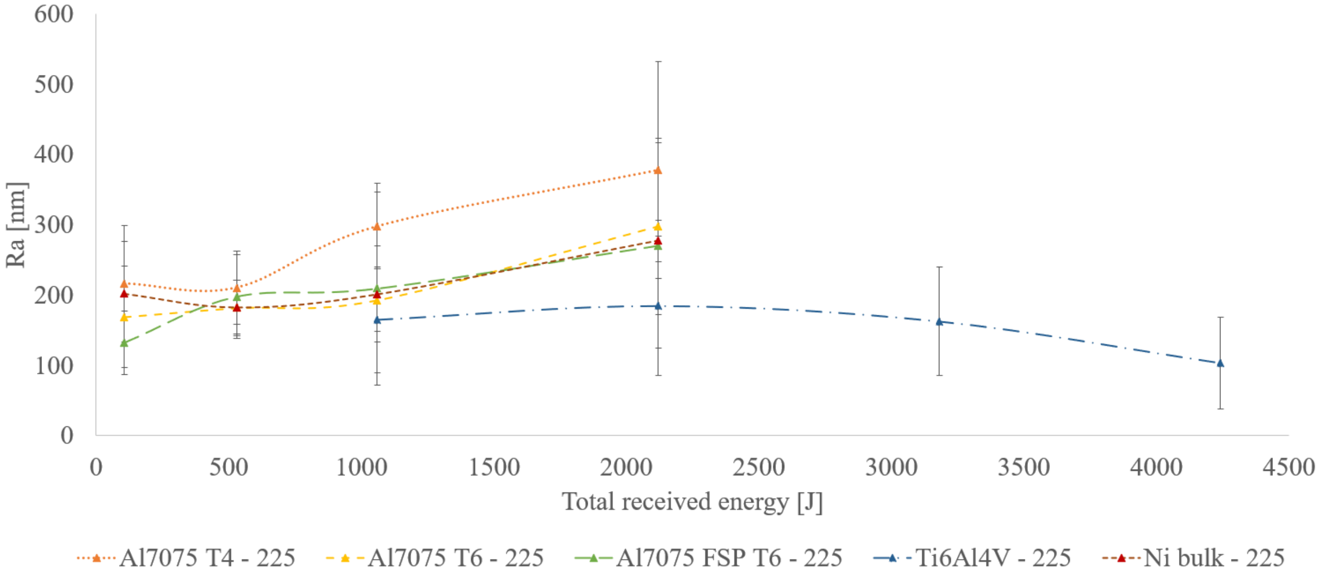

Figure 48: Evolution of the $R_a$ of all five samples as a function of the energy received, for impact speeds of 225 m/s in the PJET.

Since the $R_a$ roughness parameter has limited possible interpretation, one could look at another parameter, namely $R_z$. It has a very similar evolution for all five samples as the $R_a$ curves. Again, the Ti6Al4V sample shows rather steady values of $R_z$ while the other four samples show increasing values of $R_z$. As for the $R_a$ parameter, the amount of information given by the $R_z$ parameter is limited.

Let's therefore analyze the kurtosis $R_{ku}$ of the samples, which is a measure of the sharpness of the profile. A distinction can be seen between the lower speed and higher speed impacts. Indeed, as can be seen in Figure 49, the materials tested with impacts at 180 m/s show a slight increase of the $R_{ku}$ with the received energy. On the other hand, at impact speeds of 225 m/s, all five samples show a trend of decreasing $R_{ku}$ with total energy received, as can be seen in Figure 50. One notices that every sample has a kurtosis $R_{ku} > 3$, which implies that the features are sharper than a Gaussian distribution.

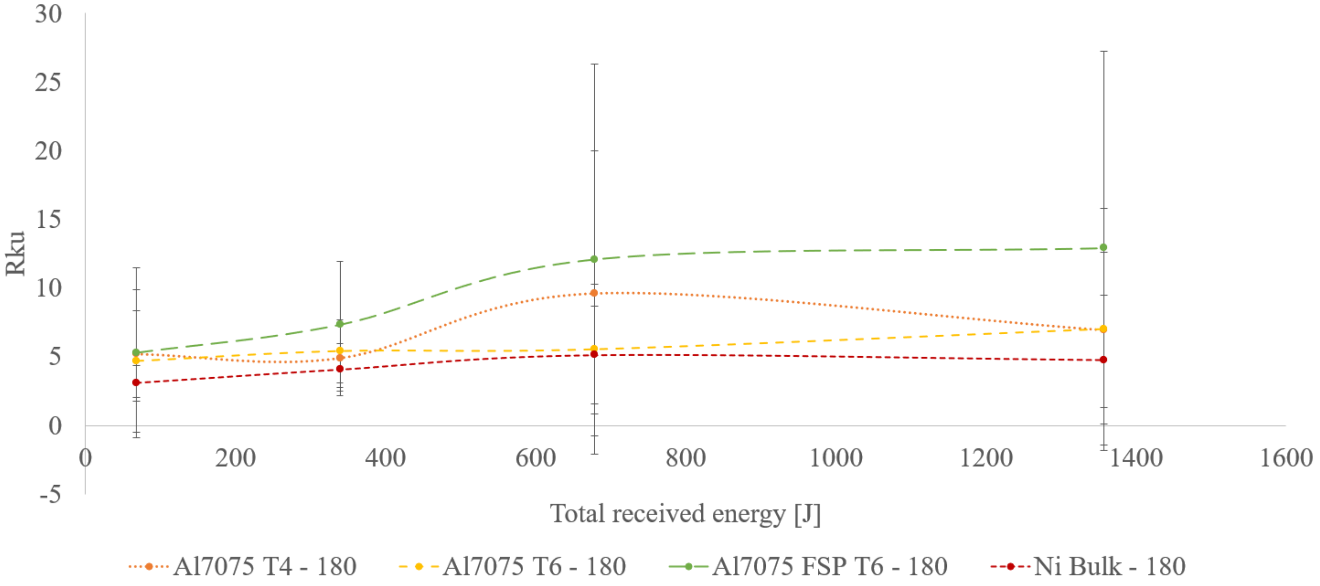

Figure 49: Evolution of the $R_{ku}$ of the Al7075 T4, Al7075 T6, Al7075 FSP T6 and Ni bulk samples as a function of the energy received, for impact speeds of 180 m/s in the PJET.

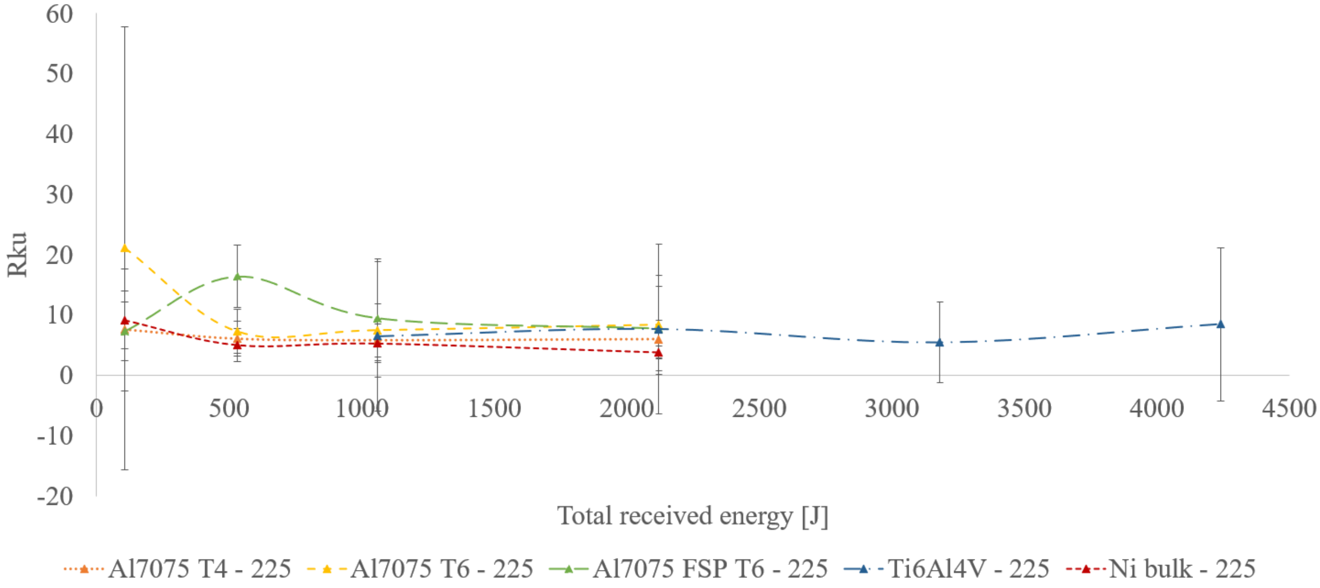

Figure 50: Evolution of the $R_{ku}$ of all five samples as a function of the energy received, for impact speeds of 225 m/s in the PJET.

The evolution of the $R_{ku}$ of the 180 m/s impacts seen in Figure 49 shows a slightly increasing trend while a decreasing trend is observed at 225 m/s impacts, as shown in Figure 50. It seems surprising that the materials exhibit different behaviors for both impact velocities. The erosion mechanisms can be enhanced at higher impact speeds, but fundamentally the behavior should be similar. Still, since the individual droplets have an kinetic energy of 67.86 mJ and 106.03 mJ at 180 m/s and 225 m/s respectively, one should not exclude that slightly different erosion mechanisms can happen depending on the impact velocity. As illustrated in the following graphs, some materials are more sensitive to the impact speed than others, presumably because a threshold is reached in terms of energy received per droplet or equivalently in terms of stress in the material.

An interpretation for the increasing $R_{ku}$ shown at 180 m/s is that, as the droplets have a significantly lower energy each, the depth and sharpness of the impacts they create on the surface of the material are lower than at 225 m/s. As a result, the features created during the first impacts are smoother and show a lower $R_{ku}$ than at higher speed impingement. However, as an increasing number of droplets reaches the surface, the features start deepening as the pitting initiation zones localize the energy and the damage. The zones of the material which undergo very little erosion due to local harder features, such as inclusions or precipitates, remain at the initial surface level while the pits created all around are dug deeper because of the stress concentration they create. Those pits, which are less numerous than at 225 m/s impacts due to the lower droplet energy, are deepened by the subsequent droplets and slightly widened. The result is a profile with increasingly sharp and deep features. This corresponds to the trend of increasing $R_{ku}$ that can be seen in Figure 49.

On the other hand, a possible explanation for the decreasing $R_{ku}$ observed in Figure 50 is that, as the number of impacts increases, the surface irregularities may be smoothed out due to overlapping high energy impacts. Indeed, the first impacts act as if they were independent on the polished surface, creating local craters with steep edges due to the high kinetic energy of the droplets. Indeed, at high speed impacts, the early stages of erosion consist in the creation of sharp and deep pits. This would explain the initially high $R_{ku}$ value. Then, the subsequent droplet impacts smooth out the edges, shearing off the possible pile up and widening the features. Indeed, as exposure to erosion is extended, the hillside of the profile is impacted and possibly sheared out. As a result, the initially very sharp profile, which concentrates the stress of the impacting droplets, becomes smoother as the sharp features are impinged. This would explain the decreasing value of $R_{ku}$ for the 225 m/s impacts, seen in Figure 50.

Finally, let's examine the evolution of the skewness parameter $R_{sk}$, which gives the asymmetry of the profile with respect to the mean line. As shown earlier in this work, the skewness parameter $R_{sk}$ illustrates best the loss of matter, the pitting and the impingement phenomena. The evolution of the $R_{sk}$ of the samples tested at 180 m/s and 225 m/s can be found in Figures 51 and 52 respectively.

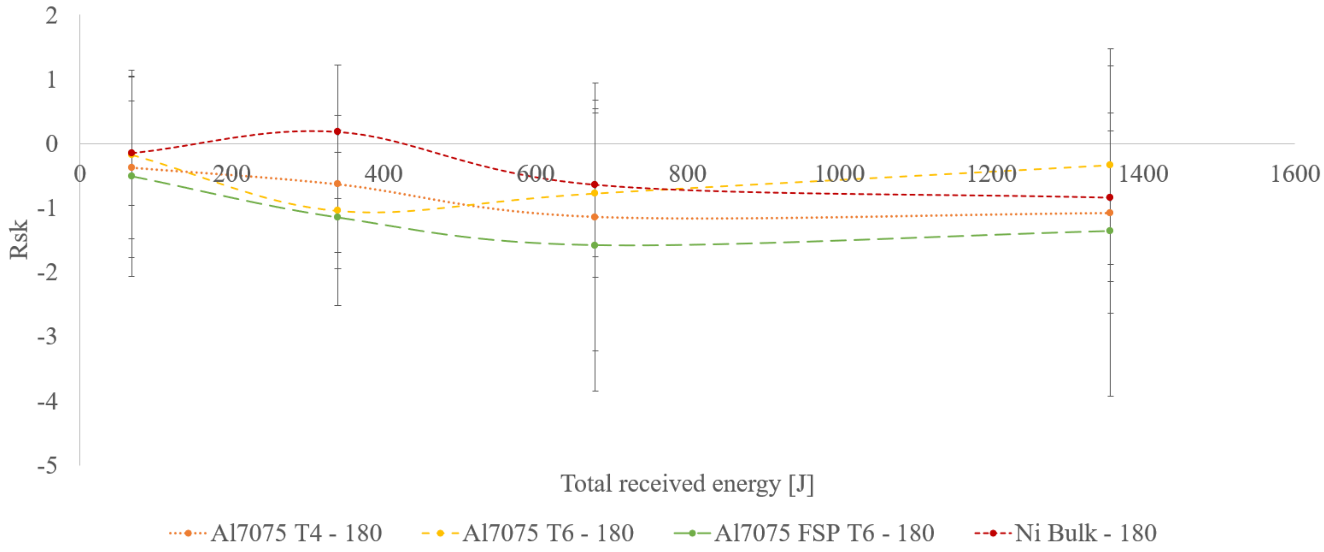

Figure 51: Evolution of the $R_{sk}$ of the Al7075 T4, Al7075 T6, Al7075 FSP T6 and Ni bulk samples as a function of the energy received, for impact speeds of 180 m/s in the PJET.

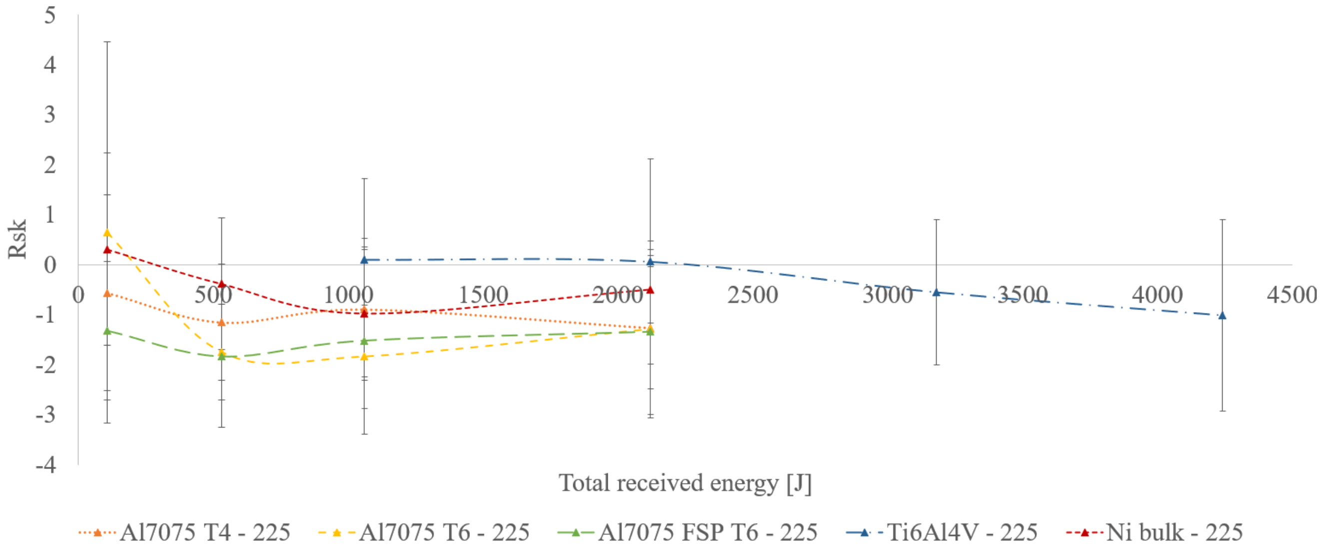

Figure 52: Evolution of the $R_{sk}$ of all five samples as a function of the energy received, for impact speeds of 225 m/s in the PJET.

As can be seen in Figure 51 for most samples, the $R_{sk}$ decreases during the early impacts then stabilizes. A similar trend can be observed in Figure 52 for the samples tested at 225 m/s, except for the Ti6Al4V sample, which starts decreasing after a higher amount of total energy received. Note that most samples have a negative skewness, $R_{sk} < 0$, which unsurprisingly indicates that the initially flat surface is dominated by cracks or valleys once erosion damage appears.

The evolution of these graphs can be understood by the fact that in the early stages of erosion, more and more pits are created while some zones are spared from erosion due to inclusions or precipitates which shield the material. As a result, during the first impacts, more and more pits are created, especially in the presence of scratches or grooves, leading to an asymmetrical surface with a majority of valleys, hence a decreasing, negative $R_{sk}$. Then, a plateau is reached, probably because the impacting droplet loses energy as it touches the hillsides of the deeper pits. As a result, the droplet does not have enough energy left to further deepen the feature, leading to a stagnating $R_{sk}$ value. The behavior of the Ti6Al4V sample, offset compared to the four other samples, may be due to the creation of pile-up around the pits. Indeed, it shows better erosion resistance, with smaller, less abundant pits. The initial erosion stages create slight pile-up around the pits, which is sheared off by the subsequent impacts and lateral jetting. As a result, the $R_{sk}$ value is initially close to 0, then decreases after a larger total received energy.

Let's now compare the evolution of the $R_{ku}$ and $R_{sk}$ to understand the difference in terms of erosion mechanisms at both impacting speeds.

For impingement speeds of 180 m/s, as the number of impacts increases, the $R_{ku}$ increases while the $R_{sk}$ decreases, as shown in Figures 49 and 51. This confirms the fact that in the early stages of erosion, shallow pits are nucleated, due to the lower impact energy. Then, the stress induced by the subsequent impacts is localized in these pits, which deepens them without significantly widening them, resulting in deeper and sharper features. This could explain why the $R_{ku}$ increases while the $R_{sk}$ decreases.

On the other hand, for impingement speeds of 225 m/s, both $R_{ku}$ and $R_{sk}$ decrease until a plateau, as illustrated in Figures 50 and 52. Indeed, due to the larger kinetic energy, the early impacts create deeper and sharper craters compared to the 180 m/s droplets. This explains the initially high $R_{ku}$ and the $R_{sk}$ quickly dropping to low values in the early stages of erosion. Then, as the number of impacts increases, the subsequent droplets smooth out and even out the surface, leading to a steady $R_{sk}$ and to a decreasing sharpness of the features, hence a decreasing $R_{ku}$.

A schematic representation of the possible erosion mechanism is illustrated in Figure 53, for the evolution of $R_{sk}$ and $R_{ku}$ described above. Note that in Figure 53, a damage localization point is already present, which can correspond to grooves created during the polishing or to defect-nucleated pits.

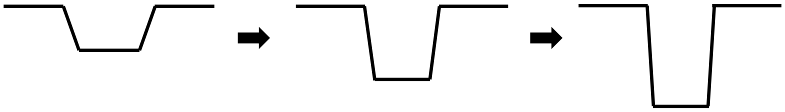

(a) Decreasing $R_{sk}$ and increasing $R_{ku}$

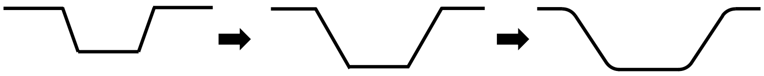

(b) Decreasing $R_{sk}$ and decreasing $R_{ku}$

Figure 53: Schematic representation of the possible erosion mechanisms undergone depending on the droplet velocity. Sub-figure (a) shows a decreasing $R_{sk}$ and an increasing $R_{ku}$, which corresponds more closely to lower energy impacts. Sub-figure (b) illustrates a decreasing $R_{sk}$ combined with a decreasing $R_{ku}$, which seems to be the topographic evolution at higher speed impacts.

In order to have a better understanding of the roughness parameters discussed above, Figure 54 shows four profiles, which highlight in a representative way the topography.

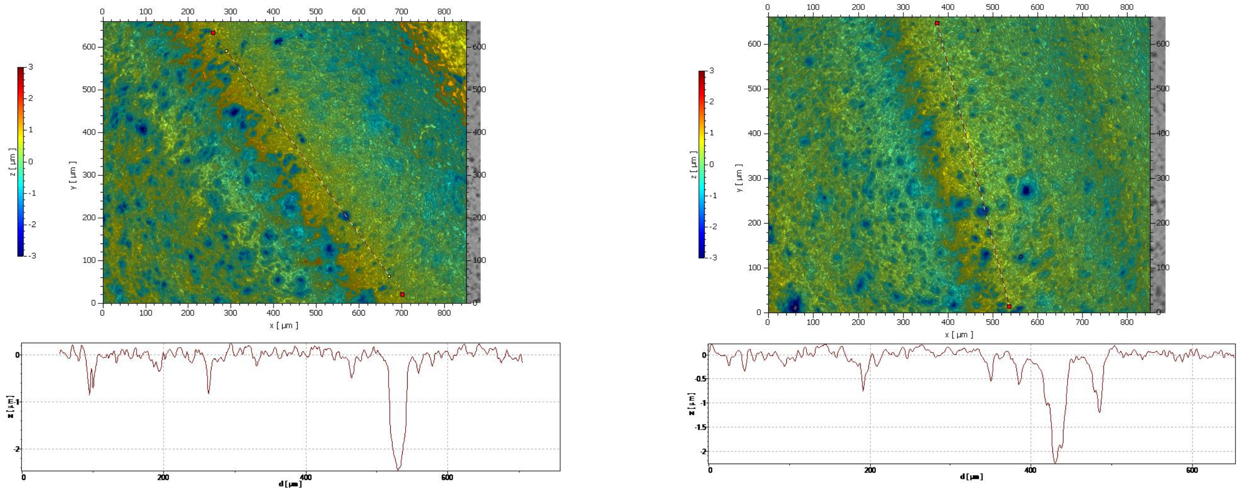

(a) Al7075 T4 - Zone C

(b) Al7075 T6 - Zone C

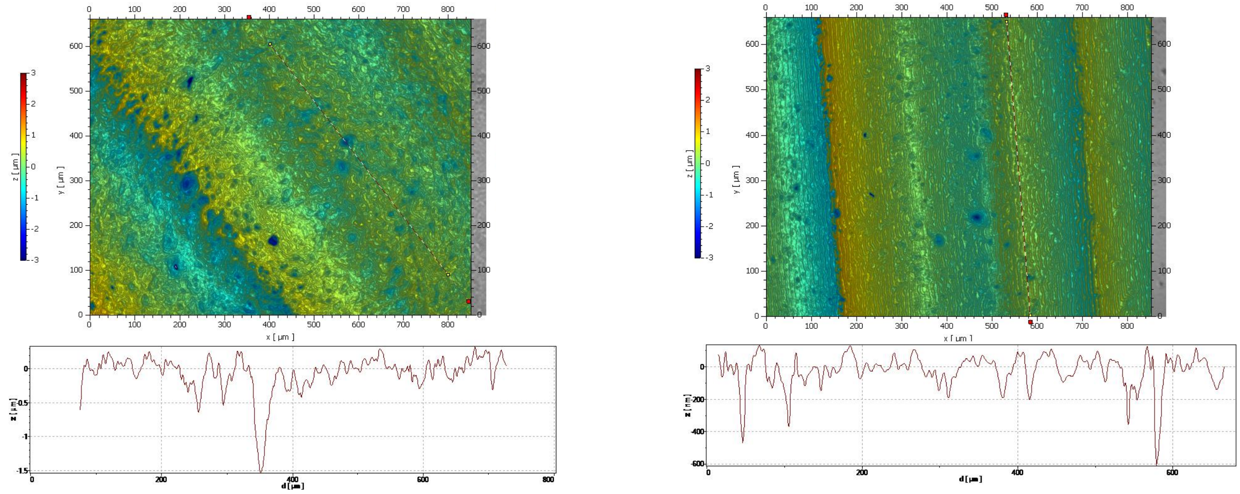

(c) Ni bulk - Zone C

(d) Ti6Al4V - Zone F

Figure 54: Profiles of the PJET-eroded samples, showing representative topography features for samples (a) Al7075 T4 (b) Al7075 T6 (c) Ni bulk and (c) Ti6Al4V. As a reminder, zone C corresponds to a total energy received of 1 060 J due to the 10 000 impacts at 225 m/s. Note that for the Ti6Al4V sample, zone F was chosen as representative profile as it displays a higher resistance to WDE. As a result, a higher total energy received is required to reach significant topographic features. Let's remind that zone F corresponds to 40 000 impacts at 225 m/s, corresponding to a total received energy of 4 240 J.

## 4.2 Comparison between PJET and WARER

### 4.2.1 Correlation between PJET and WARER

In order to compare both testing methods, one could simply correlate the number of impacts per unit surface. Indeed, as long as the materials have time to relax the stress between two consecutive impacts - which is the case for metals, both methods have similar stress-loading mechanisms despite the difference in rate of impact.

On one hand, the PJET allows to control precisely the number of impacts and the eroded zone is approximately circular with a diameter 1.5 mm, slightly smaller than the size of the impacting droplet. As a result, the surface eroded measures around 1.77 mm$^{\mathbf{2}}$.

On the other hand, the WARER has an impact rate of 144 375 impacts/h for each of the samples mounted. These droplets impact a total area of 615.75 mm$^{\mathbf{2}}$, which correspond to the exposed disk of 28 mm diameter.

As a result, if the number of impacts per unit area is equated between both WDE techniques, a correlation can be found between the number of impacts of the PJET and the exposure time of the WARER. One finds that 10 000 impacts in the PJET correspond to around 24 hours of erosion using the WARER.

This quick correlation should however be very carefully manipulated. Indeed, several strong assumptions were implicitly made. First of all, the erosion mechanisms are considered equivalent, which means that this correlation can only be used for similar impact velocity and in the absence of solid particles impingement. Secondly, the eroded area is not homogeneously exposed to droplet impacts. Indeed, in the case of the PJET, the eroded zone is not perfectly circular and the center of this zone is more heavily eroded than the outer radius. There is a distribution of impacts from the center to the outer radius, which probably follows a bell curve. In addition, the erosion zone is not clearly defined as it covers about a circular region of 1.5 mm diameter, therefore smaller than the size of the droplets. When it comes to the WARER, the discussion is even more critical. Indeed, as shown in the macro images in previous section, preferential erosion zones are located in the top left quarter of the sample. As a result, assuming that all the impacts are uniformly distributed over the whole erosion surface is a very strong hypothesis. Therefore, this correlation cannot be used in the present work, mainly because the PJET and the WARER tests were not performed at the same impact velocity.

Another way to correlate both erosion techniques is through the energy per impact. Since three different impact velocities were used for the PJET and the WARER, one can compute the kinetic energy of the droplet before impact and consider that this energy was transmitted to the sample. As a reminder, the kinetic energy can be computed as $\varepsilon_{tot} = \frac{4}{3}\pi r_0^3 \rho_0 \frac{v_0^2}{2}$. Therefore, the kinetic energy per droplet at 120 m/s, 180 m/s and 225 m/s are respectively 31.69 mJ, 67.86 mJ and 106.03 mJ.

Since the area undergoing WDE cannot be determined with precision, a direct comparison of the PJET and the WARER results based on the energy received per unit area is not straightforward. In order to correlate the PJET and the WARER results despite the difference in terms of sample size, a fixed point on the center of the WARER was chosen as reference. Indeed, all the samples which have undergone erosion in the WARER have an uneven distribution of water droplet impacts on their surface. Still, as they have all been tested in similar conditions, choosing a reference point on the sample should allow to correlate the results by eliminating the unknown exposure conditions. To compare the number of impacts with the PJET, a circular zone of 1.5 mm diameter in the center of the WARER sample will be considered.

To estimate the number of droplets which have impacted the center zone of the WARER samples, which is used for comparison with the PJET, assumptions need to be made. After 18 hours of exposure to erosion in the WARER, a total of 2.6 million droplets have impacted the sample. One can assume that all these droplets impact homogeneously the upper left quarter of the sample, as was clearly observed in Figure 18 on the chromium anodized Al2024 covered with an epoxy coating. Indeed, as a reminder, only the upper left quarter of the sample was visibly eroded, which confirms the uneven distribution of droplets over the entire sample area. Therefore, if one assumes that the 2.6 million droplets impact only a fourth of the sample, the droplet density is around 17 000 droplets/mm$^2$. As a result, on a surface equivalent to the PJET eroded zone, the number of impacts is 30 000. Since the impact velocity is 120 m/s, at which speed the droplets have a kinetic energy of 31.69 mJ, the total energy received on a region equivalent to the PJET is around 1 000 J for a sample eroded during 18 hours in the WARER.

Note that a similar reasoning for an exposure of 12 hours in the WARER gives that the total energy received by the sample on a region equivalent to the PJET erosion zones is about 670 J. This is used for the Ni bulk sample, which was eroded in the WARER for 12 hours, rather than 18 hours.

Let's examine this correlation and graphically compare the measurements of the roughness parameters for both erosion techniques.

Figure 55 compares the values of the arithmetic mean roughness parameter $R_a$ measured by laser interferometry for each material after 18 hours of exposure in the WARER with the $R_a$ of the samples eroded with the PJET. Figures 56 and 57 exhibit the same comparison for the roughness parameters $R_{ku}$ and $R_{sk}$ respectively. Note that the value of the parameters for the WARER eroded samples are represented as a red dot, located at a total energy received of 1 000 J, which corresponds to the correlation computed, except for the Ni bulk sample which is at 670 J.

Several comments can be made about these figures. The evolution of the $R_a$ parameter as a function of the total received energy for the PJET samples, displayed in Figure 55, is similar regardless of the impact speed. Indeed, both curves, measured for PJET impact speeds of 180 m/s or 225 m/s superimpose when expressed in terms of total energy received. In addition, except for the Ni bulk sample, the prediction of equivalent energy received computed for the WARER samples seems accurate. The measure of the $R_a$ parameter of the WARER samples falls in every other material almost perfectly on the PJET curves. This confirms the correlation between the exposure duration in the WARER and the total energy received in the PJET.

Regarding the $R_{ku}$ parameter, exhibited in Figure 56, the correlation found between the WARER and the PJET seems accurate for every material. As already mentioned, the evolution of the $R_{ku}$ of the PJET samples has a decreasing trend at 225 m/s while it has an increasing trend at 180 m/s. Still, both values converge at sufficiently high total energy received. The $R_{ku}$ of the WARER samples, located at the computed equivalent energy received, are in good agreement with the PJET curves.

When it comes to the skewness parameter $R_{sk}$, the fit between PJET and WARER is not as perfect, although still good. Indeed, the $R_{sk}$ value obtained for the WARER samples is over-estimated in absolute value for the Al7075 T4 and Al7075 FSP T6 samples. Still, every sample shows decent match between the WARER measurement and the PJET curves. The over-estimated $R_{sk}$ can be explained by the solid-particle impacts occurring in the WARER which cause deep, neat indents. Indeed, these indents bring the $R_{sk}$ down to more negative values as they preferentially create troughs.

All three roughness parameters, namely $R_a$, $R_{ku}$ and $R_{sk}$, seem to confirm the correlation between 18

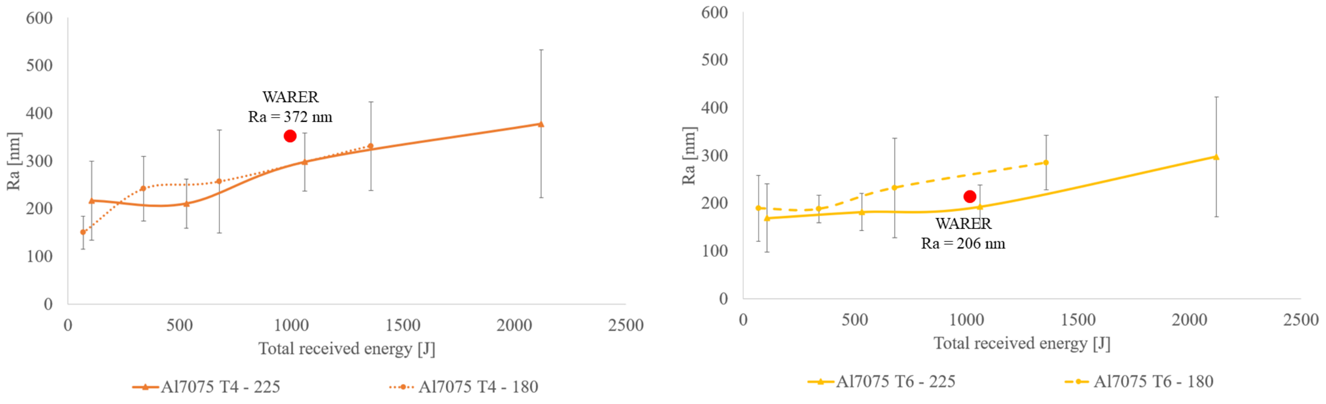

(a) Al7075 T4

(b) Al7075 T6

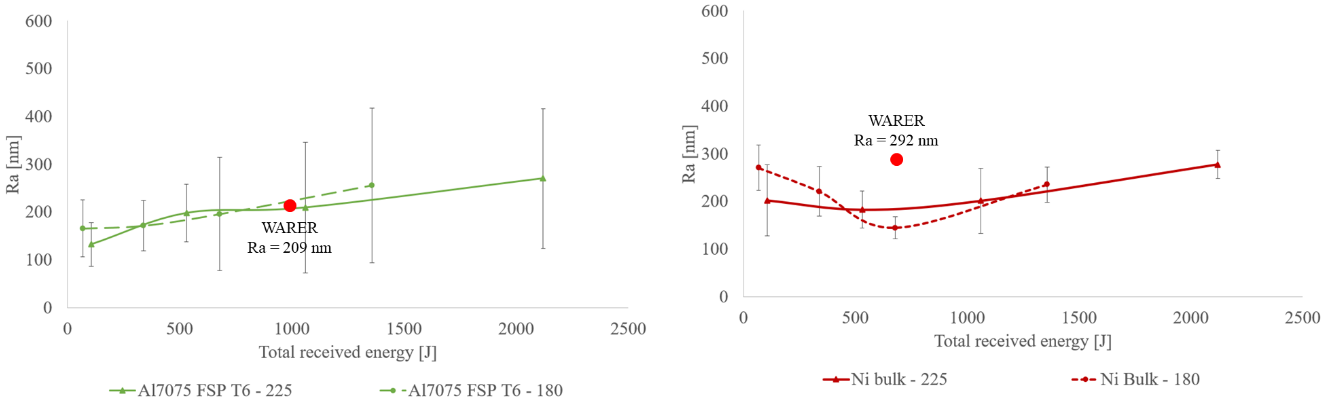

(c) Al7075 FSP T6

(d) Ni bulk

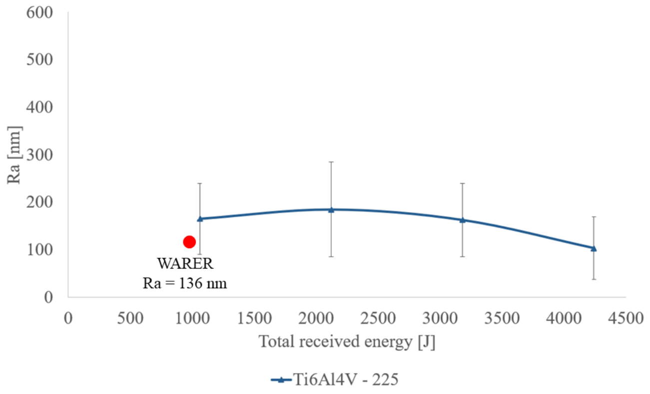

(e) Ti6Al4V

Figure 55: Comparison of $R_a$ values of the PJET and the WARER eroded samples for samples (a) Al7075 T4 (b) Al7075 T6 (c) Al7075 FSP T6 (d) Ni bulk and (e) Ti6Al4V. Note that the values obtained for impacts at 180 m/s and 225 m/s are drawn with dotted and solid lines respectively. The $R_a$ values of the WARER eroded samples are represented as a red dot.

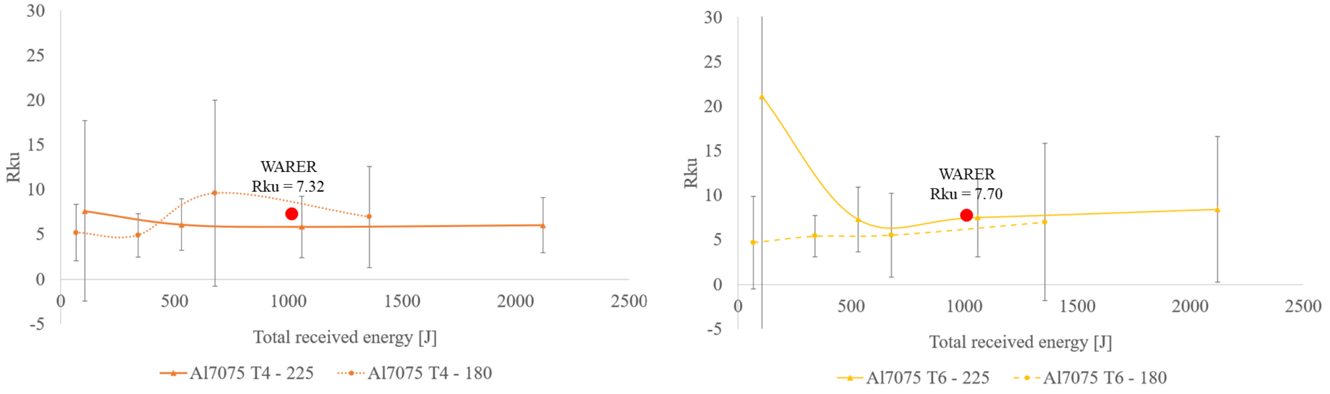

(a) Al7075 T4

(b) Al7075 T6

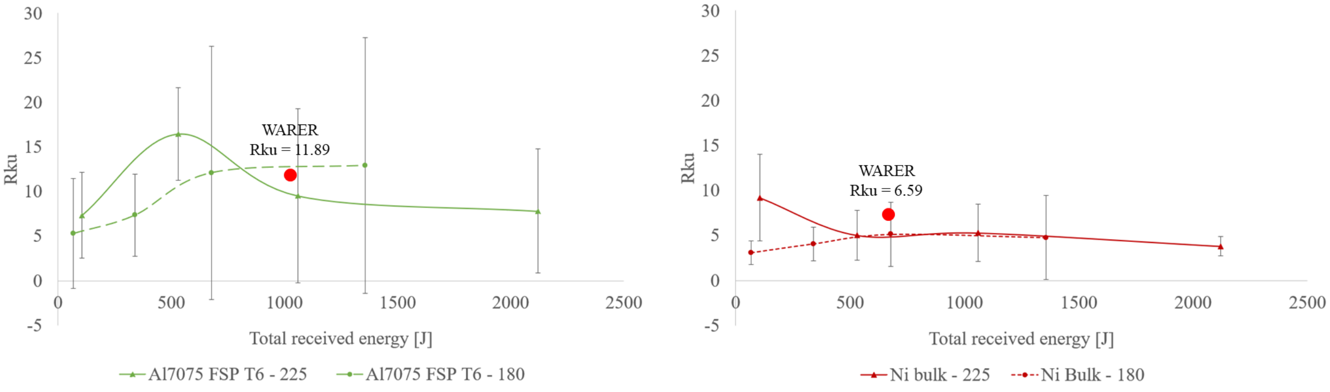

(c) Al7075 FSP T6

(d) Ni bulk

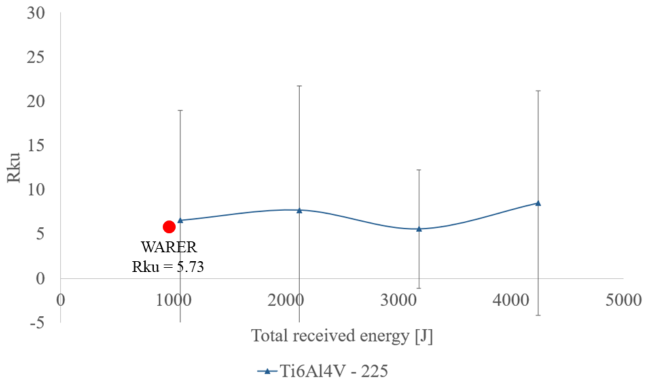

(e) Ti6Al4V

Figure 56: Comparison of $R_{ku}$ values of the PJET and the WARER eroded samples for samples (a) Al7075 T4 (b) Al7075 T6 (c) Al7075 FSP T6 (d) Ni bulk and (e) Ti6Al4V. Note that the values obtained for impacts at 180 m/s and 225 m/s are drawn with dotted and solid lines respectively. The $R_{ku}$ values of the WARER eroded samples are represented as a red dot.

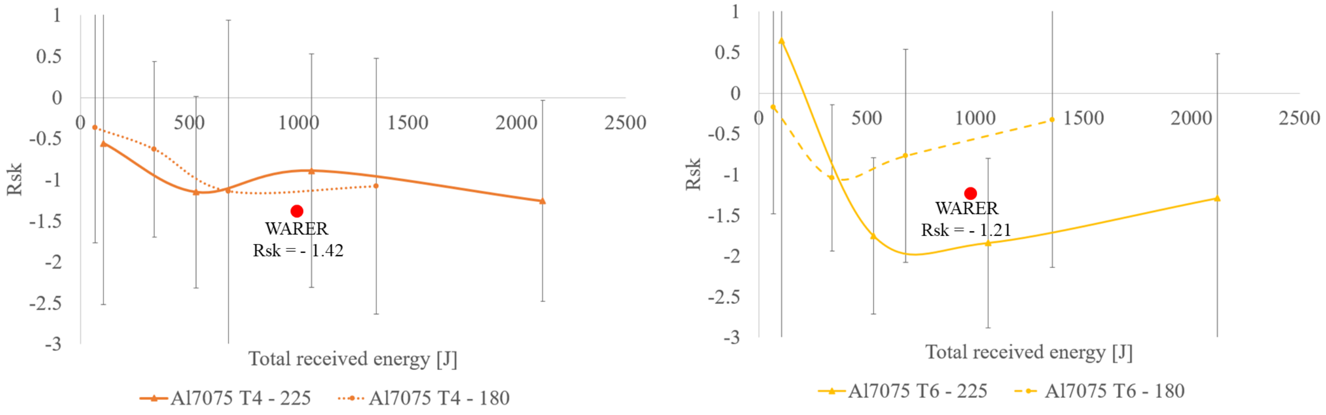

(a) Al7075 T4

(b) Al7075 T6

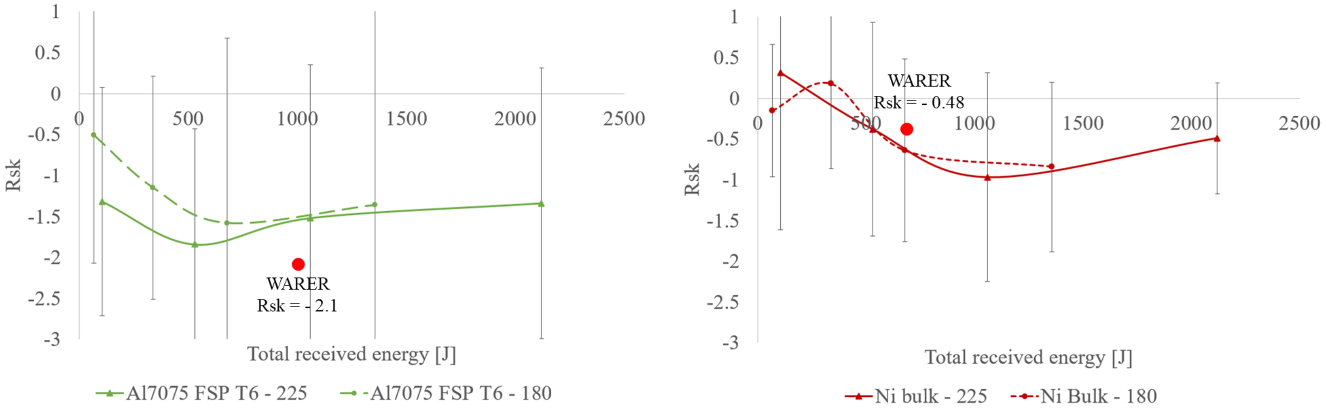

(c) Al7075 FSP T6

(d) Ni bulk

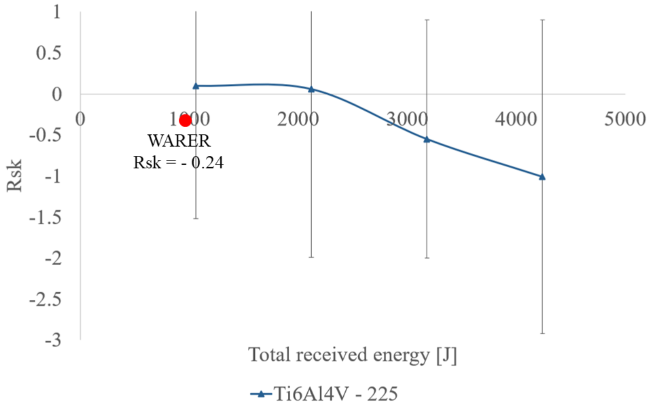

(e) Ti6Al4V

Figure 57: Comparison of $R_{sk}$ values of the PJET and the WARER eroded samples for samples (a) Al7075 T4 (b) Al7075 T6 (c) Al7075 FSP T6 (d) Ni bulk and (e) Ti6Al4V. Note that the values obtained for impacts at 180 m/s and 225 m/s are drawn with dotted and solid lines respectively. The $R_{sk}$ values of the WARER eroded samples are represented as a red dot.

hours of exposure in the WARER at 120 m/s impacts and a total energy received of 1 000 J in the PJET. This corresponds to around 15 000 impacts at 180 m/s or 9 000 impacts at 225 m/s in the PJET. Still, some comments need to be made on the correlation:

- Although the erosion mechanisms are globally similar, as shown in a previous section, there are fundamental differences between both techniques. Indeed, in the WARER, larger droplets can periodically be formed, leading to sudden more severe damage. In addition, dust particles can also cause solid-particle impingement and induce a different topography, characterized by sharp scratches.
- There is also a significant difference in terms of individual droplet energy between impacts at 120 m/s and at 225 m/s. The kinetic energy of the droplets is more than tripled between both speeds, which means that the erosion mechanisms will also differ.
- The arithmetic mean roughness $R_a$ is a very common and useful parameter, but does not take the shape of the topographic features into consideration. As a result, it serves as a comparison parameter but hides much of the topographic information.
- Although the skewness $R_{sk}$ is the roughness parameter which should give the closest insight to the erosion profile, it does not show an as good correlation between the PJET and WARER techniques as the $R_a$ and $R_{ku}$.
- In order to have a more representative correlation, one could map out a larger area on the WARER sample, to even out local defects due to WARER-specific damage mechanisms. Similarly, averaging several roughness measurements on the PJET eroded zone would give a better comparison basis and allow to narrow down the standard deviation.
- Finally, the surface roughness assessment technique used, namely laser interferometry which is based on a Michelson interferometer, may not be the best suited due to fringes appearing for low roughness profiles. Working at more advanced erosion stages would limit this problem. Another solution is to try using another technique, such as chromatic confocal laser scanning microscopy (CLSM) for example, which determines the profile with a continuum of monochromatic beams individually interpreted by a spectrometer.

These limitations show that one must keep a critical mind when it comes to correlating different techniques with very different erosion conditions and operating parameters.

### 4.2.2 Material specific comparison

In this section, the results of each material using both PJET and WARER techniques will be discussed based on the comparison of the performance analyzed above.

One should also look back to the applications where resistance against WDE is critical, mainly wind turbines and planes leading edges. Indeed, in these applications, resistance to WDE is not the only factor influencing the choice of material. In addition, the solution must resist corrosion. This is a reason why currently the protections are Al2024 anodized alloys cladded with pure aluminum which shows good corrosion resistance. On top of corrosion resistance, the solution must also have low weight, good impact resistance to withstand birdstrikes for example and decent mechanical properties, such as toughness, fatigue resistance,...

**Al7075**

As can be seen in Figure 57, the three Al7075 samples have different behaviors when it comes to the PJET and WARER results comparison. Despite similar exposure conditions, the correlation between the WARER and the PJET does not match perfectly for all three samples. Indeed, as can be seen in Figures 57b and 57c, both Al7075 T6 and Al7075 FSP T6 samples eroded with the PJET seem to converge toward a similar value of $R_{sk}$ of -1.5. On the other hand, when eroded with the WARER, these sample show a broader difference in terms of $R_{sk}$.

In addition, one should notice that the value of $R_{sk}$ decreases in absolute value from the Al7075 T4 to the Al7075 T6 WARER samples, from -1.42 to -1.21. This is in accordance with the observations: the harder Al7075 T6 sample has better resistance to WDE. What is more surprising is that the Al7075 FSP T6 WARER sample has a poorer behavior, based on the laser interferometry roughness measurements, since it has a much higher $R_{sk}$ in absolute value, namely -2.1. This does not match the ranking made based on the PJET results, which positions the Al7075 T6 and Al7075 FSP T6 on a similar performance level. This incoherence may be explained by solid-particles impingement which is a more random damage mechanism happening in the WARER samples. Indeed, in all three cases, the solid-particle impingement lead to sharp, deep and localized features, explaining locally a low value of $R_{sk}$ and a high value of $R_{ku}$. Since this is an uncontrolled process, it can appear randomly in some samples while less significantly in others, explaining a slight discrepancy in the WARER results.

Several solutions can be examined to limit this appearance of solid-particles impingement. As it is a random process, testing several samples should even out the distribution of such sharp impacts on the surface and lead to a more statistically relevant comparison. Another possibility is to test the materials in pairs as the WARER has two samples holder. Indeed, the samples Al7075 T4 and Al7075 T6 were tested simultaneously in the WARER and therefore experienced exactly the same level of dust and particles in their exposure to erosion. Since the WARER Al7075 FSP T6 sample was tested separately from the other two aluminum samples, it may have undergone more severe solid-particle impingement, explaining the lower $R_{sk}$ value. Finally, a heavy change in infrastructure in the WARER chamber could help ensure the room is perfectly clean for each test and would be a first step towards more repeatable tests.

Finally, one should notice that the PJET results, therefore with repeatable conditions, give a coherent ranking of the three Al7075 samples. The Al7075 T4 sample, which has a lower hardness erodes more significantly but still with the same erosion mechanisms as the other two. Both Al7075 T6 and Al7075 FSP T6 samples have similar, higher yield strength (540-550 MPa) as it is dictated by the heat treatment. Despite the improved ductility brought by the friction stir processing, they both perform similarly in terms of resistance to WDE. The absence of influence of the ductility is probably explained by the fact that the tests performed remained in the early stages of erosion, where no significant loss of matter is observed. For future work, pushing the erosion further for those two samples would bring interesting insight in the influence of the friction stir processing in the advanced damage mechanisms, through an improved ductility.

Still, none of these three materials seems to be perfectly suited for leading edge protection. Indeed, the Al7075 T4 sample is an intermediate step between the solution treatment and the T6 sample. Therefore, it is not a metastable state, which will change properties upon longer natural aging and does not have high impact resistance. The Al7075 T6 is not a much better solution as it has poor corrosion resistance, as could be observed in the WARER samples, which displayed heavy oxidation from the early stages of exposure to water. When it comes to the Al7075 FSP T6, it improves the ductility but is difficult to extend to non-planar structures, such as leading edges. Indeed, it would require first proceeding to the FSP treatment on a flat sheet, then forming it. During the shaping operation, which would require a solution treatment, the mechanical properties will inevitably be altered, possibly leading to abnormal grain growth, as shown by Lezaack et al. [47] In addition, the Al7075 series are known to be hardly weldable by conventional fusion techniques, which is a limitation for industrial applications. Indeed, they are susceptible to induce hot cracking and therefore require more advanced welding techniques such as friction stir welding.

### Ti6Al4V

When it comes to the Ti6Al4V sample, unsurprisingly, it has excellent erosion performances thanks to the higher strength and higher Young's modulus. The weak point of Ti6Al4V seems to be the interface between both phases $\alpha$ and $\beta$. Indeed, the first isolated pits observed as damage initiation mechanisms seem to be nucleated at the interfaces. In addition, at the macro-scale, the soft peening damage observed may also be explained by this dual phase nature. Indeed, the $\alpha$ phase seems to have a lower strength than the $\beta$ phase and therefore collapses upon the early stages of erosion, leading to wide but shallow valleys.

As for the other samples, the solid-particles impacts happening during the WARER erosion create deep and narrow scratches. As a result, the value of $R_{ku}$, representing the sharpness of the features, is probably overestimated. The asymmetry of the profile, represented by $R_{sk}$, is probably also altered as its absolute value is larger than what it would be if no solid-impingement was present.

From an industrialization point of view, Ti6Al4V is probably not a viable solution as it is highly expensive, even for the aeronautic industry. In addition, it has low impact resistance and can only be shaped at very high temperature, under superplastic forming. There is also a risk of galvanic corrosion with aluminum parts, typically the structural parts of airplanes wings. Still, research is made in carbon fiber reinforced polymers sandwiched in titanium alloys sheets. This type of leading edges, which would allow high resistance to erosion and low weight, is under development.

### Ni bulk

The behavior of the Ni bulk samples eroded both in the PJET and the WARER is harder to interpret as it shows less distinct trends. Still, as for the other samples, the two-scales erosion mechanisms can be observed. Due to its low yield strength but high ultimate tensile strength, bulk nickel undergoes significant plastic deformation, visible mostly at the macro-scale in the form of peening. The micro-scale form of erosion, namely distributed pitting, is probably nucleated at the grain boundaries as they randomly appear at distances of about 20-50 µm, corresponding to the order of magnitude of the grains size.

From an application point of view, Ni could be used as surface deposit. In that case, the problem of decohesion with the substrate becomes a major cause of failure, as often encountered in the literature. The poor adhesion of nickel on composites, main material used in wings or blades, is a critical failure mechanism. The problem of coating decohesion of electroplated nickel is discussed in the following section.

## 4.3 Erosion of coated samples

All five samples tested in the previous subsections were made of a single material. The reason for this was to assess the resistance to water droplet erosion with no influence of other external parameters. Indeed, samples consisting of a coated substrate have a different behavior dictated by the coating thickness. This was tested in the present work, using the electroplated nickel samples introduced earlier. The choice for electroplated nickel was made because of the known high hardness of this type of coating. Indeed, the electrodeposition of nickel leads to much smaller grain size than the annealed bulk nickel sample tested previously. As the main strengthening phenomenon in nickel is grain boundary strengthening, the Hall-Petch relationship predicts that electroplated nickel has a much higher strength than annealed bulk nickel due to the significantly smaller grain size.

For that reason, the preliminary test performed on the three different electroplated nickel samples was a Vickers micro-hardness test. Table 8 shows the average value of the hardness measured, based on 10 indents performed at distinct locations, using a weight of 300 g for a duration of 10 seconds (HV0.3).

| Sample | Deposition duration | Hardness | Standard deviation |
|---|---|---|---|
| Ni ED 1 | 120 min | 547.8 HV | 9.61 |
| Ni ED 2 | 135 min | 540.6 HV | 4.43 |
| Ni ED 3 | 135 min | 549.0 HV | 5.66 |

Table 8: HV0.3 micro-hardness measurement of the three electroplated nickel samples.

From the average hardness summarized in Table 8, the ultimate tensile strength of the three samples can be estimated between 1 775 and 1 800 MPa, significantly higher than the bulk nickel used in the previous tests. As a reminder, the Ni bulk samples had a Vickers hardness of around 102 HV, corresponding to a tensile strength around 330 MPa. This confirms that the electroplating process allows a much higher surface hardness. Wasekar et al. [46] showed, based on Hall-Petch relation between the strength and the grain size, that such hardness corresponds to grains of the order of 20 nm, hence nano-crytalline electroplated nickel.

One should note that annealed bulk nickel and electroplated nickel have radically opposite behaviors. On one hand, annealed bulk nickel shows a low yield strength but thanks to high strain hardening, the ductility is remarkable. On the other hand, electroplated nickel has much higher strength but displays a much more brittle behavior, due to the poor ductility.

Despite the attention paid during the electroplating, the samples showed slight pitting on the outer ring, probably due to gas bubbles entrapment or to local defects on the copper substrate surface. Since samples 2 and 3 had similar electroplating conditions for comparable hardness, they were tested simultaneously in the WARER. Sample Ni ED 1 was not tested due to the shorter deposition duration, leading to a thinner coating in which the influence of the copper substrate is more significant.

After 2 hours of erosion, the samples Ni ED 2 and Ni ED 3 already showed early signs of pitting. After an additional 3 hours of exposure to erosion, both samples had failed and experienced serious material loss. This can be observed in Figures 58a and 58b which show macro pictures of samples Ni ED 2 and Ni ED 3 respectively after 5h of exposure in the WARER at standard conditions.

(a) Ni ED 2

(b) Ni ED 3

Figure 58: Macro images of samples Ni ED 2 and Ni ED 3, after 5h of test in the WARER at standard conditions.

Both samples experienced similar failure mode, which is due to decohesion of the electrodeposited coating. Observation of these samples in optical microscopy using bright field shows clear cracks starting from the zones of pitting initiation and propagating further on the nickel coating. Despite the fact that the sample Ni ED 2 has reached an advanced stage of erosion with significant material loss, it is interesting to observe it under an optical microscope as several stages of the erosion mechanism can be highlighted. This is illustrated in Figure 59.

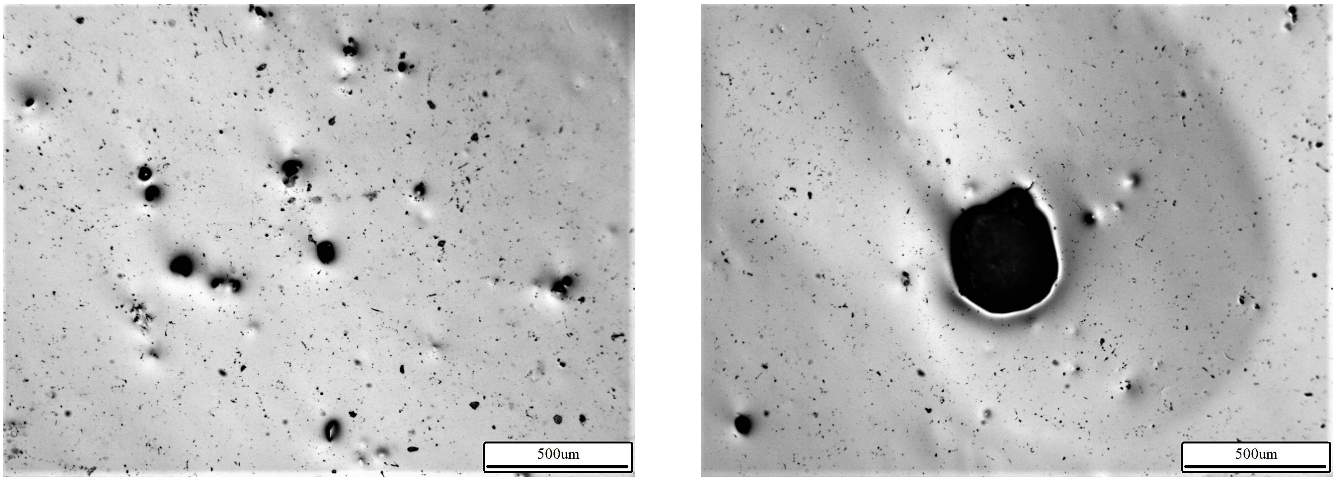

(a) Zone 1

(b) Zone 2

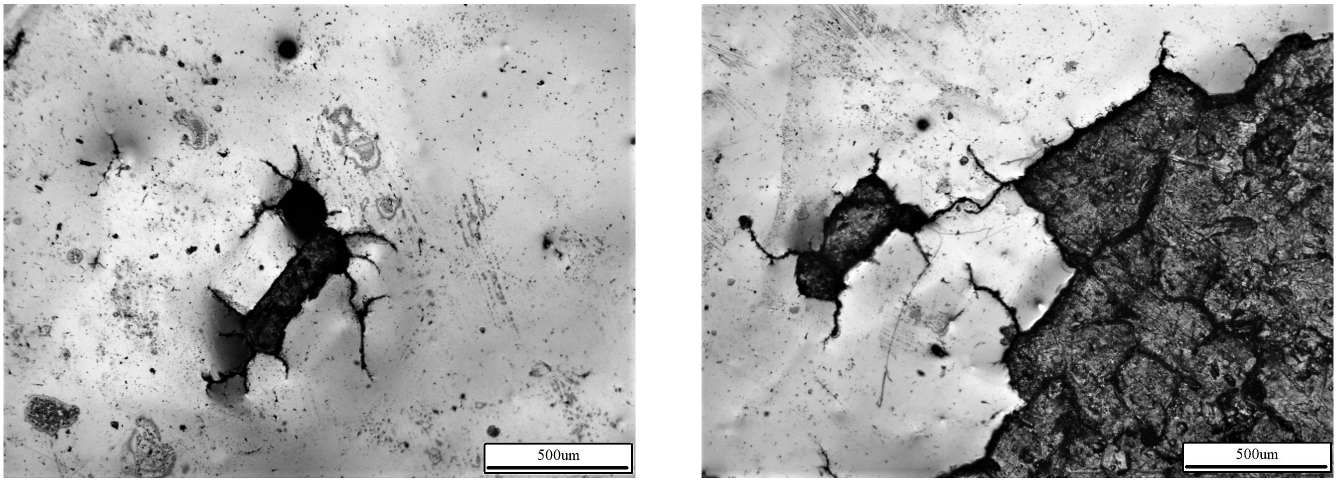

(c) Zone 3

(d) Zone 4

Figure 59: Bright field optical microscopy images of the delaminated Ni ED 2 sample. The nickel coating appears bright while the copper substrate is the dark background. The zones observed, named from 1 to 4, correspond to the zones highlighted in Figure 58a.

The images in Figure 59 were taken on four different zones of the Ni ED 2 sample, illustrated in Figure 58a as zones 1, 2, 3 and 4. Each zone represents a different stage of the erosion mechanism :

- Figure 59a shows points of pitting initiation. These points are probably defects which appeared during the electroplating in the form of gas bubbles. A bridge may have been made by the nickel over the copper substrate with poor contact, creating a weak spot. Another hypothesis is that these pitting initiations were created by impacts with solid particles. Indeed, such particles can mark the electroplated nickel with a sharp defect, which is then dug by water erosion.
- Figure 59b shows a pit which has grown due to the water droplet impacts. This image clearly shows that water engulfed in the pit and spread between the coating and the substrate, as a circular decohesion zone can be seen around the pit. This phenomenon is similar to the one shown in Figure 59a but at a more advanced stage. One should note the initiation of a crack on the upper right part of the hole.
- Figure 59c shows a subsequent stage of the damage, in the continuity with the previous image. The

cracks initiated in the previous step have grown and spread mostly in a radial direction. Here, the relatively low ductility and fracture toughness of electroplated nickel are clearly illustrated.

- The final damage mechanism is illustrated by Figure 59d. Due to the merging of the cracks, entire coating panels have been isolated and detached from the substrate by the high speed lateral water jetting. This final stage leads to a severe loss of material.

It is interesting to note that the hardness of the Ni ED samples did not significantly increase in the zones impacted by the liquid droplets but which have not undergone decohesion or failure. For example, a measure of the hardness following the same procedure as previously on the bottom part of the Ni ED 2 sample gave 547.7 Hv, similar to the initial 540 Hv. This confirms that hard electroplated nickel does not allow much work hardening under the liquid impingement conditions of the WARER, as was shown by Wasekar et al. [46]

Both Ni ED samples showed the importance and influence of the adhesion to the substrate for coatings. This is crucial for aerospace and wind power applications, where leading edge protection solutions generally include a coating. Indeed, despite the much higher hardness of the coating compared to the Ni bulk sample, the resistance to WDE is much poorer. One would prefer using a tougher and more ductile material, which loses less matter than a harder but brittle coating which detaches from the substrate.

In the case of coatings, two aspects must be closely monitored: the presence of initial pitting or damage initiation zones and the adhesion with the substrate. On one hand, the coatings must have excellent initial surface condition because as soon as a pitting initiation zone is present, as illustrated in Figure 59, the damage will propagate and lead to complete, catastrophic delamination of the coating. On the other hand, to improve the adhesion with the substrate, the coating thickness as well as the compatibility in terms of strain release rate must be closely studied. To avoid such problems, a primer can be of great use, as it serves as intermediate between the substrate and the coating. A well chosen primer leads to a better compatibility of both layers, ensuring better adhesion.

# 5 Towards a material performance index

## 5.1 Pressure rise

Let's now examine the correlation between the material properties and the resistance to WDE. For this comparison, instead of using the material properties found in the results section, which fluctuate significantly due to the experimental characterization techniques, ideal material properties are used, based on the values found in the literature. [47] [48] [55] [63] The parameters used are summarized in Table 9.

| **Material** | **Al7075 T4** | **Al7075 T6** | **Al7075 FSP T6** | **Ti6Al4V** | **Ni bulk** |
|---|---|---|---|---|---|
| Yield strength - $\sigma_y$ [MPa] | 450 | 540 | 550 | 900 | 300 |
| Young's modulus - $E$ [GPa] | 72 | 72 | 72 | 114 | 200 |
| Density - $\rho_s$ [kg/m$^3$] | 2 800 | 2 800 | 2 800 | 4 500 | 8 900 |
| Speed of sound - $c_s$ [m/s] | 6 350 | 6350 | 6350 | 4950 | 4 900 |

Table 9: Ideal material properties, used for comparison of material performance indices.

Before looking at actual performance indices, let's look at the pressure rise in the material, based on the review of literature section. The parameters of the equations are the droplet density $\rho_0 = 1\ 000$ kg/m$^3$, the speed of sound in water $c_0 = 1\ 500$ m/s and the impact velocity $v_0$ which, in the experiments of the present work, was 120 m/s, 180 m/s or 225 m/s. The four models predicting the pressure rise which are discussed further are reminded below.

$$\varDelta P_{w-h} = \rho_0 c_0 v_0 \tag{1}$$

$$\varDelta P_{Heymann} = \rho_0 c_0 v_0 \left[1 + kM_0\right] \tag{2}$$

$$\varDelta P_{mw-h} = \frac{\rho_0 c_0 \rho_s c_s v_0}{\rho_0 c_0 + \rho_s c_s} \tag{3}$$

$$\varDelta P_{sg} = \rho_0 c_0 v_0 \left[\frac{(\gamma+1)M_0}{4} + \sqrt{1 + \frac{(\gamma+1)^2 M_0^2}{16}}\right] \tag{4}$$

According to equation (1), the water-hammer pressure rises in the material for impacts at 120 m/s, 180 m/s and 225 m/s are respectively 180 MPa, 270 MPa and 338 MPa. When it comes to the water-hammer pressure corrected by Heymann, found in equation (2), it predicts pressures of 209 MPa, 335 MPa and 439 MPa. Based on the stiffened-gas pressure rise, defined in equation (4), the pressure rise is 200 MPa, 317 MPa and 413 MPa for impacts at 120 m/s, 180 m/s and 225 m/s respectively. The pressure rise predicted by these three models are summarized in Table 10.

| | **120 m/s** | **180 m/s** | **225 m/s** |
|---|---|---|---|
| $\varDelta P_{w-h}$ [MPa] | 180 | 270 | 338 |
| $\varDelta P_{Heymann}$ [MPa] | 209 | 335 | 439 |
| $\varDelta P_{sg}$ [MPa] | 200 | 317 | 413 |

Table 10: Comparison of the pressure rise in the impinged material predicted by the water-hammer model $\varDelta P_{w-h}$, by Heymann $\varDelta P_{Heymann}$ and by the stiffened-gas model $\varDelta P_{sg}$ for impact speeds of 120 m/s, 180 m/s and 225 m/s. Note that the pressure rise predicted by these models do not consider material properties and are therefore similar regardless of the target impinged.

These results can be compared to the modified water-hammer pressure, as defined in equation (3), which is specific for each class of material as it depends on the properties of the impinged material. Table 11 compares the pressure rise for the Al7075 series, the Ti6Al4V and the Ni bulk materials for the three impacting speeds.

| $\Delta P_{mw-h}$ [MPa] | **120 m/s** | **180 m/s** | **225 m/s** |
|---|---|---|---|
| Al7075 series | 166 | 249 | 311 |
| Ti6Al4V | 169 | 253 | 316 |
| Ni bulk | 174 | 261 | 326 |

Table 11: Comparison of the modified water-hammer pressure $\Delta P_{mw-h}$ of the three categories of materials studied, namely Al7075 series, Ti6Al4V and Ni bulk, for impact speeds of 120 m/s, 180 m/s and 225 m/s.

Note that the maximum pressure predicted by the stiffened-gas model is below the yield strength of each material, except for the Ni bulk sample. A naive interpretation would lead to the conclusion that the materials should not show plastic deformation upon impacts at these speeds. The experiments performed in the present work clearly show the opposite. This is due to several factors, such as the local stress concentration upon impingement due to the surface topography. On the other hand, the materials are intrinsically not uniform and therefore experience local weaker points. Weaker points can be linked to grain boundaries or to a weaker phase as in biphasic materials such as Ti6Al4V. Performing a fine mapping of the surface hardness by nano-indentation on the samples would allow to confirm this hypothesis. This indicates that the tensile strength, or equivalently the hardness, alone is not a sufficient performance index.

## 5.2 Comparison of material performance indices

In order to rank the different samples from an erosion resistance point of view, let's focus on material performance indices, based on macroscopic properties. Since erosion is a complex phenomenon which implies several mechanical properties, such as the hardness, the tensile strength, the toughness or the ductility, a rigorous material selection method is difficult. Still, an approach similar to that developed by Michael Ashby [1] can be taken to develop a material index.

The first step is to identify the requirements of the application. In our case, the function of the material is to serve as a protecting solution against erosion caused by the impingement of water droplets at high speed. When it comes to the objective, it is more difficult to pinpoint a single one as it depends on the application. Indeed, one could want to minimize the mass loss if the focus is put on the durability; one could want to minimize the roughness evolution to conserve aerodynamic properties; one could want to minimize the weight in aerospace applications for instance. Still, in our economy-based society, most applications are subjected to the same objective: minimizing cost. Currently, in most industries, reducing costs is the only objective with, as constraint, to have a resistance to erosion enough to keep the application running during the lifetime of the application. Typically, in the airplanes industry, the objective is to find the cheapest and lightest solution possible, provided that the leading edge has a lifetime of at least 25 years. However, from a sustainable development point of view, it might be better to design more durable, possibly reusable parts.

Since the present work is more focused on the technical point of view, the objective chosen is to minimize the roughness evolution, which can be translated as minimizing the absolute value of $R_{sk}$. Indeed, based on the samples analyzed, the main damage mechanism was the pitting of the material, which translates into a negative $R_{sk}$. As long as the initial surface level can still be seen, which is the case for all the samples of the present work, this criterion is similar to minimizing the volume loss of the sample.

One should note, based on the definition of $R_{sk}$, that a material with a skewness equal to 0 only means that the profile is symmetric with respect to the mean line. As a result, past the incubation stage, when the erosion profile is much more pronounced, minimizing the absolute value of $R_{sk}$ may not be the most relevant choice. Indeed, the surface may be highly eroded, with extreme relief, but symmetrical, which would bias the assessment of the erosion due to the definition of the $R_{sk}$ parameter. Instead, minimizing weight loss, minimizing the arithmetic mean roughness $R_a$ or minimizing the maximum peak to valley distance $R_z$ would be more suitable objectives, as suggested by A. Phelps. [66]

When it comes to the constraints, the material chosen should resist to corrosion due to the frequent exposure to water. In terms of impact resistance, one would also prefer, from an application point of view, a material with high toughness for example to resist to bird strikes. The material chosen should also allow easy manufacturing or forming in order to produce leading edge protections, often in the form of long sheets to be placed on top of a structural support in wings or blades. In that context, the structure and the protecting layer need to have a good match in terms of Young's modulus and thermal expansion coefficient to prevent high internal stresses leading to warping or decohesion.

A first candidate for erosion resistance index, which was introduced in the first section of this work, is the elastic resilience $U_r$ defined as $I_1 = U_r = \frac{\sigma_y^2}{2E}$. This index $I_1$ corresponds to the elastic energy that the material can store per unit volume, expressed in [Pa] or equivalently in [J/m$^3$].

Another performance index was introduced by Heymann [67] and reported by H.S. Kirols [14]. Indeed, Heymann showed that the "normalized erosion resistance" of a series of materials, defined as the erosion rate compared to a sample with reference hardness, is proportional to $\left(\sigma_y^2 E\right)^{\frac{2}{3}}$. This observation defines the following erosion parameter: $I_2 = \sigma_y^2 E$, which is based on experimental correlations. The units of $I_2$ are therefore [Pa$^3$].

An approach similar to M. Ashby was used by Zok et al. [68] where solid-solid contacts were studied with several conditions for yielding: either plastic deformation or cracking. This is a study of the wear resistance, characterized as the change of surface topography due to unwanted removal of matter, which is a twin problem to water droplet erosion. For a blunt contact with yielding as limiting constraint, the material index developed is $I_3 = \frac{\sigma_y^3}{E^2}$. As for index $I_1$, the units of $I_3$ are [Pa]. Note that this index is based on the normal load undergone by the material upon indentation. Since no such physical relation has been developed so far for the impingement of liquid droplets, no direct translation to a material index for the resistance to WDE can be made. Still, it is interesting to compare this index with the tested samples.

One should also investigate the influence of the density of the material on the resistance to WDE. Indeed, despite its low yield strength, the Ni bulk sample shows better erosion resistance than the Al7075 alloys. This could be explained by its higher density, leading to a dynamic inertia, which could dissipate more energy during the impact. In addition, the modified water hammer pressure, illustrated in equation (3) and computed in Table 11 for each sample, illustrates that the density of the material has an influence on the maximum pressure rise. At high strain rates, as in water droplet erosion where the droplets smash the substrate at high speed, the material inertia has a significant influence on the stress response, as shown by Houqun et al. [69] and Zhang et al. [70] Since inertia is directly proportional to weight, one could define a new material index based on $I_2$ as $I_4 = \rho\sigma_y^2 E$. The units of $I_4$ are $\left[\frac{kg.Pa^3}{m^3}\right]$, which correspond in the SI units reference to $\left[\frac{kg^4}{m^6 s^6}\right]$.

The different material performance indices mentioned in this section are estimated and compared for each of the five tested materials in Table 12. The units and order of magnitude of each index are indicated in the table for reference. Still, one should not compare the absolute value of the different indices for one sample but rather rank the different samples based on one index.

| **Index** | **Units** | **Al7075 T4** | **Al7075 T6** | **Al7075 FSP T6** | **Ti6Al4V** | **Ni bulk** |
|---|---|---|---|---|---|---|
| $I_1 = \frac{\sigma_y^2}{2E}$ | $10^5$ [Pa] | 14.1 | 20.2 | 21.0 | 35.5 | 2.3 |
| $I_2 = \sigma_y^2 E$ | $10^{27}$ [Pa$^3$] | 14.5 | 20.9 | 21.8 | 92.3 | 18.0 |
| $I_3 = \frac{\sigma_y^3}{E^2}$ | $10^3$ [Pa] | 17.5 | 30.4 | 32.1 | 56.1 | 0.7 |
| $I_4 = \rho\sigma_y^2 E$ | $10^{31}$ $\left[\frac{kg.Pa^3}{m^3}\right]$ | 4.1 | 5.9 | 6.1 | 41.5 | 16.0 |

Table 12: Comparison of material performance indices assessing the resistance to WDE, using the ideal material properties summarized in Table 9.

Let's compare the material indices summarized in Table 12 with the resistance to WDE observed based on the value of the $R_{sk}$ roughness parameter. Indeed, as can be seen in Figure 52, the materials can be classified in increasing resistance to WDE as Al7075 T4, Al7075 T6, Al7075 FSP T6, Ni bulk and Ti6Al4V. Note that the three Al7075 samples have very close behavior. The only index of Table 12 which ranks the materials in the same way is $I_4$.

Index $I_1$, which is a measure of the maximum elastic energy that the material can absorb before entering plasticity, and index $I_3$, which is a measure of the resistance to plastic imprint upon impingement, are poor indicators. Indeed, although they both classify the aluminum alloys and the Ti6Al4V correctly, they greatly undervalue the resistance of the Ni bulk sample. When it comes to the $I_2$ index, developed experimentally by Heymann, it places the Ni bulk sample on the same level of intrinsic resistance to WDE as the aluminum alloys, although it performed better in the experiments carried out in the present thesis. Therefore, index $I_2$ is a better candidate but it is still not a universal indicator.

Finally, index $I_4$, which is an extrapolation of $I_2$ including the influence of the sample density, seems to follow accurately the experimental results. Still, as no rigorous development of this index was performed here, it should not be seen as a global parameter and should be further studied on other materials, under more severe erosion conditions.

Figure 60 illustrates a material property map showing different materials with index $I_4$ as y-axis and the fracture toughness $K_{I,c}$ as x-axis for different material classes. The materials with the best index can be found on the top of the chart. To distinguish two materials with the same performance index, one could chose the tougher one, with a higher $K_{I,c}$. This justifies the choice of x-axis for Figure 60. Once heavier erosion stages are reached, with severe crack initiation zones, materials with higher fracture toughness are expected to have a longer resistance to erosion and a lower material loss rate. Indeed, the damage zones created in the early stages of erosion will certainly create cracks, which should not propagate to avoid further damage. As a result, for heavily eroded samples, materials with high fracture toughness are likely to resist better further erosion.

One should note that in Figure 60, the units used for the $I_4$ performance index are $\left[\frac{kg.MPa^2.GPa}{m^3}\right]$. Indeed, the density $\rho_s$, the yield strength $\sigma_y$ and Young's modulus $E$ were used in their most common units, namely $kg/m^3$, $MPa$ and $GPa$ respectively. As a result, there is a factor $10^{21}$ difference between the values of $I_4$ in Figure 60 and in Table 12.

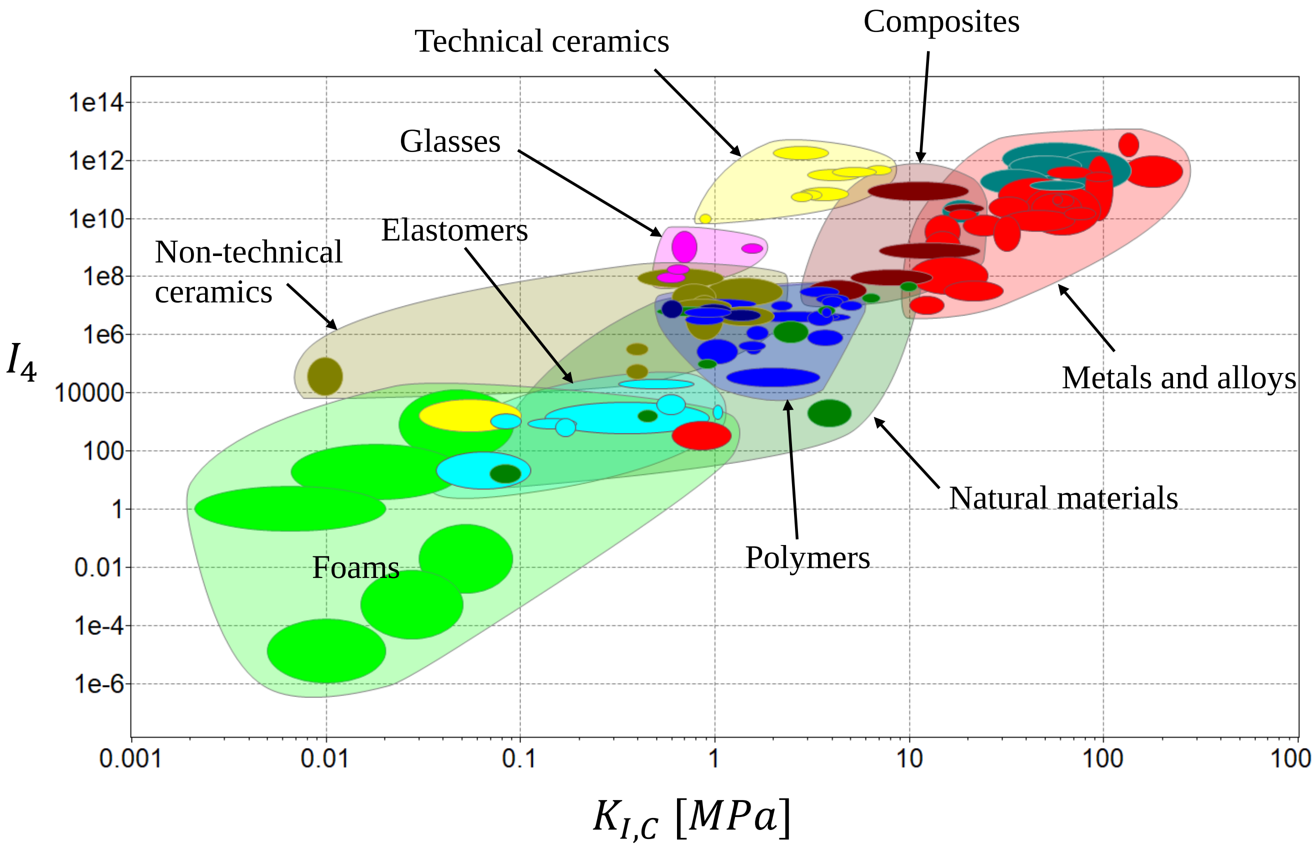

Figure 60: Material property chart illustrating index $I_4 = \rho\sigma_y^2 E$ in the y-axis and fracture toughness $K_{I,c}$ in the x-axis for most classes of materials. This material chart was obtained using *CES EduPack 2019* by *Granta*.

As can be seen in this chart, the best performing class of materials is the metallic alloys. One should note that in this graph the polymer-based composites seem to perform as well as most metallic alloys as they have a similar value of $I_4$ despite their lower density. This gives a wrong representation of the situation since the properties illustrated in the graph are along the strongest direction, namely the fibers direction. In reality, the water droplets impact the material in the out-of-plane direction, perpendicular to the fibers plane. At the surface of the composite, where the impacts happen, the material displays a layer of non-reinforced polymer. Therefore, instead of the in-plane properties, the out-of-plane strength and modulus should be considered, which correspond to classical, non-reinforced polymers. Indeed, polymer-based composites show poor resistance when exposed to water droplet impingement and fail by decohesion of the reinforcement upon damage of the matrix. Therefore, the 'composites' bubble in Figure 60 gives an incorrect, overestimated representation of the performances of composites based on $I_4$ and will not be considered further.

Similarly, technical ceramics also show excellent $I_4$ index in Figure 60, this time explained by very high Young's modulus and yield strength. Still, they have poor performance in WDE because of their too low fracture toughness $K_{I,c}$ and their high density is problematic for most applications.

Since the material performance index used, $I_4$, is based on experimental observations in metals, one should question whether it gives an accurate representative of the resistance to WDE of other types of materials. For example, elastomers such as polyurethane paint used as protection solution in airplanes have poor properties based on $I_4$. Still, when used as a 200 µm coating, such elastomers show good resistance to WDE and are a common solution used to protect parts exposed to rain erosion. One could cite for example *Mapcoat by AkzoNobel* which is recommended in the aerospace industry for protection of radomes or air inlets for instance. [71] These materials display good resistance to erosion thanks to their elastic behavior, which prevents plastic strain from building up. However, they require very thick coatings to absorb the impact energy due to their resilience. Another possible explanation for their good performance is that the pressure rise within the material is lower than in metals. Indeed, due to the low speed of sound $c_s$ through elastomers and the low density, the modified water-hammer pressure equation (3) predicts a pressure rise one order of magnitude lower than in their metallic counterparts. One should also consider the low toughness of elastomers and their change of behavior at low temperatures.

As a result, the proposed index $I_4$ should only focus on the upper-right end of the materials shown in Figure 60, namely on metals and their alloys. Figure 61 is a similar material properties chart as Figure 60, zooming on the metals and alloys family. The three material types tested in the present work, namely Al7075, Ti6Al4V and Ni bulk, are highlighted in the chart.

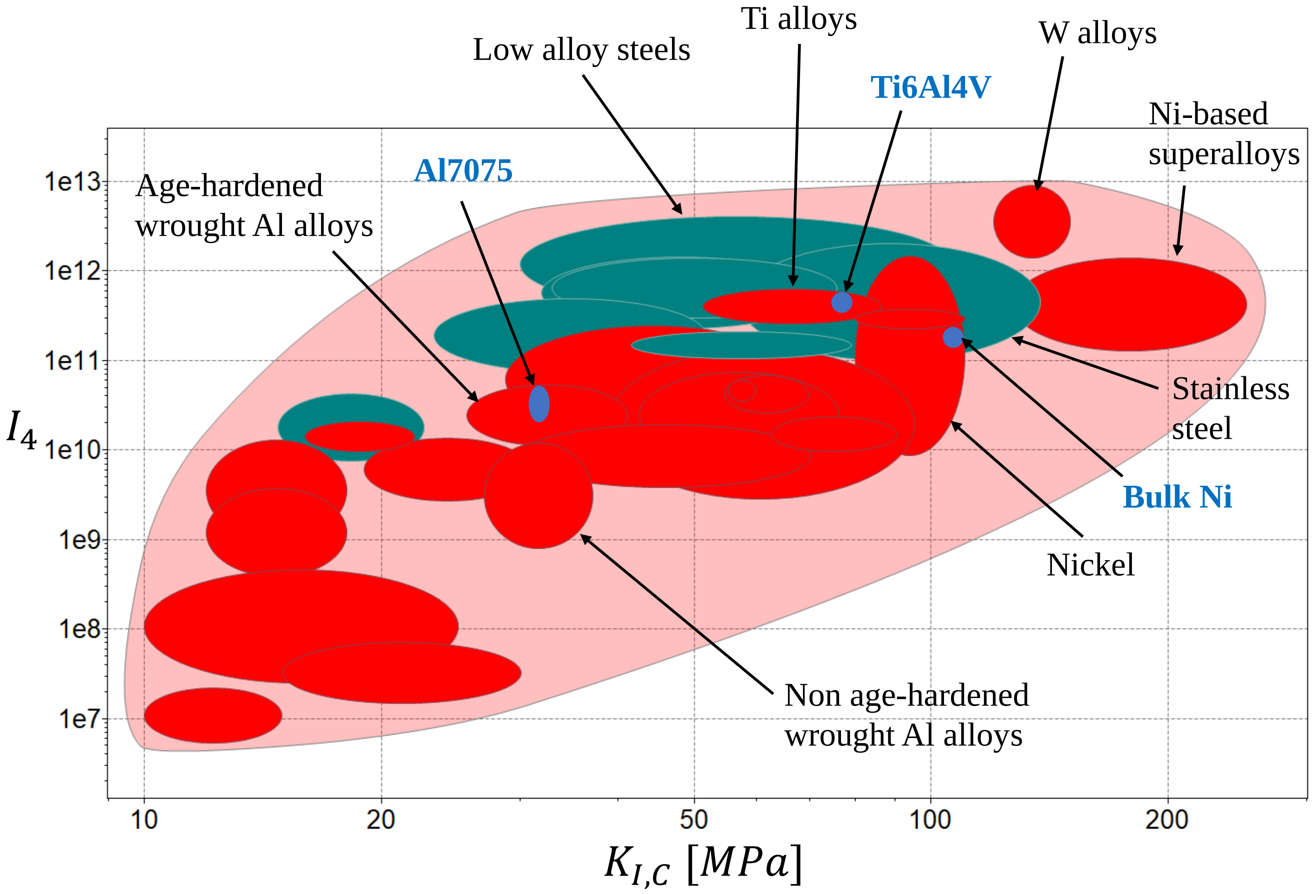

Figure 61: Material property chart illustrating index $I_4 = \rho\sigma_y^2 E$ in the y-axis and fracture toughness $K_{I,c}$ in the x-axis for metals and alloys. The three main materials tested in the present work, namely Al7075, Ti6Al4V and Ni bulk, are comprised in the Age-hardened wrought Al alloys, Ti alloys and Nickel bubbles respectively. They are highlighted as blue dots. This material chart was obtained using *CES EduPack 2019* by *Granta.*

As can be seen in Figure 61, the index $I_4$ ranks the materials in a similar way as the experiments. The Al7075 alloys have an oval shape in the age-hardened wrought Al alloys bubble. Indeed, the Al7075

T4 is at the bottom of the oval while the T6 treated samples is at the top. It is interesting to note that, as shown by F. Hannard [50], the friction stir processing does not influence significantly the toughness, while it improves ductility. Therefore, all three samples are located at a similar $K_{I,C}$. Figure 61 clearly illustrates the improved resistance to erosion that age-hardening brings to aluminum alloys. Indeed, the non age-hardened wrought Al alloys have a $I_4$ performance index one order of magnitude lower than the age-hardened ones. In addition, Figure 61 confirms that the Ni bulk sample has a slightly higher value of $I_4$ than the Al7075 T6. One would prefer nickel in this case as it has much better fracture toughness on top of a better $I_4$ index. If one were to place the electroplated nickel used in the present work, it would have higher $I_4$ but lower $K_{I,C}$ than the bulk nickel. Indeed, electroplated nickel is harder but more brittle than to its bulk counterpart.

As can be seen in Figure 61, the titanium alloys are an order of magnitude higher in terms of index $I_4$, as well as for the other material performance indices found in Table 12. A better alternative to titanium alloys could be nickel-based superalloys, which show excellent strength and corrosion resistance. These superalloys seem at first sight to be good candidates but further study should be performed. Similarly, one should study low alloy steels and stainless steels which seem to have good performance and decent fracture toughness, but are also probably too heavy and bulky for most applications.

Note that based on Figure 61, tungsten alloys seem to be excellent candidates. However, tungsten alloys are probably a too expensive solution to be commercialized. Besides, they have a too high density to be applicable to most applications. This shows a limitation of the index $I_4$ as the materials with extremely high density, such as tungsten alloys, have excellent ranking but are likely to be unusable for most applications. A solution would be to perform hardfacing of tungsten carbide on an aluminum base for example, as it creates a hard and extremely wear resistant protection layer. This should be further studied, particularly for the impact resistance, the compatibility and the adhesion with the structural base.

Besides the parameters aforementioned, in the case of aeronautic applications, one should also make sure the material can withstand temperature variations from -60°C, which corresponds to the air temperature at cruising altitude, up to +50°C, when the plane is on the ground. The temperature variations can cause stresses or warping if dissimilar materials are assembled. This is the case for sandwich hybrids, which require two faces and compatible thermal expansion coefficients between the materials. Otherwise, as one material dilates more than the other, stresses build up at the interfaces when the components are joined leading to cracking, warping or delamination.

In addition, one should pay attention to galvanic corrosion which appears between pairs of components, such as between carbon fiber reinforced polymers and aluminum alloys, as mentioned by Wu et al. [72]

One should investigate the influence of the strain rate, which is high in the case of water droplet impingement, on the mechanical properties of the materials. It is well known that strain rate and temperature have a very significant influence on the observed properties of polymers due to their viscoelastic nature, as reviewed by Siviour et al. [73]. It is also the case, to a lesser extent, for metals and their alloys. Indeed, the dynamic stress-strain curves are significantly altered when working at strain rates up to $10^5$ $s^{-1}$. Figure 62 highlights the strain rate regimes and the experiments used to assess the response in each regime. Note that this figure underlines the importance of inertia under high strain rates, which justifies the introduction of $\rho$ in the performance index $I_4$.

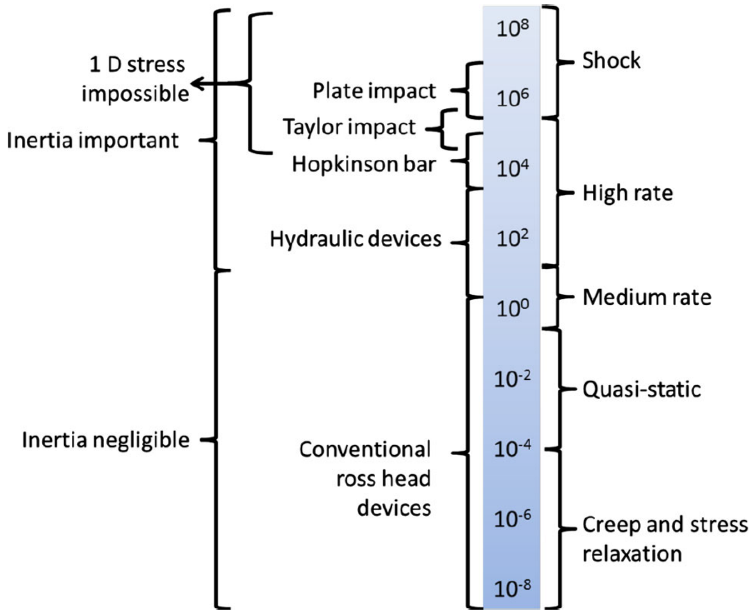

Figure 62: Division of the strain rate regimes in $s^{-1}$ and the experiments associated to each regime. Image from Siviour et al. [73]

Mukherjee et al. [74] performed split Hopkinson pressure bar tests on Al7075 and confirmed that increasing the strain rate increases the yield strength of the material. On the other hand, as suggested by Pothnis et al. [75], most materials switch from a ductile failure mechanism to a brittle behavior under high strain rates, which influences the erosion mechanisms depending on the impact speed. Mechanical properties obtained at high strain rates are more relevant to assess WDE than the quasi-static properties commonly used. The influence of the dynamic loading on the stress-strain response could allow to design a universal performance index including other materials families than metallic alloys.

To assess the strain hardening linked to the high deformation rate, the most commonly used model is Johnson-Cook flow stress, as mentioned by J. Bergström. [76] It predicts the evolution of the yield surface of a material based on the strain hardening and the temperature softening. Therefore, this model seems to be an efficient tool in predicting the material response under varying water droplet impact speeds and atmospheric temperatures. Johnson-Cook model links the yield stress $\sigma_y$ to the equivalent plastic strain $\varepsilon_p$, the plastic strain rate $\dot{\varepsilon}_p$ and the temperature $T$ as in equation (19). In equation (19), $A$, $B$, $C$, $n$ and $m$ are material-specific constants. $T_m$ is the melting temperature, $T_0$ is a reference temperature - usually room temperature - and $\dot{\varepsilon}_{p,0}$ is an equivalent plastic strain rate used for quasi-static loading, namely 1 $s^{-1}$.

$$\sigma_y = \left[A + B\,\varepsilon_p^n\right]\left[1 + C\,ln\left(\frac{\dot{\varepsilon}_p}{\dot{\varepsilon}_{p,0}}\right)\right]\left[1 - \left(\frac{T - T_0}{T_m - T_0}\right)^m\right] \tag{19}$$

However, as stated by Sasso et al. [77], uncontrollable experimental parameters influence the results obtained at high strain rate, such as non constant strain rate, non uniform stress-strain distribution and temperature rise due to plastic work. Due to these phenomena intrinsically linked to split Hopkinson pressure bar tests, the apparent mechanical properties can be far from the true material properties. Based on these dynamic response tests, the density of the material would be implicitly considered and another material performance index would probably have to be found. Further investigation on the dynamic stress-strain response of materials could bring more insight in the prediction of WDE.

All in all, the material performance charts should not be taken as sole decision criterion to select an erosion resistant material. Indeed, besides experimental material performance indices, important constraints such as corrosion resistance, impact resistance, weight and cost are at least as important for practical applications such as aviation and wind power. In addition, up to now, no validated erosion performance index has been developed. Therefore, one could still accept the possibility of an independent macroscopic material property, which would characterize the resistance to water droplet erosion. For that purpose, a standardized property assessment procedure, such as using PJET or WARER facilities under reference conditions, would have to be defined. Until then, a simple and qualitative comparison using both techniques can be considered as the best way to predict long term resistance to water droplet erosion.

# Conclusion

**Water droplet erosion** (WDE) is a mechanism responsible for damage on surfaces exposed to droplets impinging at high speed, such as leading edges of airplanes or blades of wind turbines. Due to the repeated impacts of water droplets, several mechanisms happen in the impinged material. The impact loading creates a sub-surface pressure rise, which leads to stress waves propagating through the material. As a consequence, the material goes through several stages of erosion, the first of which being the incubation. Current solutions include polymer coatings, paints or Al2024 aluminum alloys cladded with pure aluminum to resist corrosion.

Two different techniques were compared in the present work to assess the resistance of a material to WDE, namely a **whirling arm rain erosion rig** (WARER) developed at *UCLouvain* and a **pulsating jet erosion test** (PJET) used at *Sonaca*. The WARER accelerates the sample to collide it with controlled free falling droplets while the PJET projects a chosen number of droplets towards the stationary sample. Both techniques can simulate rainfall rates equivalent to 20-25 mm/h, which corresponds to heavy rain. The WARER used in the present work is limited to impacts at 120 m/s while the PJET can span droplet speeds between 180 m/s and 225 m/s. The testing conditions chosen were up to 18 hours at 120 m/s impacts in the WARER and up to 20 000 impacts at 180 m/s or 225 m/s in the PJET. Despite the difference in terms of area eroded and therefore frequency of impacts per unit surface, both techniques give results which can be correlated for most metallic materials.

In the present work, five main metallic materials were tested, namely Al7075 T4, Al7075 T6, Al7075 FSP T6, Ni bulk and Ti6Al4V. These materials were chosen for the range of mechanical properties they exhibit, allowing to compare the influence of certain parameters on the resistance to WDE. To assess the level of erosion reached by the materials, several techniques were used, including observation with scanning electron microscopy, digital microscopy and assessment of the roughness thanks to laser interferometry. An analysis of the weight loss was not possible for the PJET samples due to the configuration of the machine and no mass loss was observed in the WARER samples after 18 hours of erosion at 120 m/s impacts. This indicates that, with the chosen parameters, the samples remained in the early stages of erosion, namely the incubation period where no significant mass loss is measured. For example, the experiments showed that at the early stages of erosion, the enhanced ductility of the friction stir processed Al7075 FSP T6 sample did not lead to improved erosion performances compared to the Al7075 T6 sample. This highlights that, interestingly, the ductility does not influence significantly the resistance to WDE in the incubation stage.

In all the samples, similar **erosion damage mechanisms** were highlighted at different scales. The first mechanism, at the macro-scale is the creation of wide (about 10 µm) but shallow valleys in the material, in a **peening** manner. Down to the micro-scale, two other damage mechanisms were observed, in the form of **pitting**. On one hand, isolated pits nucleate at surface defects or grain boundaries, then grow independently upon subsequent impacts up to a width of 5 µm before merging with neighboring pits. On the other hand, scratches-nucleated pitting was also observed, located along the grooves created by the polishing step. These pits deepen and broaden the scratches, progressing preferentially in the direction of the grooves. This shows that the initial surface roughness, even down to the sub-micron scale, has an influence on the resistance to water droplet erosion. In addition to those damage mechanisms, the WARER eroded samples showed deep, sharp and rectilinear scratches created by solid-particle impacts, due to dust particles in suspension in the machine chamber.

The evolution of the erosion damage of the samples as a function of the energy received by the PJET impacts was quantified using several **roughness parameters**, namely $R_a$, $R_{ku}$ and $R_{sk}$. These were measured with laser interferometry. While the **arithmetic mean roughness** $R_a$ gives a basis for comparison, it hides the erosion mechanisms since very different profiles can have similar $R_a$. The **kurtosis** $R_{ku}$ reflects the sharpness of the features, hence an image of the erosion damage. Finally, the **skewness** $R_{sk}$, which illustrates the asymmetry of the surface profile with respect to the mean line, allows to compare quantitatively the pitting damage. Showing both a low arithmetic mean roughness parameter $R_a$, combined with a $R_{sk}$ close to 0 characterizes a material with good resistance to WDE. One should however be critical with the results obtained by laser interferometry since fringes tend to appear for samples in the early stages of erosion. This technique would be more accurate at more advanced erosion stages.

A **correlation** between the WARER and the PJET results was established via an estimation of the total energy received by the sample on a zone of similar dimensions in both techniques. Indeed, based on the samples tested in the present work, a correlation seems to exist between 18 hours of exposure to 120 m/s droplets in the WARER at standard conditions and 9 000 impacts in the PJET at 225 m/s or 15 000 impacts at 180 m/s. This correlation was confirmed by a comparison of the roughness parameters $R_a$, $R_{ku}$ and $R_{sk}$ measured for both WARER and PJET samples.

The present work therefore showed that both PJET and WARER techniques give significant indications on the resistance to WDE. Although the WARER reproduces a behavior closer to natural conditions, the PJET should be favored to isolate the effect of water droplet mechanisms from the solid-particle impingement. Indeed, because of dust particles, the WARER technique provides less repeatable measurements, unless the tests are performed in a perfectly clean, dust-free environment. One should also mention that the WARER is the set-up recommended for standard testing of liquid impingement erosion, with ASTM G73-10 reference. [36] Still, the PJET technique is faster by localizing the impacts at higher rate on a smaller erosion zone. The present work highlighted that the erosion mechanisms, except for the solid-particle impingement, are similar in both techniques for the metallic samples tested. On the other hand, for polymeric samples which do not have time to relax before a subsequent loading, the discrepancy in terms of impact frequency between PJET and WARER is critical and does not allow direct correlation of both techniques.

Several **material performance index** candidates were tested and compared to the $R_{sk}$ parameter-based ranking. The properties considered were the **yield strength** and **Young's modulus**, which seem to be the most influential macroscopic parameters to assess the resistance to WDE. Based on the skewness $R_{sk}$, the samples can be ranked by increasing resistance to WDE as follows: Al7075 T4, Al7075 T6, Al7075 FSP T6, Ni bulk and Ti6Al4V. All the performance indices presented in this work correctly predicted the domination of Ti6Al4V over the other materials. However, they do not seem to be universal indicators. Indeed, the performance of the bulk nickel sample was undervalued by the indices, except when the **density** of the material was considered. This could be corrected by working with mechanical properties obtained at high strain rate, to include the dynamic behavior of the materials. Besides the resistance to WDE, several other as important parameters are required for most applications, such as the toughness, the weight, the cost and the corrosion resistance. An improved protection solution to WDE which should be investigated is tungsten carbide hardfacing. However, one should ensure excellent adhesion with the substrate, which is a critical failure mechanism of coated or plated materials. This was experienced in the present work as electroplated nickel, with high hardness but low toughness, quickly failed due to delamination, nucleated by local plating defects.

When it comes to suggestions for future work, the following points mentioned in the present work would require additional study:

- In terms of material performance index, the influence of the **ductility** and the **dynamic properties**, via the density of the material, should be further investigated. Indeed, the materials tested in the present work remained in the early stages of erosion, namely the incubation period, where the ductility may have less influence than in more advanced erosion stages. In addition, although dynamic response of the material is expected under high speed impact, the influence of the material density has not been extensively studied yet.

- The **initial surface topography** and roughness, even down to sub-micron features, have significant influence on the erosion performance, as shown by the scratches-induced erosion mechanisms highlighted in this work. Patterning the material surface with laser etching for instance, would help understand the influence of the initial surface roughness and topographic features. Indeed, by fine tuning the pattern down to the sub-micron scale, the surface defects which seem to initiate erosion damage mechanisms would be controlled. One could try different patterns at different scales to identify a sequence - probably material-dependent - which improves resistance to WDE. Conversely, one could try further polishing techniques, such as electropolishing to delay the appearance of erosion mechanisms and extend the incubation period.

- A further study of the difference between the Al7075 T6 and Al7075 FSP T6 materials would allow to identify the influence of the ductility of a material on its resistance to WDE. Indeed, both materials are similar, except the size and dispersion of the intermetallic inclusions thanks to **friction stir processing**. This FSP step brings an increased ductility, which is probably a parameter influencing erosion in more advanced stages of damage. Therefore, comparing the friction stir processed material to the reference one at more advanced erosion stages would be of great interest.

- Finally, further investigation should be performed on all of the **macroscopic material properties** which influence the resistance to WDE. Indeed, in order to develop a universal material performance index, the individual influence of each parameter should be identified as well as the influence of their dynamic response. The relative weight of parameters such as the strength, the toughness, the strain hardening, Young's modulus or the density, may likely vary depending on the experimental conditions. Therefore, standardization of the testing methods should be further expanded. Finally, investigations need to be performed to determine whether a material performance index describing resistance to WDE based on macroscopic properties such as hardness, toughness or strength, can actually be defined or whether it should be considered as an independent, macroscopic parameter.

# 6 Annex

## 6.1 Nano-indentation curves

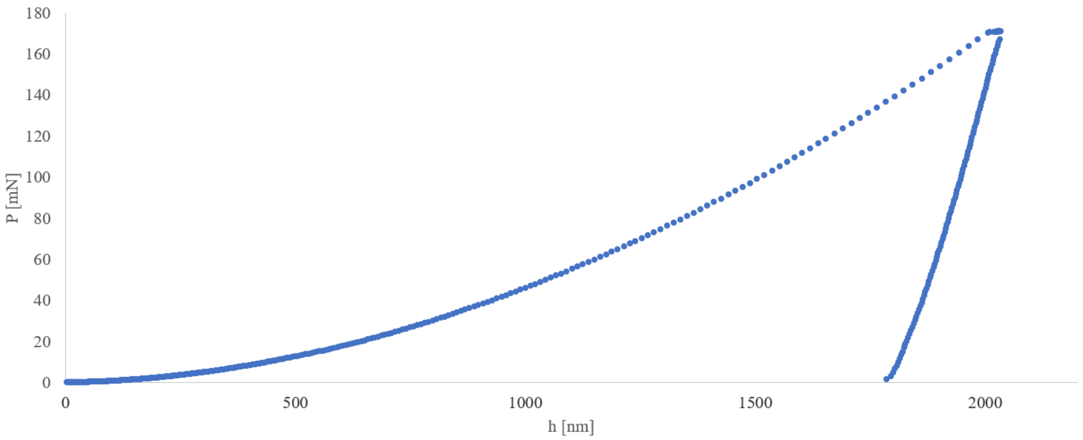

(a) Load $P$ as a function of the penetration depth $h$ for sample Al7075 T4.

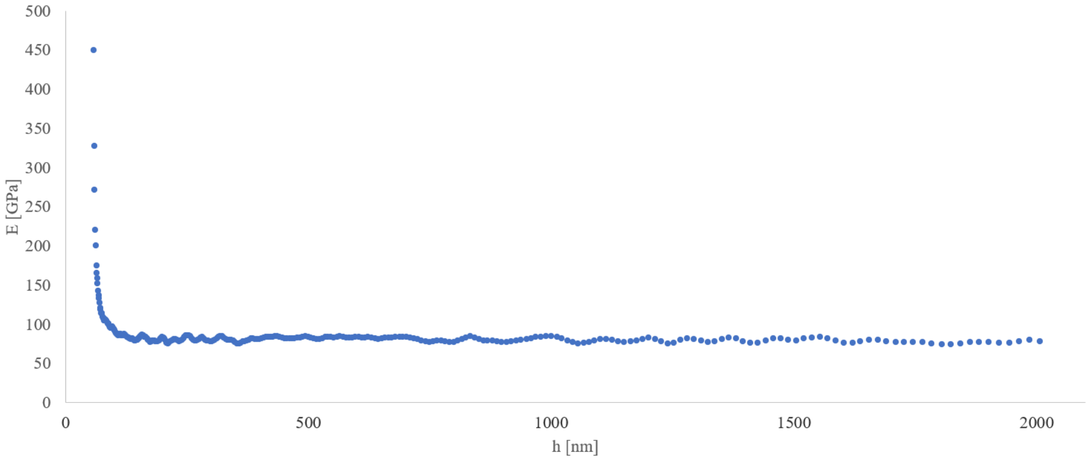

(b) Evolution of Young's modulus $E$ of the Al7075 T4 sample as a function of the penetration depth $h$.

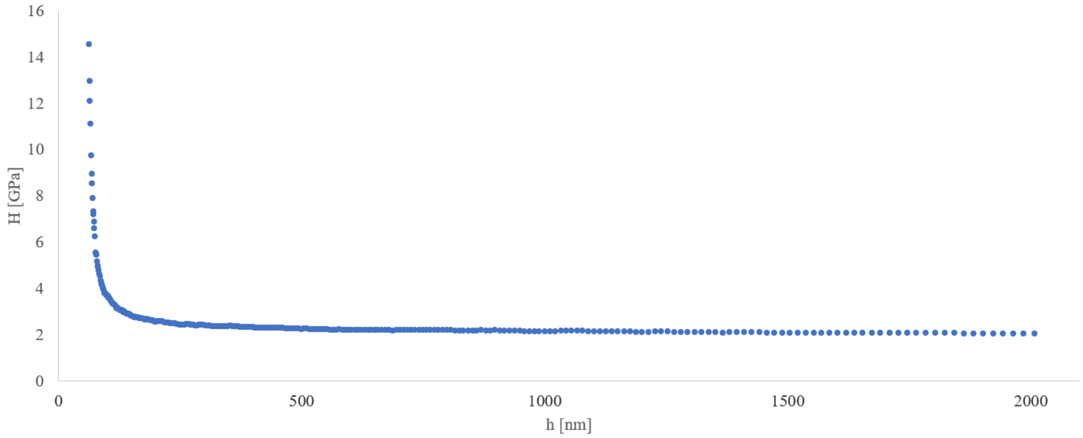

(c) Evolution of the hardness $H$ of the Al7075 T4 sample as a function of the penetration depth $h$.

Figure 63: Average nano-indentation curves of the Al7075 T4 sample.

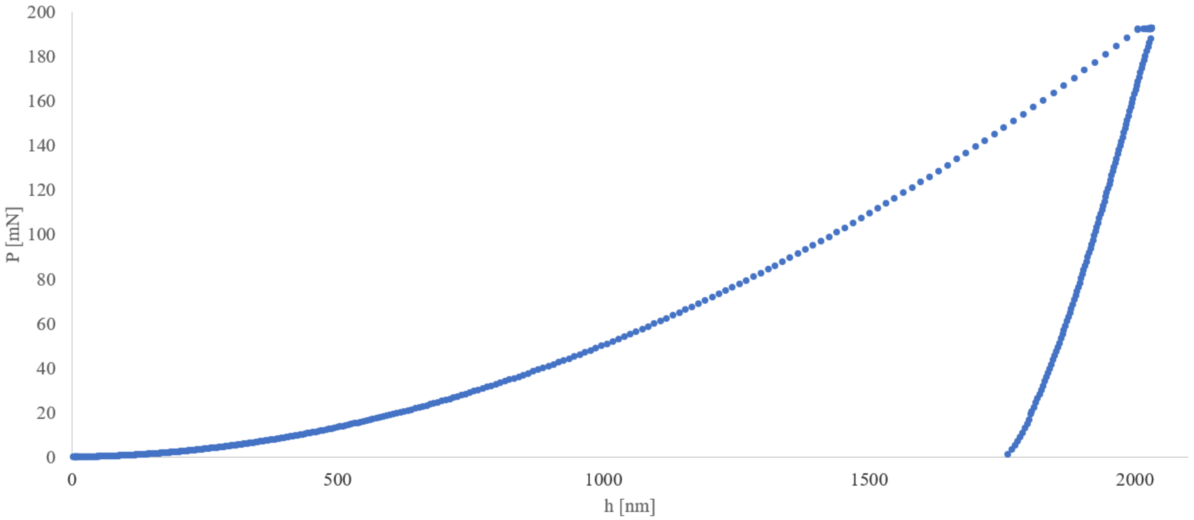

(a) Load $P$ as a function of the penetration depth $h$ for sample Al7075 T6.

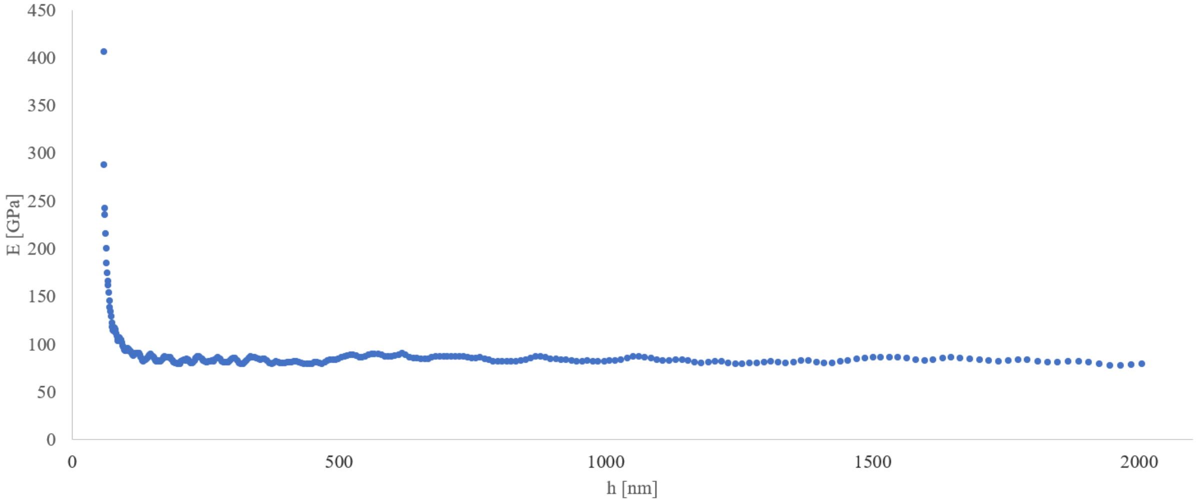

(b) Evolution of Young's modulus $E$ of the Al7075 T6 sample as a function of the penetration depth $h$.

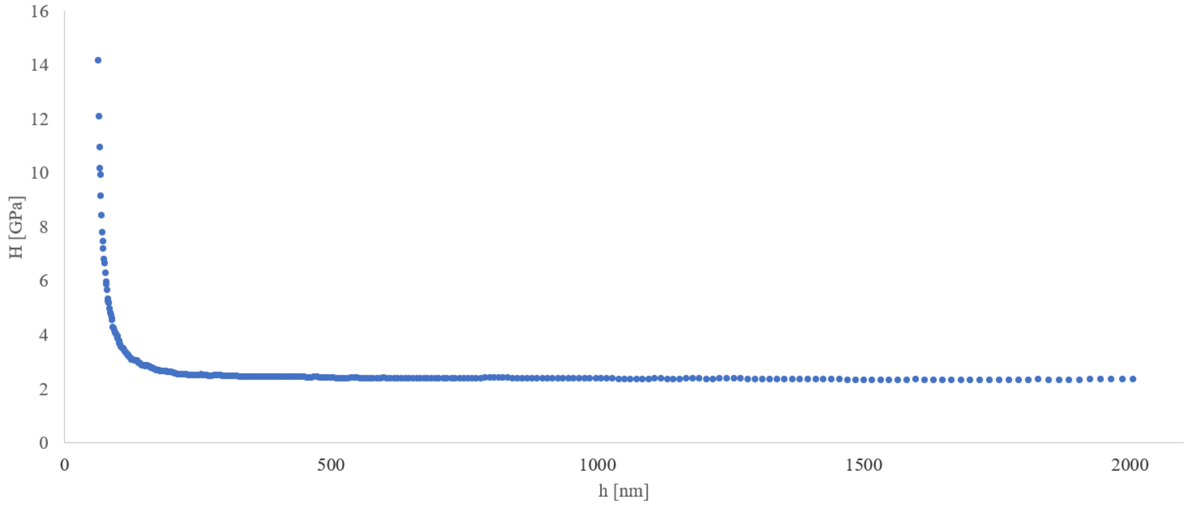

(c) Evolution of the hardness $H$ of the Al7075 T6 sample as a function of the penetration depth $h$.

Figure 64: Average nano-indentation curves of the Al7075 T6 sample.

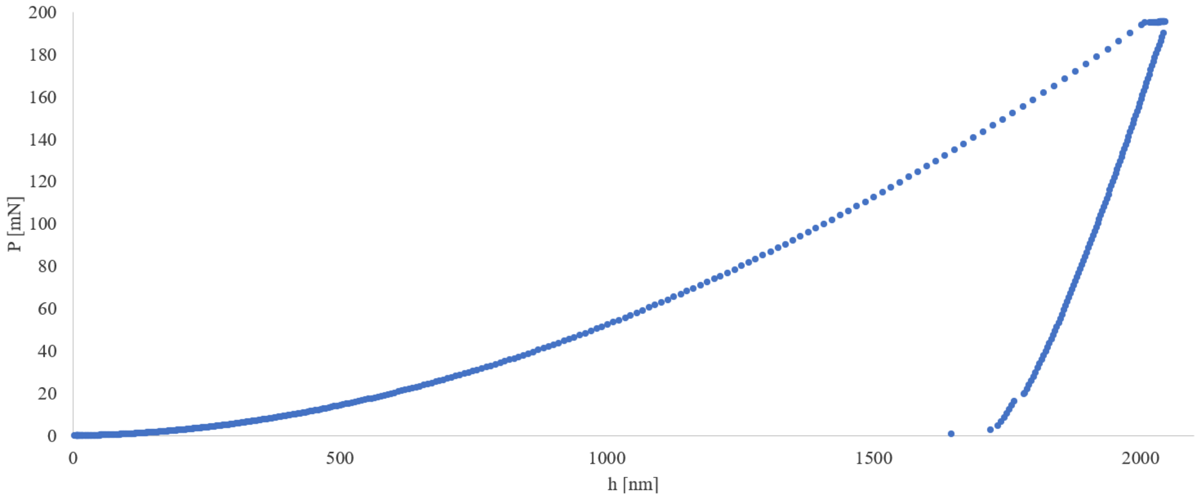

(a) Load $P$ as a function of the penetration depth $h$ for sample Al7075 FSP T6.

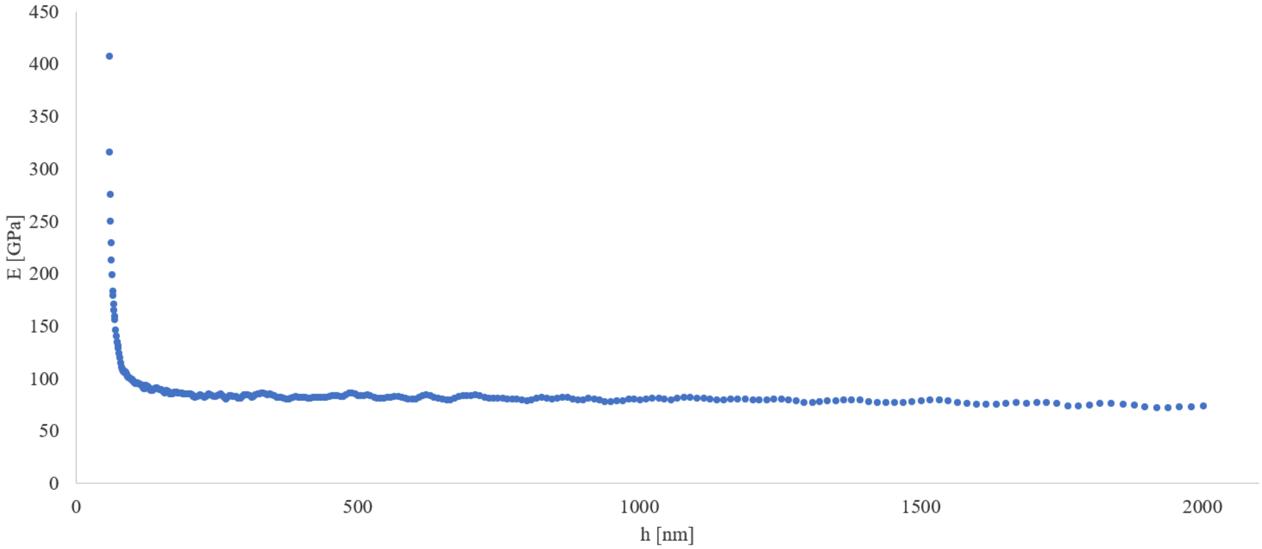

(b) Evolution of Young's modulus $E$ of the Al7075 FSP T6 sample as a function of the penetration depth $h$.

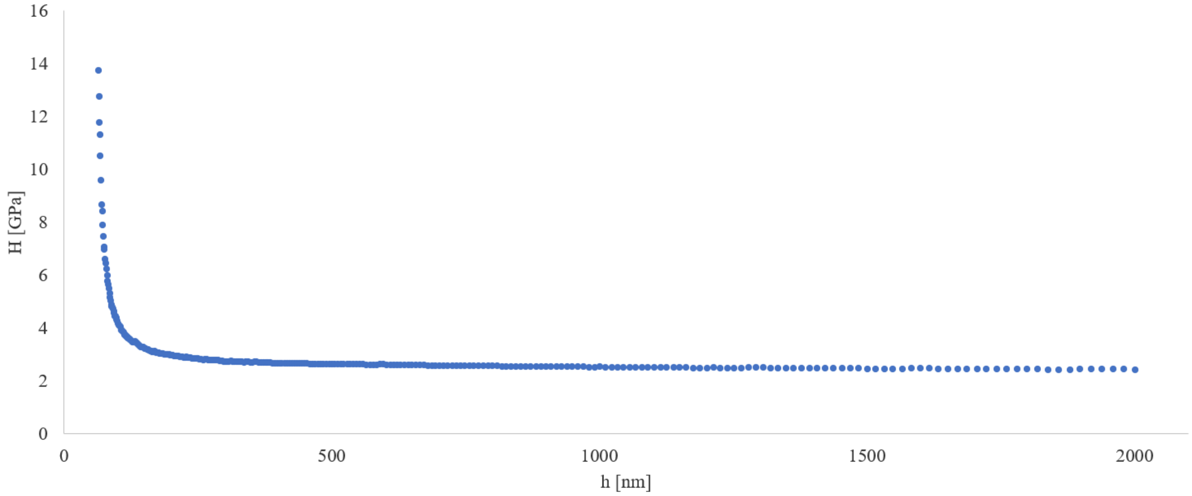

(c) Evolution of the hardness $H$ of the Al7075 FSP T6 sample as a function of the penetration depth $h$.

Figure 65: Average nano-indentation curves of the Al7075 FSP T6 sample.

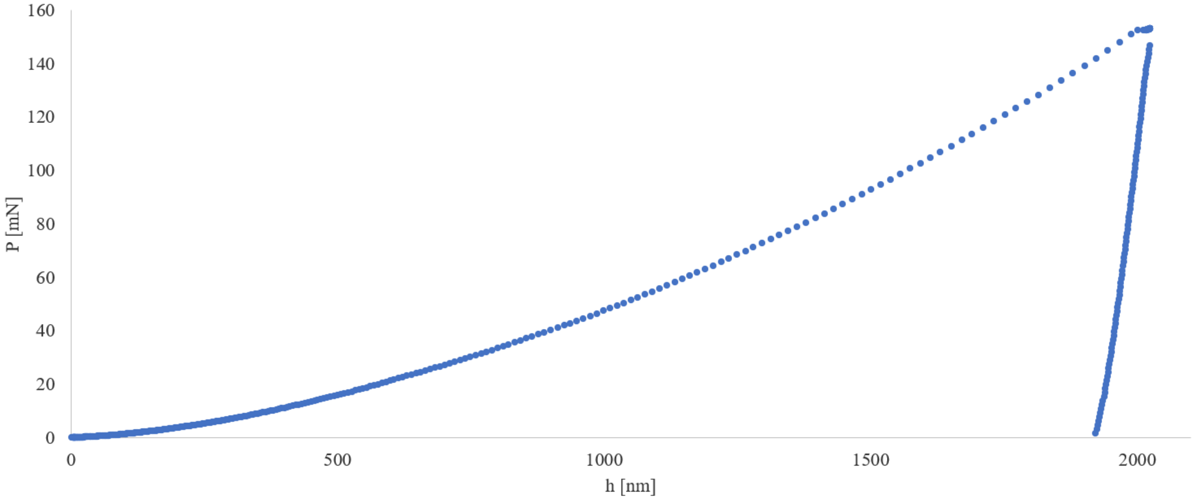

(a) Load $P$ as a function of the penetration depth $h$ for sample Ni bulk.

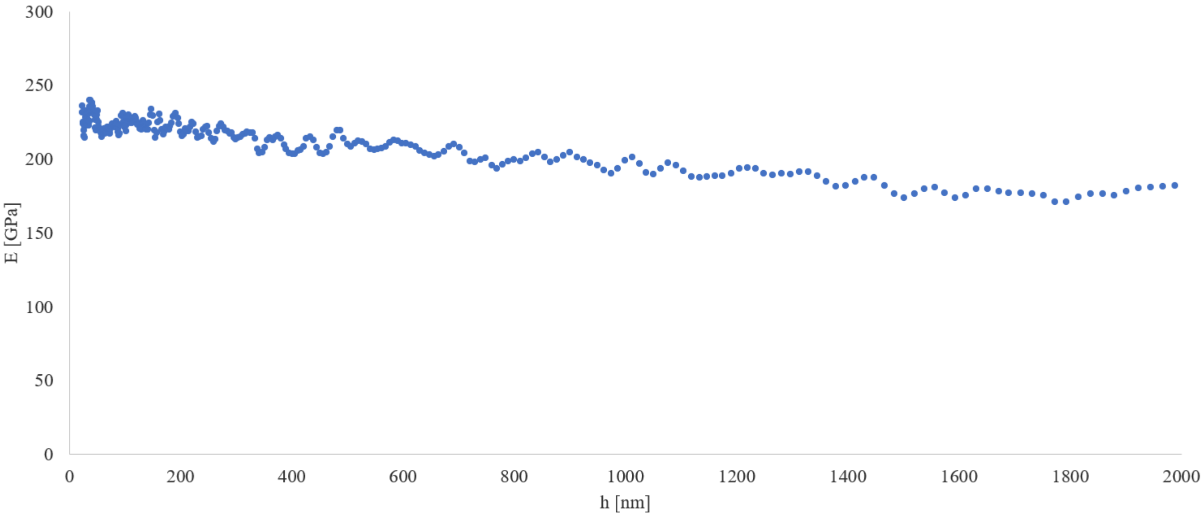

(b) Evolution of Young's modulus $E$ of the Ni bulk sample as a function of the penetration depth $h$.

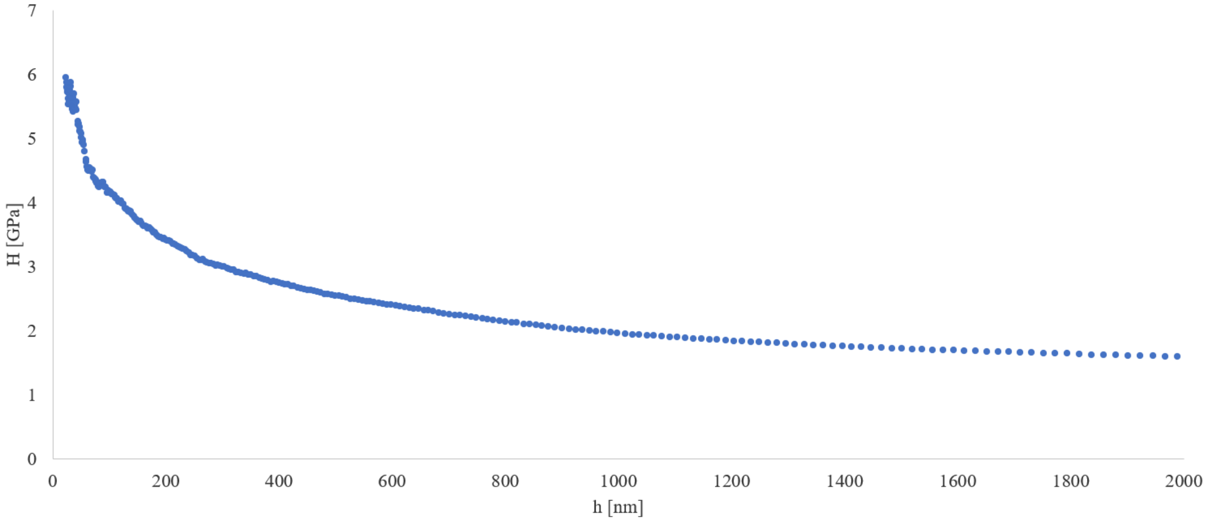

(c) Evolution of the hardness $H$ of the Ni bulk sample as a function of the penetration depth $h$.

Figure 66: Average nano-indentation curves of the Ni bulk sample.

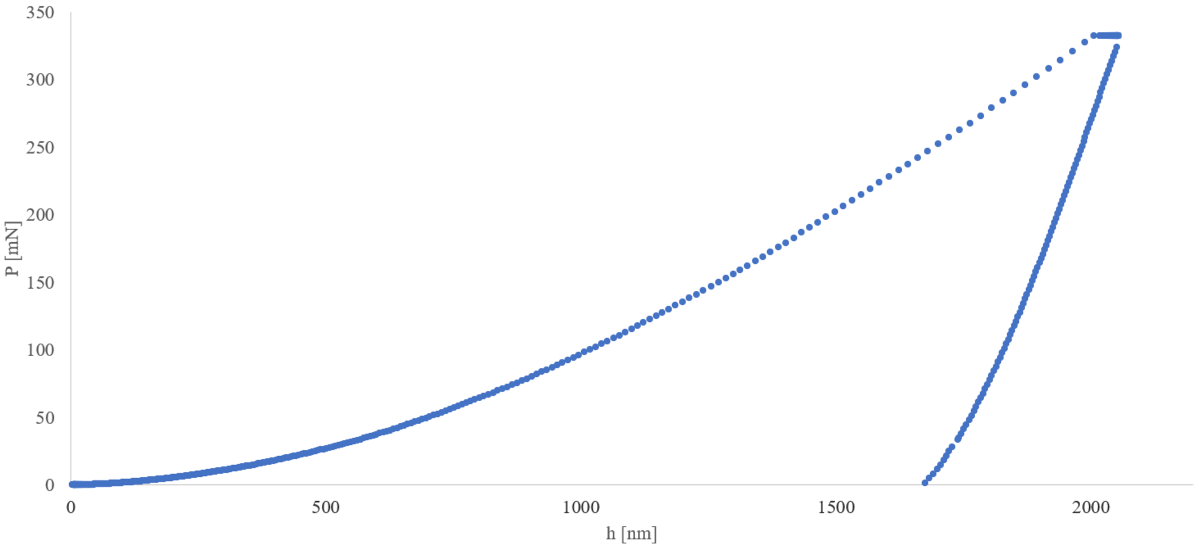

(a) Load $P$ as a function of the penetration depth $h$ for sample Ti6Al4V.

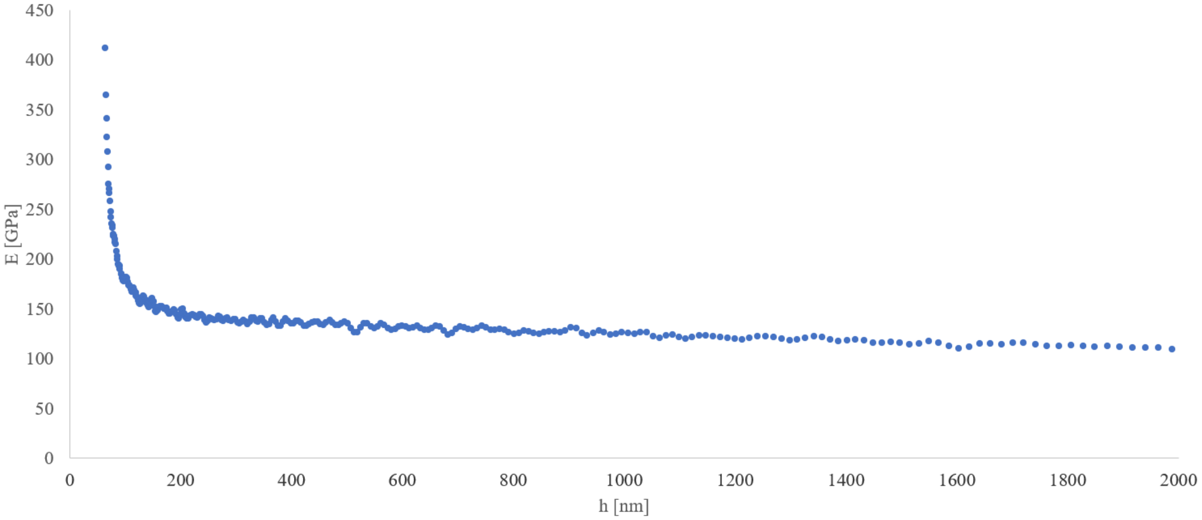

(b) Evolution of Young's modulus $E$ of the Ti6Al4V sample as a function of the penetration depth $h$.

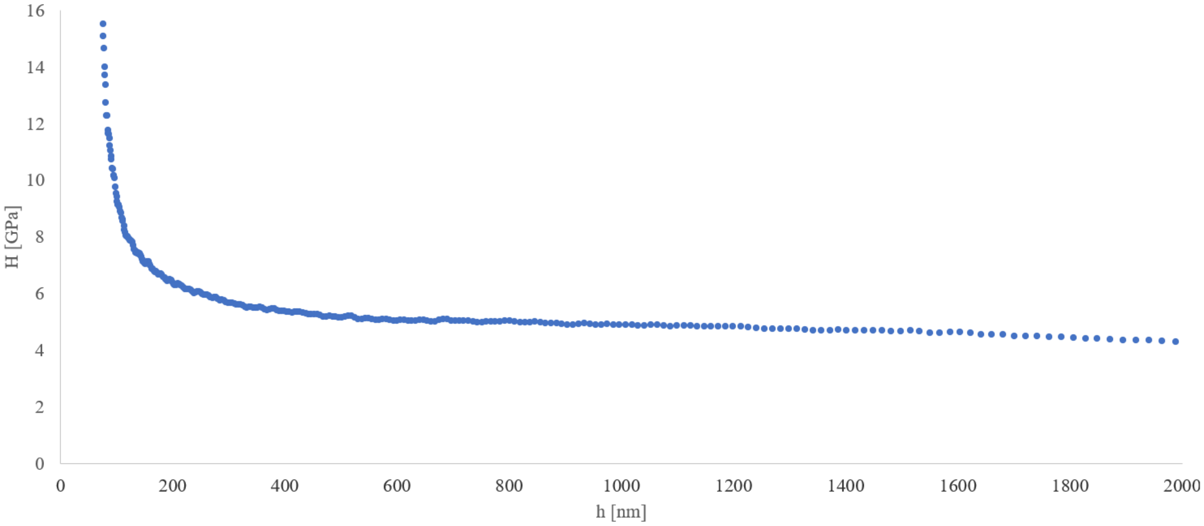

(c) Evolution of the hardness $H$ of the Ti6Al4V sample as a function of the penetration depth $h$.

Figure 67: Average nano-indentation curves of the Ti6Al4V sample.

## 6.2 Tensile tests on Ti6Al4V

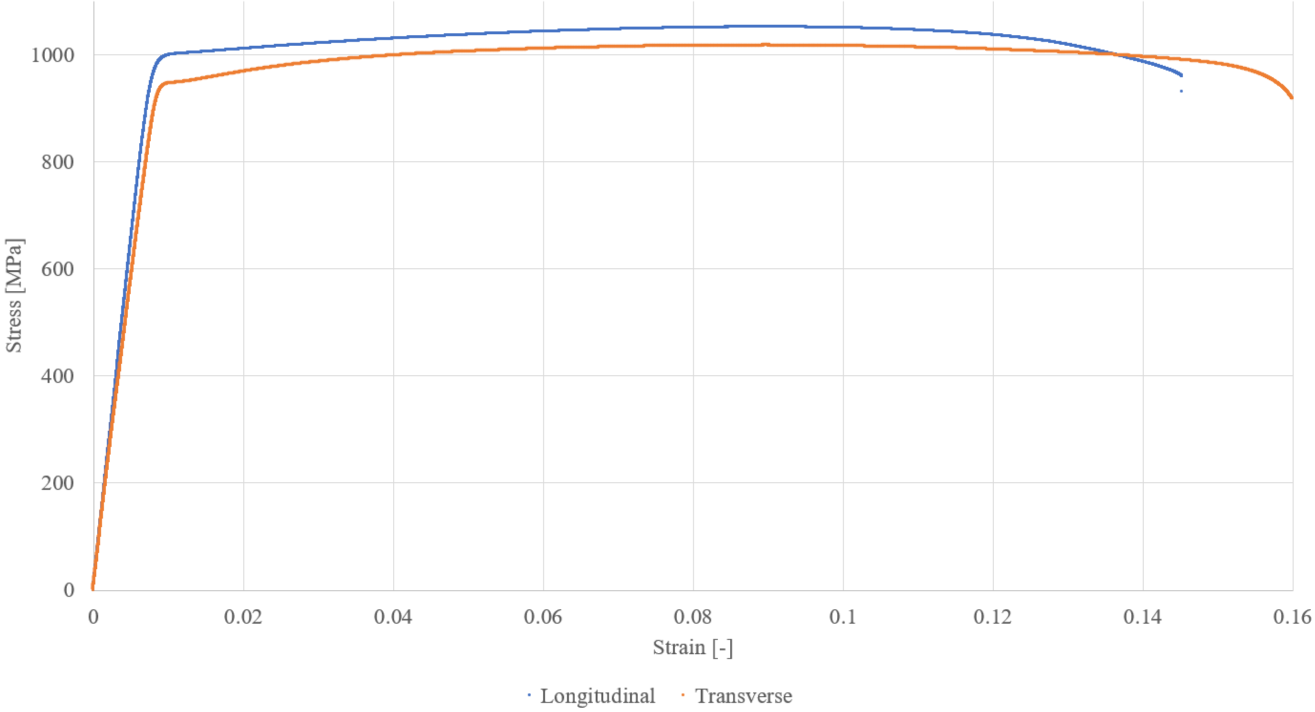

Figure 68: Stress-strain curves of the dog-bone traction samples of Ti6Al4V. The longitudinal curve is a sample pulled along the rolling direction while the transverse direction is perpendicular. Out of this graph, Young's modulus, yield strength and ultimate tensile strength can be deduced: $E_l = 126$ GPa, $\sigma_{y,0.002,l} = 945$ MPa, $\sigma_{u,l} = 1050$ MPa and $E_t = 114$ GPa, $\sigma_{y,0.002,t} = 945$ MPa, $\sigma_{u,t} = 1020$ MPa.

## 6.3 Energy-dispersive X-ray spectroscopy on Al7075 FSP T6

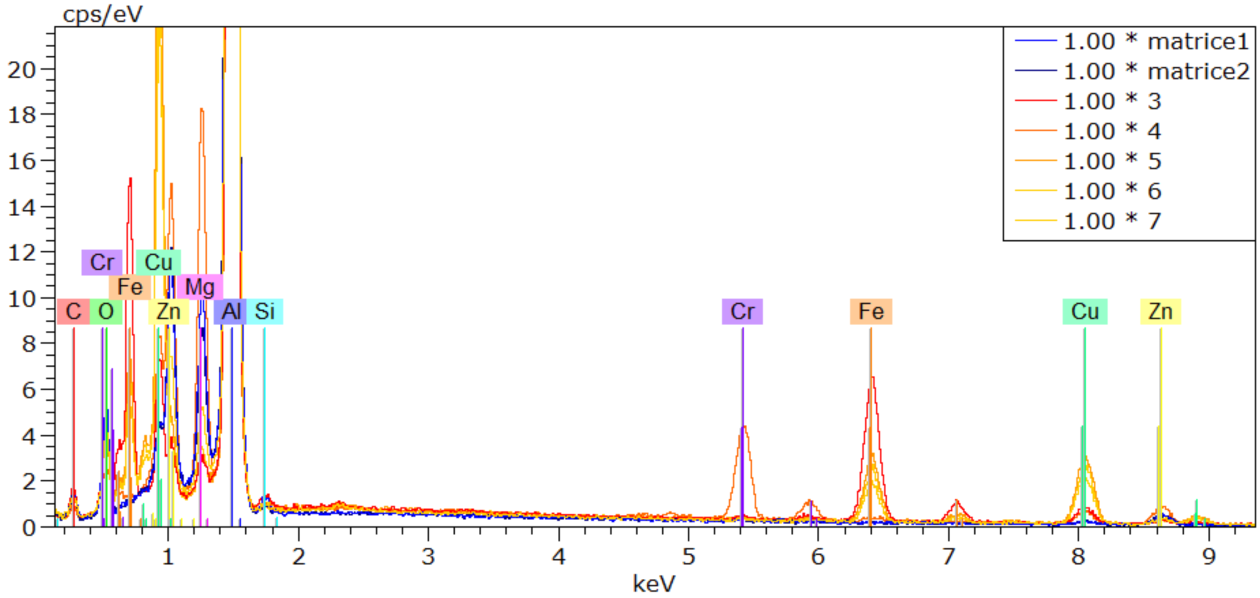

Figure 69: Energy-dispersive X-ray spectroscopy on the Al7075 FSP T6 sample. The different spectra correspond to the zones highlighted in Figure 27. Matrice1 and Matrice2 are two spectra of the matrix phase while curves 3 to 7 are spectra of the inclusion particles. One should refer to Figure 27 for the location of the zones where the spectra were measured.

| Spectrum | C | O | Mg | Al | Si | Cr | Fe | Cu | Zn |
|---|---|---|---|---|---|---|---|---|---|
| Matrice1 | 6.54 | 5.33 | 3.24 | 78.22 | 0.51 | 0.15 | 0.00 | 1.15 | 4.85 |
| Matrice2 | 6.58 | 5.20 | 2.67 | 78.83 | 0.23 | 0.16 | 0.01 | 1.21 | 5.10 |
| 3 | 6.31 | 4.35 | 1.06 | 56.29 | 0.48 | 0.40 | 22.40 | 6.19 | 2.51 |
| 4 | 3.87 | 0.92 | 8.63 | 58.43 | 0.10 | 11.59 | 0.77 | 5.11 | 10.58 |
| 5 | 4.49 | 3.25 | 1.14 | 53.23 | 0.13 | 0.17 | 10.33 | 25.33 | 1.94 |
| 6 | 5.54 | 3.78 | 1.26 | 57.50 | 0.14 | 0.14 | 7.62 | 21.49 | 2.53 |
| 7 | 5.11 | 3.47 | 1.88 | 65.48 | 0.18 | 0.08 | 5.39 | 15.83 | 2.59 |

Table 13: Normalized mass fraction composition (in %) of each zone measured, referring to Figure 27.

| Spectrum | C | O | Mg | Al | Si | Cr | Fe | Cu | Zn |
|---|---|---|---|---|---|---|---|---|---|
| Matrice1 | 13.53 | 8.28 | 3.31 | 72.06 | 0.46 | 0.07 | 0.00 | 0.45 | 1.84 |
| Matrice2 | 13.65 | 8.09 | 2.74 | 72.81 | 0.21 | 0.08 | 0.01 | 0.48 | 1.94 |
| 3 | 15.05 | 7.80 | 1.26 | 59.79 | 0.49 | 0.22 | 11.49 | 2.79 | 1.10 |
| 4 | 9.53 | 1.70 | 10.49 | 64.01 | 0.11 | 6.59 | 0.41 | 2.38 | 4.78 |
| 5 | 11.63 | 6.32 | 1.45 | 61.30 | 0.14 | 0.10 | 5.75 | 12.39 | 0.92 |
| 6 | 13.57 | 6.95 | 1.52 | 62.65 | 0.15 | 0.08 | 4.01 | 9.94 | 1.14 |
| 7 | 12.02 | 6.13 | 2.19 | 68.56 | 0.18 | 0.04 | 2.73 | 7.04 | 1.12 |

Table 14: Normalized atomic fraction composition (in %) of each zone measured, referring to Figure 27.

## 6.4 Digital microscopy images of the WARER eroded samples

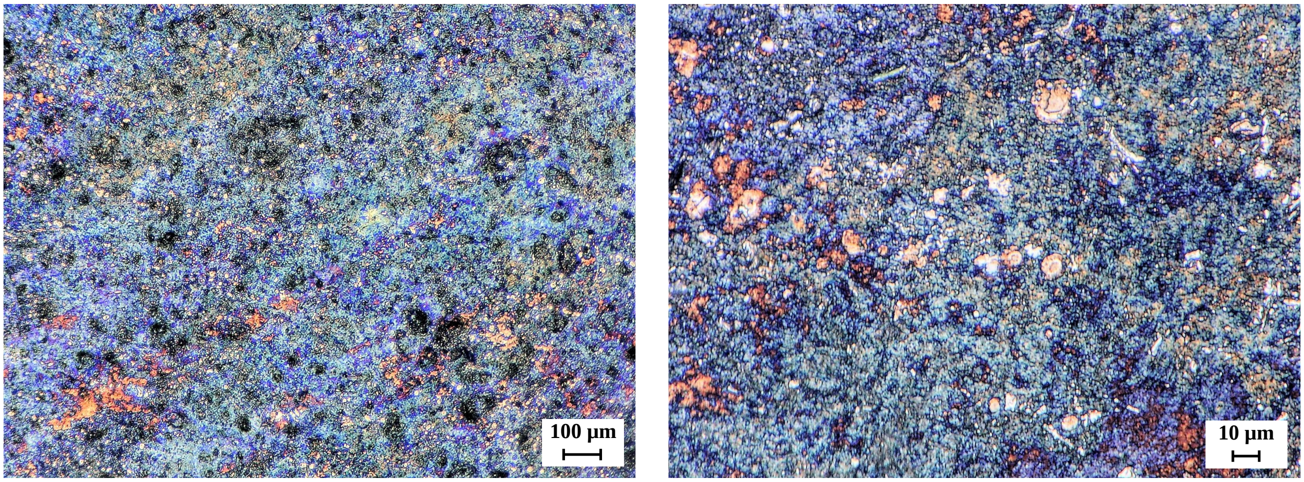

(a) (b)

Figure 70: Digital microscopy images at (a) low and (b) high magnification of the Al7075 T4 sample eroded with the WARER technique.

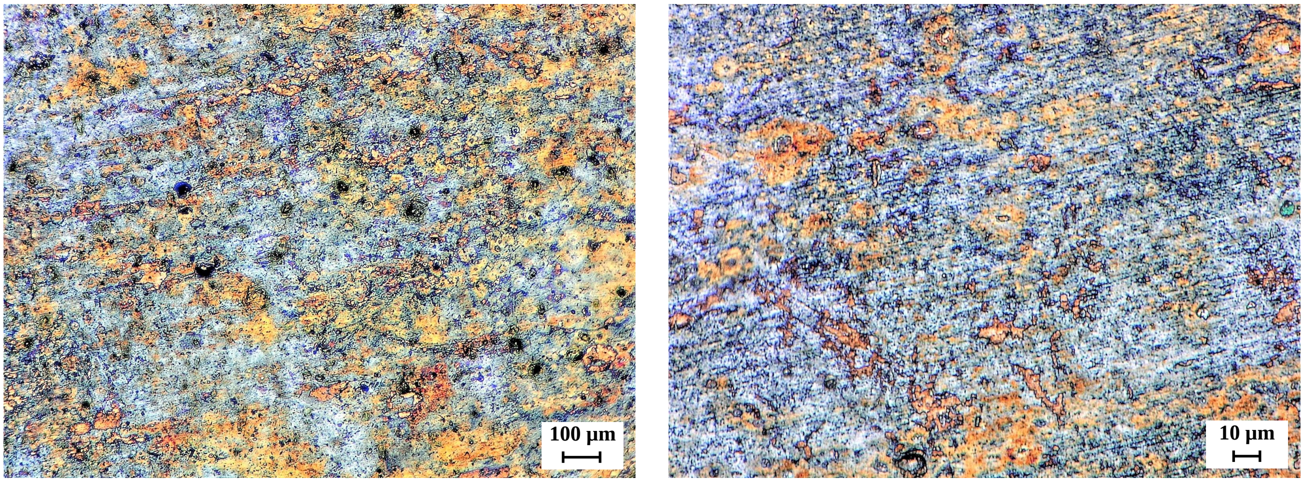

(a) (b)

Figure 71: Digital microscopy images at (a) low and (b) high magnification of the Al7075 T6 sample eroded with the WARER technique.

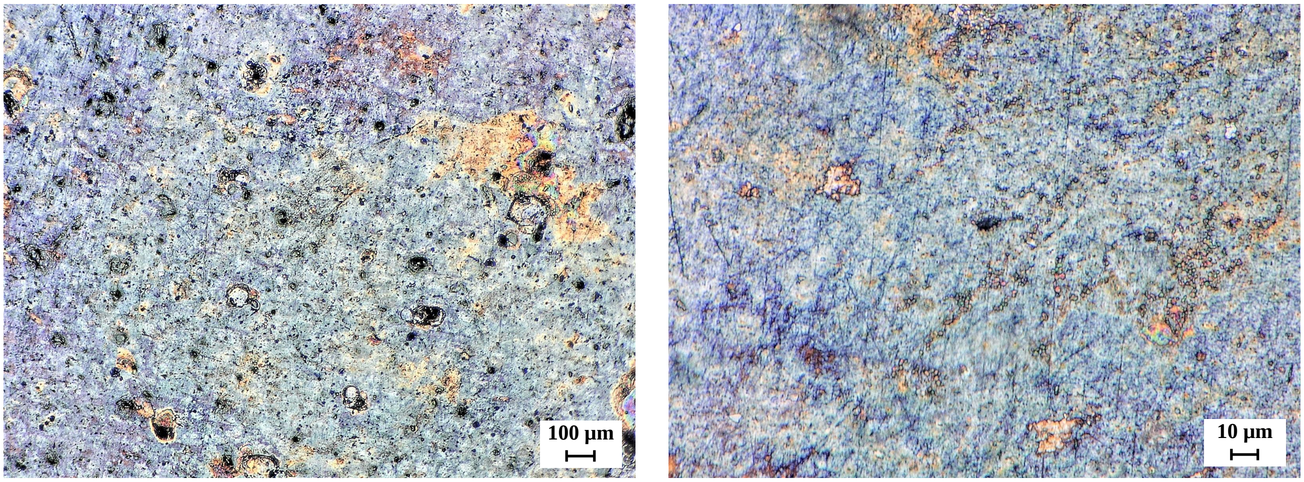

(a) (b)

Figure 72: Digital microscopy images at (a) low and (b) high magnification of the Al7075 FSP T6 sample eroded with the WARER technique.

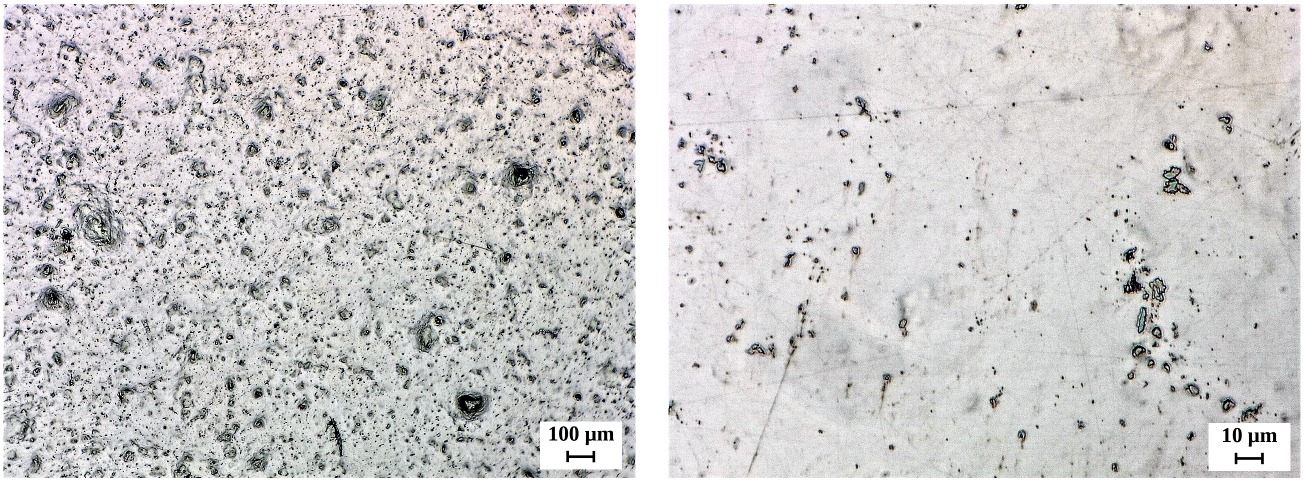

(a) (b)

Figure 73: Digital microscopy images at (a) low and (b) high magnification of the Ni bulk sample eroded with the WARER technique.

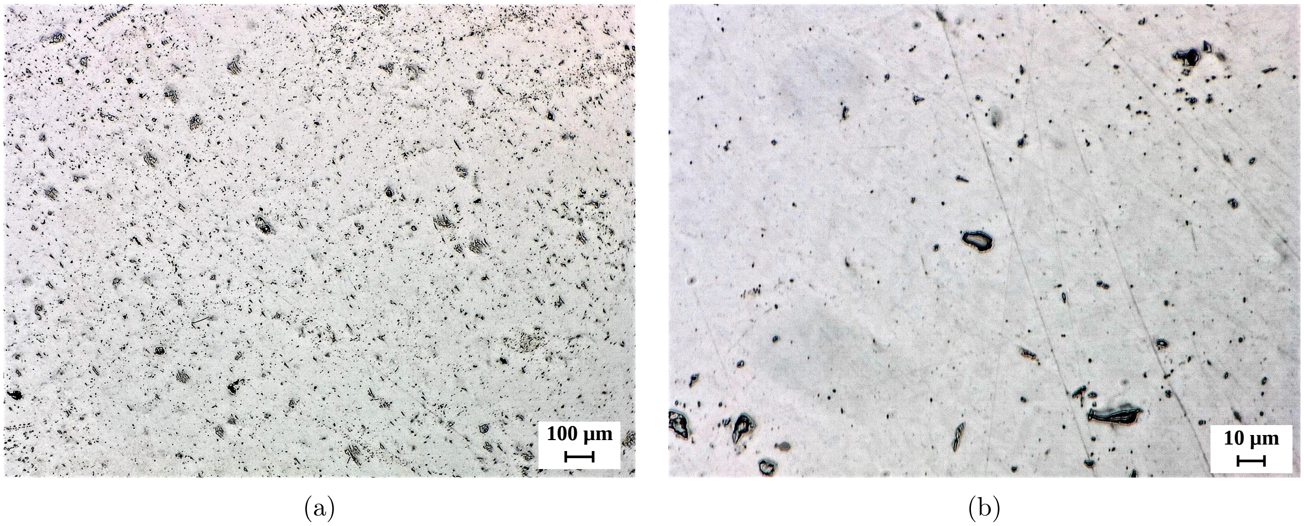

(a)

(b)

Figure 74: Digital microscopy images at (a) low and (b) high magnification of the Ti6Al4V sample eroded with the WARER technique.

## 6.5 Values of the roughness measurements

| $R_a$ in [nm] | Al7075 T4 | Al7075 T6 | Al7075 FSP T6 | Ti6Al4V | Ni bulk |
|---|---|---|---|---|---|
| Zone A | 216.4 | 168.9 | 132.1 | - | 201.8 |
| Zone B | 210.4 | 181.7 | 197.7 | - | 182.6 |
| Zone C | 297.7 | 192.7 | 209.2 | 164.7 | 201.1 |
| Zone D | 377.9 | 297.3 | 270.3 | 184.4 | 277.15 |
| Zone E | 149.6 | 188.9 | 165.6 | 162.3 | 270.6 |
| Zone F | 241.6 | 187.7 | 171.5 | 102.9 | 220.9 |
| Zone G | 256.7 | 232.3 | 195.8 | - | 144.5 |
| Zone H | 331.3 | 284.9 | 255.8 | - | 235.1 |

Table 15: Arithmetic mean roughness parameter $R_a$ expressed in nm, measured for each of the erosion zones on the PJET samples.

| $R_{ku}$ | Al7075 T4 | Al7075 T6 | Al7075 FSP T6 | Ti6Al4V | Ni bulk |
|---|---|---|---|---|---|
| Zone A | 7.62 | 21.10 | 7.34 | - | 9.20 |
| Zone B | 6.09 | 7.28 | 16.45 | - | 5.03 |
| Zone C | 5.84 | 7.49 | 9.52 | 6.52 | 5.29 |
| Zone D | 6.03 | 8.40 | 7.80 | 6.96 | 3.81 |
| Zone E | 5.20 | 4.70 | 5.31 | 5.55 | 3.08 |
| Zone F | 4.90 | 5.41 | 7.35 | 8.48 | 4.07 |
| Zone G | 9.61 | 5.54 | 12.10 | - | 5.14 |
| Zone H | 6.94 | 6.99 | 12.92 | - | 4.78 |

Table 16: Kurtosis roughness parameter, $R_{ku}$, measured for each of the erosion zones on the PJET samples.

| $R_{sk}$ | Al7075 T4 | Al7075 T6 | Al7075 FSP T6 | Ti6Al4V | Ni bulk |
|---|---|---|---|---|---|
| Zone A | -0.56 | 0.65 | -1.32 | - | 0.31 |
| Zone B | -1.15 | -1.75 | -1.84 | - | -0.38 |
| Zone C | -0.89 | -1.84 | -1.52 | 0.10 | -0.97 |
| Zone D | -1.26 | -1.29 | -1.34 | 0.06 | -0.49 |
| Zone E | -0.37 | -0.17 | -0.51 | -0.55 | -0.15 |
| Zone F | -0.63 | -1.04 | -1.15 | -1.01 | 0.18 |
| Zone G | -1.14 | -0.77 | -1.58 | - | -0.64 |
| Zone H | -1.08 | -0.33 | -1.36 | - | -0.84 |

Table 17: Skewness roughness parameter, $R_{sk}$, measured for each of the erosion zones on the PJET samples.

| | Al7075 T4 | Al7075 T6 | Al7075 FSP T6 | Ti6Al4V | Ni bulk |
|---|---|---|---|---|---|
| $R_a$ | 371.8 | 205.5 | 208.5 | 136.1 | 291.7 |
| $R_{ku}$ | 7.32 | 7.70 | 11.89 | 5.73 | 6.59 |
| $R_{sk}$ | -1.42 | -1.21 | -2.10 | -0.24 | -0.48 |

Table 18: Roughness parameters, $R_a$, $R_{ku}$ and $R_{sk}$ measured on the center zone of the WARER samples.

# References

[1] M. F. Ashby, *Materials selection in mechanical design*, 4th ed. Burlington, MA: Butterworth-Heinemann, 2011, 646 pp., OCLC: ocn639573741, ISBN: 978-1-85617-663-7.

[2] *Scholarly community encyclopedia - water droplet erosion*, 2020. [Online]. Available: `https://encyclopedia.pub/503` (visited on 11/11/2020).

[3] A. Castorrini, A. Corsini, F. Rispoli, P. Venturini, K. Takizawa, and T. E. Tezduyar, "Computational analysis of wind-turbine blade rain erosion," *Computers & Fluids*, vol. 141, pp. 175–183, 2016, Advances in Fluid-Structure Interaction, ISSN: 0045-7930. DOI: `https://doi.org/10.1016/j.compfluid.2016.08.013`. [Online]. Available: `https://www.sciencedirect.com/science/article/pii/S0045793016302596`.

[4] M. Ibrahim and M. Medraj, "Water droplet erosion of wind turbine blades: Mechanics, testing, modeling and future perspectives," *Materials*, vol. 13, p. 157, Dec. 2019. DOI: `10.3390/ma13010157`.

[5] B. CASTANIE, C. BOUVET, and M. Ginot, "Review of composite sandwich structure in aeronautic applications," *Composites Part C: Open Access*, vol. 1, p. 100 004, 2020, ISSN: 2666-6820. DOI: `https://doi.org/10.1016/j.jcomc.2020.100004`. [Online]. Available: `https://www.sciencedirect.com/science/article/pii/S2666682020300049`.

[6] L. Bartolomé and J. Teuwen, "Prospective challenges in the experimentation of the rain erosion on the leading edge of wind turbine blades," *Wind Energy*, vol. 22, no. 1, pp. 140–151, 2019. DOI: `10.1002/we.2272`. [Online]. Available: `https://onlinelibrary.wiley.com/doi/abs/10.1002/we.2272`.

[7] R. Li, H. Ninokata, and M. Mori, "A numerical study of impact force caused by liquid droplet impingement onto a rigid wall," *Progress in Nuclear Energy*, vol. 53, no. 7, pp. 881–885, 2011, The Third International Symposium on Innovative Nuclear Energy Systems, INES-3- Innovative Nuclear Technologies for Low-Carbon Society, ISSN: 0149-1970. DOI: `https://doi.org/10.1016/j.pnucene.2011.03.002`. [Online]. Available: `http://www.sciencedirect.com/science/article/pii/S0149197011000369`.

[8] Y. Tatekura, M. Watanabe, K. Kobayashi, and T. Sanada, "Pressure generated at the instant of impact between a liquid droplet and solid surface," *Royal Society Open Science*, vol. 5, p. 181 101, Dec. 2018. DOI: `10.1098/rsos.181101`.

[9] M. Keegan, D. Nash, and M. Stack, "Modelling rain drop impact of offshore wind turbine blades," *Proceedings of the ASME Turbo Expo*, vol. 6, Jun. 2012. DOI: `10.1115/GT2012-69175`.

[10] H. Slot, E. Gelinck, C. Rentrop, and E. van der Heide, "Leading edge erosion of coated wind turbine blades: Review of coating life models," *Renewable Energy*, vol. 80, pp. 837–848, 2015, ISSN: 0960-1481. DOI: `https://doi.org/10.1016/j.renene.2015.02.036`. [Online]. Available: `http://www.sciencedirect.com/science/article/pii/S0960148115001366`.

[11] N. Li, Q. Zhou, X. Chen, T. Xu, S. Hui, and D. Zhang, "Liquid drop impact on solid surface with application to water drop erosion on turbine blades, part i: Nonlinear wave model and solution of one-dimensional impact," *International Journal of Mechanical Sciences*, vol. 50, no. 10, pp. 1526–1542, 2008, ISSN: 0020-7403. DOI: `https://doi.org/10.1016/j.ijmecsci.2008.08.001`. [Online]. Available: `http://www.sciencedirect.com/science/article/pii/S0020740308001185`.

[12] W. F. Adler, "Liquid drop collisions on deformable media," *Journal of Materials Science*, vol. 12, no. 6, pp. 1253–1271, Jun. 1977, ISSN: 1573-4803. DOI: `10.1007/BF02426864`. [Online]. Available: `https://doi.org/10.1007/BF02426864`.

[13] H. Slot, D. Matthews, D. Schipper, and E. Van Der Heide, "Fatigue-based model for the droplet impingement erosion incubation period of metallic surfaces," *Fatigue & Fracture of Engineering Materials & Structures*, vol. 44, Oct. 2020. DOI: `10.1111/ffe.13352`.

[14] H. Kirols, "Water droplet erosion: Influencing parameters, representation and comparisons," Master's thesis, Concordia University, Jul. 2015. [Online]. Available: `https://spectrum.library.concordia.ca/980617/`.

[15] O. Gohardani, "Impact of erosion testing aspects on current and future flight conditions," *Progress in Aerospace Sciences*, vol. 47, no. 4, pp. 280–303, May 1, 2011, ISSN: 0376-0421. DOI: `10.1016/j.paerosci.2011.04.001`. [Online]. Available: `https://www.sciencedirect.com/science/article/pii/S0376042111000315` (visited on 02/21/2021).

[16] M. S. Mahdipoor, "Water droplet erosion resistant materials and surface treatments," Feb. 2016, [Online]. Available: `https://spectrum.library.concordia.ca/980886/`.

[17] F. Heymann, "Erosion by liquids ... the mysterious murderer of metals," *Machine Design*, vol. December 10, pp. 118–124, 1970. [Online]. Available: `http://users.encs.concordia.ca/~tmg/images/8/8b/Erosion_by_liquids.pdf`.

[18] H. Kirols, D. Kevorkov, A. Uihlein, and M. Medraj, "The effect of initial surface roughness on water droplet erosion behaviour," *Wear*, vol. 342-343, pp. 198–209, 2015, ISSN: 0043-1648. DOI: `https://doi.org/10.1016/j.wear.2015.08.019`. [Online]. Available: `http://www.sciencedirect.com/science/article/pii/S0043164815004032`.

[19] A. Mednikov, A. Tkhabisimov, M. Dasaev, A. Burmistrov, and O. Zilova, "Metallographic studies results of 20kh13 steel samples with textured relief, modified surface and protective coating," *E3S Web of Conferences*, vol. 140, p. 02 009, Jan. 2019. DOI: `10.1051/e3sconf/201914002009`.

[20] Q. Zhou, N. Li, X. Chen, T. Xu, S. Hui, and D. Zhang, "Liquid drop impact on solid surface with application to water drop erosion on turbine blades, part ii: Axisymmetric solution and erosion analysis," *International Journal of Mechanical Sciences*, vol. 50, no. 10, pp. 1543–1558, 2008, ISSN: 0020-7403. DOI: `https://doi.org/10.1016/j.ijmecsci.2008.08.002`. [Online]. Available: `http://www.sciencedirect.com/science/article/pii/S0020740308001197`.

[21] M. Ahmad, M. Casey, and N. Sürken, "Experimental assessment of droplet impact erosion resistance of steam turbine blade materials," *Wear*, vol. 267, no. 9, pp. 1605–1618, 2009, ISSN: 0043-1648. DOI: `https://doi.org/10.1016/j.wear.2009.06.012`. [Online]. Available: `https://www.sciencedirect.com/science/article/pii/S0043164809004219`.

[22] S. Zhang, *Accelerated rain erosion of wind turbine blade coatings*. Danmarks Tekniske Universitet (DTU), 2014, ISBN: 978-87-93054-49-3. [Online]. Available: `https://orbit.dtu.dk/en/publications/accelerated-rain-erosion-of-wind-turbineblade-coatings` (visited on 02/21/2021).

[23] D. Ma, "Liquid impingement erosion performance of low plasticity burnished Ti6Al4V," Jun. 2014. [Online]. Available: `https://spectrum.library.concordia.ca/978755/`.

[24] Wikipedia, *Drop (liquid) — Wikipedia, the free encyclopedia*, 2021. [Online]. Available: `http://en.wikipedia.org/w/index.php?title=Drop%5C%20(liquid)&oldid=1006388070` (visited on 03/02/2021).

[25] M. S. Mahdipoor, H. S. Kirols, D. Kevorkov, P. Jedrzejowski, and M. Medraj, "Influence of impact speed on water droplet erosion of TiAl compared with Ti6Al4V," *Scientific Reports*, vol. 5, no. 1, p. 14 182, Sep. 22, 2015, ISSN: 2045-2322. DOI: `10.1038/srep14182`. [Online]. Available: `https://www.nature.com/articles/srep14182` (visited on 02/02/2021).

[26] J. Bech, C. Hasager, and C. Bak, “Extending the life of wind turbine blade leading edges by reducing the tip speed during extreme precipitation events,” *Wind Energy Science*, vol. 3, pp. 729–748, Oct. 2018. DOI: `10.5194/wes-3-729-2018`.

[27] M. Ahmad, M. Schatz, and M. Casey, “An empirical approach to predict droplet impact erosion in low-pressure stages of steam turbines,” *Wear*, vol. 402-403, pp. 57–63, 2018, ISSN: 0043-1648. DOI: `https://doi.org/10.1016/j.wear.2018.02.004`. [Online]. Available: `http://www.sciencedirect.com/science/article/pii/S0043164817314084`.

[28] E. Tobin, T. Young, D. Raps, and O. Rohr, “Comparison of liquid impingement results from whirling arm and water-jet rain erosion test facilities,” *Wear*, vol. 271, no. 9, pp. 2625–2631, 2011, 18th International Conference on Wear of Materials, ISSN: 0043-1648. DOI: `https://doi.org/10.1016/j.wear.2011.02.023`. [Online]. Available: `http://www.sciencedirect.com/science/article/pii/S0043164811002699`.

[29] R. Herring, K. Dyer, F. Martin, and C. Ward, “The increasing importance of leading edge erosion and a review of existing protection solutions,” *Renewable and Sustainable Energy Reviews*, vol. 115, p. 109 382, 2019, ISSN: 1364-0321. DOI: `https://doi.org/10.1016/j.rser.2019.109382`. [Online]. Available: `http://www.sciencedirect.com/science/article/pii/S1364032119305908`.

[30] E. Tobin, O. Rohr, D. Raps, W. Willemse, P. Norman, and T. Young, “Surface topography parameters as a correlation factor for liquid droplet erosion test facilities,” *Wear*, vol. 328-329, pp. 318–328, 2015, ISSN: 0043-1648. DOI: `https://doi.org/10.1016/j.wear.2015.02.054`. [Online]. Available: `http://www.sciencedirect.com/science/article/pii/S0043164815001635`.

[31] P. Lammel, A. Whitehead, H. Simunkova, O. Rohr, and B. Gollas, “Droplet erosion performance of composite materials electroplated with a hard metal layer,” *Wear*, vol. 271, no. 9, pp. 1341–1348, 2011, 18th International Conference on Wear of Materials, ISSN: 0043-1648. DOI: `https://doi.org/10.1016/j.wear.2010.12.034`. [Online]. Available: `http://www.sciencedirect.com/science/article/pii/S0043164811001542`.

[32] A. S. Verma, S. G. Castro, Z. Jiang, and J. J. Teuwen, “Numerical investigation of rain droplet impact on offshore wind turbine blades under different rainfall conditions: A parametric study,” *Composite Structures*, vol. 241, p. 112 096, 2020, ISSN: 0263-8223. DOI: `https://doi.org/10.1016/j.compstruct.2020.112096`. [Online]. Available: `http://www.sciencedirect.com/science/article/pii/S0263822319329794`.

[33] E. Cortés, F. Sánchez, A. O’Carroll, B. Madramany, M. Hardiman, and T. M. Young, “On the material characterisation of wind turbine blade coatings: The effect of interphase coating-laminate adhesion on rain erosion performance,” *Materials (Basel, Switzerland)*, vol. 10, no. 10, Sep. 28, 2017, ISSN: 1996-1944. DOI: `10.3390/ma10101146`.

[34] A. H. Whitehead, H. Simunkova, P. Lammel, J. Wosik, N. Zhang, and B. Gollas, “Rain erosion characteristics of electrodeposited ni–sic metal-matrix composite layers,” *Wear*, vol. 270, no. 9, pp. 695–702, 2011, ISSN: 0043-1648. DOI: `https://doi.org/10.1016/j.wear.2011.02.001`. [Online]. Available: `http://www.sciencedirect.com/science/article/pii/S0043164811000536`.

[35] K. Tomantschger, N. Nagarajan, T. Kowpak, F. Gonzalez, M. Neacsu, I. Brooks, A. Wang, and T. Ronis, “Nanometal-polymer hybrids: Application of high strength nanocrystalline metallic structural layers on thermoplastic articles,” *Jahrbuch Oberflaechentechnik*, vol. 67, Jan. 2011.

[36] *ASTM international - ASTM G73-10(2017), standard test method for liquid impingement erosion using rotating apparatus*, West Conshohocken, PA, DOI 10.1520/G0073-10R17, 2017. [Online]. Available: `http://www.astm.org/cgi-bin/resolver.cgi?G73-10(2017)` (visited on 11/02/2020).

[37] S. Zhang, K. Dam-Johansen, P. L. Bernad, and S. Kiil, "Rain erosion of wind turbine blade coatings using discrete water jets: Effects of water cushioning, substrate geometry, impact distance, and coating properties," *Wear*, vol. 328-329, pp. 140–148, 2015, ISSN: 0043-1648. DOI: `https://doi.org/10.1016/j.wear.2015.01.079`. [Online]. Available: `http://www.sciencedirect.com/science/article/pii/S0043164815001040`.

[38] J. H. Brunton and M. C. Rochester, "Erosion of solid surfaces by the impact of liquid drops," *C.M. Preece (Ed.), Treatise on Materials Science and Technology, Academic press, New York*, pp. 186–248, 1979.

[39] M. C. Rochester, "The impact of a liquid drop with a solid surface and the effects of the properties of the liquid on the erosion of solids," Doctoral Thesis, PhD thesis, University of Cambridge, Sep. 1977.

[40] E. Tobin, T. Young, and D. Raps, "Evaluation and correlation of inter-laboratory results from a rain erosion test campaign," vol. 6, Sep. 2012.

[41] *HexFlow infusion resins | hexcel*. [Online]. Available: `https://www.hexcel.com/Products/Prepregs-and-Resins/HexFlow-Infusion-Resins-for-Aerospace` (visited on 05/17/2021).

[42] *CYCOM 977-2*, Solvay. [Online]. Available: `https://www.solvay.com/en/product/cycom-977-2` (visited on 05/17/2021).

[43] A. Jumahat, C. Soutis, F. Jones, and A. Hodzic, "Fracture mechanisms and failure analysis of carbon fibre/toughened epoxy composites subjected to compressive loading," *Composite Structures*, vol. 92, no. 2, pp. 295–305, 2010, ISSN: 0263-8223. DOI: `https://doi.org/10.1016/j.compstruct.2009.08.010`. [Online]. Available: `https://www.sciencedirect.com/science/article/pii/S0263822309002839`.

[44] V. Rao and D. Buckley, "Solid impingement erosion mechanisms and characterization of erosion resistance of ductile metals," *NASA Technical Reports Server (NTRS)*, Jan. 1982. [Online]. Available: `https://ntrs.nasa.gov/citations/19840004219` (visited on 05/30/2021).

[45] K. Karuppusamy, R. Anantharam, C. J. Kennady, R. M. Krishnan, and S. R. Natarajan, "Pit-free nickel electroplating," *Metal Finishing*, vol. 90, pp. 15–19, 1992.

[46] N. P. Wasekar, P. Haridoss, and G. Sundararajan, "Solid particle erosion of nanocrystalline nickel coatings: Influence of grain size and adiabatic shear bands," *Metallurgical and Materials Transactions A*, vol. 49, no. 2, pp. 476–489, Feb. 2018, ISSN: 1073-5623, 1543-1940. DOI: `10.1007/s11661-017-4434-x`. [Online]. Available: `http://link.springer.com/10.1007/s11661-017-4434-x` (visited on 05/18/2021).

[47] M. B. Lezaack and A. Simar, "Avoiding abnormal grain growth in thick 7xxx aluminium alloy friction stir welds during t6 post heat treatments," *Materials Science and Engineering: A*, vol. 807, p. 140 901, 2021, ISSN: 0921-5093. DOI: `https://doi.org/10.1016/j.msea.2021.140901`. [Online]. Available: `https://www.sciencedirect.com/science/article/pii/S0921509321001702`.

[48] J.-F. Li, Z.-W. Peng, C.-X. Li, Z.-Q. Jia, W.-J. Chen, and Z.-Q. Zheng, "Mechanical properties, corrosion behaviors and microstructures of 7075 aluminium alloy with various aging treatments," *Transactions of Nonferrous Metals Society of China*, vol. 18, no. 4, pp. 755–762, 2008, ISSN: 1003-6326. DOI: `https://doi.org/10.1016/S1003-6326(08)60130-2`. [Online]. Available: `https://www.sciencedirect.com/science/article/pii/S1003632608601302`.

[49] X. Yang, Y.-d. Li, X.-m. Luo, H.-w. Zhou, Q.-y. Cai, M. Li, and Y. Ma, "Microstructural evaluation and mechanical properties of 7075 aluminum alloy prepared by controlled diffusion solidification," *China Foundry*, vol. 16, no. 4, pp. 238–247, Jul. 2019, ISSN: 1672-6421, 2365-9459. DOI: `10.1007/s41230-019-9059-9`. [Online]. Available: `http://link.springer.com/10.1007/s41230-019-9059-9` (visited on 03/30/2021).

[50] F. Hannard, “3D characterization, modelling and tailoring of microstructure heterogeneity effects on damage and fracture of 6xxx aluminium alloys,” PhD thesis, Jan. 2018.

[51] J.-Q. Su, T. Nelson, R. Mishra, and M. Mahoney, “Microstructural investigation of friction stir welded 7050-t651 aluminium,” *Acta Materialia*, vol. 51, no. 3, pp. 713–729, 2003, ISSN: 1359-6454. DOI: `https://doi.org/10.1016/S1359-6454(02)00449-4`. [Online]. Available: `https://www.sciencedirect.com/science/article/pii/S1359645402004494`.

[52] T. Aoba, M. Kobayashi, and H. Miura, “Effects of aging on mechanical properties and microstructure of multi-directionally forged 7075 aluminum alloy,” *Materials Science and Engineering: A*, vol. 700, pp. 220–225, 2017, ISSN: 0921-5093. DOI: `https://doi.org/10.1016/j.msea.2017.06.017`. [Online]. Available: `https://www.sciencedirect.com/science/article/pii/S0921509317307827`.

[53] M. Do Vale, N. De Medeiros, G. Fonseca, S. Diniz, A. Paula, and L. P. Brandao, “On the mechanical behavior of an al 7075 alloy deformed by asymmetrical and conventional rolling,” *Matéria (Rio de Janeiro)*, vol. 24, May 2019. DOI: `10.1590/s1517-707620190001.0625`.

[54] A. Joshi, C. R. Shastry, and M. Levy, “Effect of heat treatment on solute concentration at grain boundaries in 7075 aluminum alloy,” *Metallurgical Transactions A*, vol. 12, no. 6, pp. 1081–1088, Jun. 1, 1981, ISSN: 1543-1940. DOI: `10.1007/BF02643489`. [Online]. Available: `https://doi.org/10.1007/BF02643489`.

[55] Z. He, H. He, J. Lou, Y. Li, D. Li, Y. Chen, and S. Liu, “Fabrication, structure and mechanical and ultrasonic properties of medical ti6al4v alloys part i: Microstructure and mechanical properties of ti6al4v alloys suitable for ultrasonic scalpel,” *Materials*, vol. 13, p. 478, Jan. 2020. DOI: `10.3390/ma13020478`.

[56] S. Bec, A. Tonck, J.-M. Georges, E. Georges, and J.-L. Loubet, “Improvements in the indentation method with a surface force apparatus,” *Philosophical Magazine, Part A*, vol. 74, no. 5, pp. 1061–1072, Nov. 1996. DOI: `10.1080/01418619608239707`.

[57] M. Dao, N. Chollacoop, K. Van Vliet, T. Venkatesh, and S. Suresh, “Computational modeling of the forward and reverse problems in instrumented sharp indentation,” *Acta Materialia*, vol. 49, no. 19, pp. 3899–3918, 2001, ISSN: 1359-6454. DOI: `https://doi.org/10.1016/S1359-6454(01)00295-6`. [Online]. Available: `https://www.sciencedirect.com/science/article/pii/S1359645401002956`.

[58] S. Masson, “Numerical investigation of droplet trajectories in a raindrop erosion test bench,” PhD thesis, UCL - Ecole polytechnique de Louvain, 2019. [Online]. Available: `http://hdl.handle.net/2078.1/thesis:19588`.

[59] U. Ghantasala, *Rain erosion performance of the material to be used as the leading edge protection of the wind turbine blades*, Mar. 2021. [Online]. Available: `http://essay.utwente.nl/85944/`.

[60] M. Matuszewski, M. Słomion, A. Mazurkiewicz, and D. Pimenov, “Assessment of friction pair elements condition based on changes in the geometric surface structure isotropicity degree,” *MATEC Web of Conferences*, vol. 302, p. 01 015, Jan. 2019. DOI: `10.1051/matecconf/201930201015`.

[61] E. Gadelmawla, M. Koura, T. Maksoud, I. Elewa, and H. Soliman, “Roughness parameters,” *Journal of Materials Processing Technology*, vol. 123, no. 1, pp. 133–145, 2002, ISSN: 0924-0136. DOI: `https://doi.org/10.1016/S0924-0136(02)00060-2`. [Online]. Available: `https://www.sciencedirect.com/science/article/pii/S0924013602000602`.

[62] M. Taro, T. Chaise, and D. Nélias, “A methodology to predict the roughness of shot peened surfaces,” *Journal of Materials Processing Technology*, vol. 217, pp. 65–76, 2015, ISSN: 0924-0136. DOI: `https://doi.org/10.1016/j.jmatprotec.2014.10.016`. [Online]. Available: `https://www.sciencedirect.com/science/article/pii/S0924013614003835`.

[63] S. M. Kumar, R. Pramod, M. S. Kumar, and H. Govindaraju, "Evaluation of fracture toughness and mechanical properties of aluminum alloy 7075, t6 with nickel coating," *Procedia Engineering*, vol. 97, pp. 178–185, 2014, "12th Global Congress on Manufacturing and Management" GCMM - 2014, ISSN: 1877-7058. DOI: `https://doi.org/10.1016/j.proeng.2014.12.240`. [Online]. Available: `https://www.sciencedirect.com/science/article/pii/S1877705814032998`.

[64] F. Hannard, S. Castin, E. Maire, R. Mokso, T. Pardoen, and A. Simar, "Ductilization of aluminium alloy 6056 by friction stir processing," *Acta Materialia*, vol. 130, Jan. 2017. DOI: `10.1016/j.actamat.2017.01.047`.

[65] H. Kirols, M. S. Mahdipoor, D. Kevorkov, and M. Medraj, "Water droplet impingement erosion: Testing, mechanisms and improved representation," Aug. 2016.

[66] A. Phelps, "Materials selection for wear resistance," in. Nov. 2007, vol. 56, pp. 1275–1286, ISBN: 9780470172551. DOI: `10.1002/9780470172551.ch41`.

[67] F. Heymann, "Toward quantitative prediction of liquid impact erosion," in *Characterization and Determination of Erosion Resistance*, West Conshohocken, PA: ASTM International, Jan. 1, 1970, pp. 212–243, ISBN: 978-0-8031-4589-4. DOI: `10.1520/STP26871S`. [Online]. Available: `https://www.astm.org/DIGITAL_LIBRARY/STP/PAGES/STP26871S.htm`.

[68] F. Zok and A. Miserez, "Property maps for abrasion resistance of materials.," *Acta materialia*, vol. 55 18, pp. 6365–6371, 2007.

[69] C. Houqun, W. Shengxin, and D. Faning, "Chapter 10 - research progress on dynamic mechanical behavior of high arch dam concrete," in *Seismic Safety of High Arch Dams*, C. Houqun, W. Shengxin, and D. Faning, Eds., Oxford: Academic Press, 2016, pp. 239–256, ISBN: 978-0-12-803628-0. DOI: `https://doi.org/10.1016/B978-0-12-803628-0.00010-0`. [Online]. Available: `https://www.sciencedirect.com/science/article/pii/B9780128036280000100`.

[70] S. Zhang, P. T. Pedersen, and R. Villavicencio, "5 - collision damage assessment by nonlinear finite element simulations," in *Probability and Mechanics of Ship Collision and Grounding*, S. Zhang, P. T. Pedersen, and R. Villavicencio, Eds., Butterworth-Heinemann, 2019, pp. 324–368, ISBN: 978-0-12-815022-1. DOI: `https://doi.org/10.1016/B978-0-12-815022-1.00005-0`. [Online]. Available: `https://www.sciencedirect.com/science/article/pii/B9780128150221000050`.

[71] *Mapcoat - AkzoNobel Aerospace Coatings - AkzoNobel*. [Online]. Available: `https://aerospace.akzonobel.com/product/mapcoat` (visited on 06/04/2021).

[72] X. Wu, J. Sun, J. Wang, Y. Jiang, and J. Li, "Investigation on galvanic corrosion behaviors of cfrps and aluminum alloys systems for automotive applications," *Materials and Corrosion*, Dec. 2018. DOI: `10.1002/maco.201810635`.

[73] C. R. Siviour and J. L. Jordan, "High Strain Rate Mechanics of Polymers: A Review," *Journal of Dynamic Behavior of Materials*, vol. 2, no. 1, pp. 15–32, Mar. 2016, ISSN: 2199-7454. DOI: `10.1007/s40870-016-0052-8`. [Online]. Available: `https://doi.org/10.1007/s40870-016-0052-8` (visited on 06/05/2021).

[74] A. Mukherjee, M. Ghosh, K. Mondal, V. Parameswaran, A. Moon, and A. Varshney, "Study of mechanical properties, microstructures and corrosion behavior of al 7075 t651 alloy with varying strain rate," *IOP Conference Series: Materials Science and Engineering*, vol. 75, Feb. 2015. DOI: `10.1088/1757-899X/75/1/012031`.

[75] J. Pothnis, Y. Perla, H. Arya, and N. Naik, "High strain rate tensile behavior of aluminum alloy 7075 t651 and is 2062 mild steel," *Journal of Engineering Materials and Technology*, vol. 133, p. 021 026, Apr. 2011. DOI: `10.1115/1.4003113`.

[76] J. Bergström, "7 - plasticity models," in *Mechanics of Solid Polymers*, J. Bergström, Ed., William Andrew Publishing, 2015, pp. 353–369, ISBN: 978-0-323-31150-2. DOI: `https://doi.org/10.1016/B978-0-323-31150-2.00007-8`. [Online]. Available: `https://www.sciencedirect.com/science/article/pii/B9780323311502000078`.

[77] M. Sasso, G. Newaz, and D. Amodio, "Material characterization at high strain rate by hopkinson bar tests and finite element optimization," *Materials Science and Engineering: A*, vol. 487, no. 1, pp. 289–300, 2008, ISSN: 0921-5093. DOI: `https://doi.org/10.1016/j.msea.2007.10.042`. [Online]. Available: `https://www.sciencedirect.com/science/article/pii/S0921509307017431`.

**UNIVERSITÉ CATHOLIQUE DE LOUVAIN**
**École polytechnique de Louvain**
Rue Archimède, 1 bte L6.11.01, 1348 Louvain-la-Neuve, Belgique | **www.uclouvain.be/epl**